ESTIMATION OF THE HIGH FREQUENCY DECAY PARAMETER (κ) AND ANELASTIC ATTENUATION FACTOR (Q) FOR ISTANBUL

by

Hakan Süleyman

B.S., Civil Engineering, Yıldız Technical University, 2014

Submitted to the Kandilli Observatory and Earthquake Research Institute
in partial fulfillment of the requirements for the degree of
Master of Science

Graduate Program in Earthquake Engineering

Boğaziçi University

2018

ESTIMATION OF THE HIGH FREQUENCY DECAY PARAMETER (κ) AND ANELASTIC ATTENUATION FACTOR (Q) FOR ISTANBUL

APPROVED BY:

Prof. Eser Çaktı Boğaziçi University (Thesis Supervisor)	…….
Prof. Ali Pınar Boğaziçi University	…….
Dr. Olga-Joan Ktenidou National Observatory of Athens	…….

DATE OF APPROVAL: …./…./……

ACKNOWLEDGEMENTS

First, I want to express my thankfulness to my supervisor Eser Çaktı. It has been an honor to be her M.Sc. student. She showed me the way for constructing myself as a researcher, shared her experience during the preparation of this thesis and motivated me in my time of need. I am also glad that I prepared this study with an excellent example of successful woman engineer and professor.

Olga-Joan Ktenidou, who refined my work and made it scientifically much more meaningful is among the most successful people who could contribute to this work. Her effort to share her knowledge was admiring. I am so glad that I had the chance to be able to work with her. Another person who gave me useful feedback was Ali Pınar. I am grateful to him that he shared some useful tips that helped me construct my thesis better.

Without my parents, my mother Semra and my father Neim I wouldn't be able to reach the stage of gaining an M.Sc. degree. They gave me the freedom and opportunities that made me be successful enough to reach this level. More than anything, they dedicated part of their lives just to build my future in a healthy and safe way – which is one of the most supreme human behaviors that could ever realize.

I especially want to thank Monica Marks, for being beside me in every moment while I was preparing my thesis. Her existence in my life is so meaningful that she makes every part of my life more successful. Even without touching my thesis she could make it be much better. She is and will be one of the most precious people that have ever came into my life.

ABSTRACT

ESTIMATION OF THE HIGH FREQUENCY DECAY PARAMETER (κ) AND ANELASTIC ATTENUATION FACTOR (Q) FOR ISTANBUL

In this study we attempt to estimate parameters that are related to path and near-surface effects, due to earthquakes that occurred in northwestern Turkey, by drawing on data from the Istanbul Earthquake Rapid Response System (IERRS) that is operated by the Department of Earthquake Engineering at Boğaziçi University's Kandilli Observatory and Earthquake Research Institute. Our data set includes over 4677 strong motion recordings from 115 stations of the IERRS. The records are associated with events having local magnitudes ranging within $4.0<M_L<6.5$ and epicentral distances between 6-444 km. Only records, that have a signal-to-noise ratio larger than 3, are kept for a more accurate selection of κ and estimation of Q. Horizontal-to-vertical spectral ratio profiles are observed, and fundamental frequencies are checked in order to prevent possible biases in the attenuation models. κ is measured from the acceleration Fourier amplitude spectra of shear-waves, as originally proposed by Anderson and Hough (1984). Several regional models are prepared as a function of site (κ_0) and distance ($m \times R$) by linearly regressing over distance. Correlations of azimuths, SNR levels and V_{S30} values with these models are discussed. A regional model for frequency dependent anelastic attenuation Q(f) is proposed by a regression analysis of acceleration Fourier amplitudes of shear-waves following Castro and Ruiz-Cruz (2005) and Safarshahi et al. (2013).

ÖZET

İSTANBUL İÇİN YÜKSEK FREKANS AZALIM PARAMETRESİ (κ) VE ANELASTİK AZALIM FAKTÖRÜ'NÜN (Q) HESAPLANMASI

Bu çalışmada, kuzeybatı Türkiye'de meydana gelen depremlerle ilişkili yayılım ve yakın yüzey etki parametreleri, Boğaziçi Üniversitesi, Kandilli Rasathanesi ve Deprem Araştırma Enstitüsü, Deprem Mühendisliği Anabilim Dalı tarafından işletilen İstanbul Deprem Acil Müdahale ve Uyarı Sistemi verileri yardımıyla hesaplanmıştır. Veri setimiz, 115 istasyon tarafından kaydedilen 4677 kuvvetli yer hareketi kaydını içermektedir. Veri setine dahil depremlerin yerel büyüklüğü $4.0<M_L<6.5$ ve merkez üssü uzaklığı 6-444 km arasında değişmektedir. κ ölçümü ve Q hesaplamasının yüksek doğruluk payına sahip olması için, sinyal-gürültü oranı 3'ün üzerinde olan kayıtlar kullanılmıştır. Yatay/düşey spektral oranlarına ait profiller ile temel frekanslar, azalım modellerindeki olası yanıltmalardan kaçınmak için özel olarak incelenmiştir. κ, aslen Anderson ve Hough (1984) tarafından önerilen yöntem izlenerek, kesme dalgalarının Fourier ivme spektrumları üzerinden belirlenmiştir. İstanbul için genel ve istasyonlar için özel olmak üzere bir seri saha (κ_0) ve uzaklık ($m \times R$) fonksiyonu üretilmiştir. Azimut, sinyal-gürültü oranı ve V_{S30} değerlerinin bu modeller ile ilişkisi tartışılmıştır. Son olarak, kesme dalgalarının Fourier ivme spektrumları üzerinden yapılan regresyon analizi ile frekansa bağlı anelastik azalım faktörü Q(f) için bölgesel bir model önerilmiştir (Castro and Ruiz-Cruz, 2005; Safarshahi et al., 2013).

TABLE OF CONTENTS

LIST OF FIGURES

LIST OF TABLES

LIST OF SYMBOLS

a	Logarithm of S
A(f,R)	Attenuation function
b	Distance-dependent parameter
B	S-wave velocity
D(f,R)	Observed spectral amplitude
ΔE	Maximum strain energy
Δf	Frequency range
E_0	Energy dissipation in a cycle
f_c	Corner frequency
f_e	Beginning of κ_r measurement
f_{max}	Beginning of the amplitude decay in FAS
f_x	End of κ_r measurement
G(R)	Geometrical spreading model
i	Event number
κ	High-frequency decay parameter
κ_0	Site parameter of κ
κ_r	Distance parameter of κ
m	Slope of regression line
M(f)	Source term
M_L	Local magnitude
M_w	Moment magnitude
μ	Mean value
Q	Anelastic attenuation factor
Q_S	Constant attenuation parameter
R	Distance parameter
R^2	Coefficient of determination
S	Source-dependent scalar
S_v	Integral sum of velocity spectrum
S_d	Integral sum of displacement spectrum

σ	Standard deviation
u(R)	Distance-dependent function
U(f,R)	Observed spectral amplitude
V_{S30}	S-wave velocity over the top 30 m
VSP	Vertical Seismic Profile

LIST OF ACRONYMS/ABBREVIATIONS

Avg.	Average
Comp.	Component
Eq.	Earthquake
FAS	Fourier Amplitude Spectrum
H	Horizontal
Hor	Horizontal
H/V	Horizontal-to-vertical
Hz	Hertz
IERRS	Istanbul Earthquake Rapid Response System
KOERI	Kandilli Observatory and Earthquake Research Center
Num.	Number
RMS	Root-mean-square
RETMC	Regional Earthquake-Tsunami Monitoring Center
SNR	Signal-to-noise ratio
V	Vertical
Ver	Vertical

1. INTRODUCTION

Istanbul is closely located to an active tectonic plate boundary. Being just a few kilometers off the North Anatolian Fault (NAF), it has been always exposed to very significant levels of seismic activity. Two destructive earthquakes that occurred in the Marmara region in 1999, having moment magnitudes of 7.4 and 7.2, left thousands dead and led to a massive destruction in the region, including Istanbul. Therefore, for such regions, understanding the physics of earthquakes is crucial both for saving human lives and preserving engineering structures.

Despite the fact that this region has been studied for many years, uncertainties still lead us to address fundamental questions based related to earthquake hazard. Source processes, path and site effects are attracting a lot of research interest as they are important in estimating expected ground motions in Istanbul.

This study attempts to fill in some of the above described gaps. Specifically, we develop regional path and site parameters for Istanbul. The high frequency decay parameter κ and the anelastic attenuation factor Q are estimated regarding site amplification and noise effects, by using a dense network of strong motion recorders installed in the city. These parameters can be used to generate realistic synthetic ground motions reliably through stochastic ground motion simulations; as well as they can be used in various GMPEs, for estimating other seismological parameters.

1.1. Use and Current Practice of Estimating κ and Q

Studies on site parameter of kappa (κ_0) has increased recently because of its significance in controlling high frequencies. Therefore, it is used as an input parameter for constraining high frequencies, while Q factor controls the frequency dependent attenuation in synthetic ground motions developed by hybrid, physics-based or stochastic ground motion simulations (i.e. Boore, 2003; Akinci et al. 2017). κ_0 is also an important input parameter for adjusting GMPEs regionally (Hassani and Atkinson, 2018).

Numerous studies on developing source, site and path parameters, as well as ground motion simulations are prepared for the Marmara region or for regions in the northwestern Turkey (i.e., Gündüz et. al., 1998; Durukal, 2002; Durukal and Çatalyürekli, 2004; Akinci et al., 2006; Askan et al., 2014; Akinci et al., 2017; Tanırcan and Dikmen 2018), while none of them encompassed the whole city of Istanbul specifically. Several of them include estimations on κ, just a few of them include estimations on Q factor.

In these studies, these estimations are generalized over the whole study area, except for Tanırcan and Dikmen (2018). In which they estimate site parameter of κ in five stations on the European side of Istanbul. Durukal and Çatalyürekli (2004) used nine stations located in Istanbul, out of 58 stations located around the western segments of North Anatolian Fault. Besides these studies, Askan et al. (2014), prepared a kappa model for Istanbul, where only a single station was located in Istanbul.

Akinci et al. (2006), observed several stochastic ground motion parameters for the Marmara region, while Gündüz et al. (1998) focused on estimating attenuation parameters for the same region. Both of the studies propose attenuation models, which are compared with ours in this study.

1.2. Major Results and Scope of Our Research

Our study focuses on estimating κ and Q through a dense station network located in Istanbul. Variety of the recorder locations, earthquake sources and their azimuths not only allowed us to observe and discuss the results, but also enabled us to prepare unusual correlations and ask new questions on acceptability and use of these parameters reliably.

The dense network consisting 115 recorders are located on various geological settings, meaning different conditions for wave propagation. Initially, through a visual inspection, we selected records having the highest quality. Before using them for further purposes, we bandpass filtered the data, eliminated the records with low signal-to-noise ratio and tapered them for the most efficient results.

Horizontal-to-vertical spectral ratio profiles were prepared, and fundamental frequencies were checked, so that we could prevent our individual κ_r measurements from unwanted site amplification effects.

At the stage of measuring κ, we carefully applied the suggested measuring criteria in the past relevant studies. Once they were reliably measured, several correlations with κ were prepared. Despite that we are focusing on a more concentrated region than the previous studies, it was difficult to offer any generalized model for κ. We present the variations in site and path components of κ, depending on azimuth and noise levels. Our results show that when azimuthal differences are taken into account the difference in estimations may vary up to 25%, which is likely to result even higher in further analyses. Some basic correlation that were prepared between κ and SNR encouraged us to work in this section deeper. We consider these estimations significantly, that these they may be taken into account once they will be studied in depth in the near future.

Anelastic attenuation parameter Q was estimated at the end of this study and compared with previous studies. A geometrical spreading model is also proposed within the Q model.

2. DATA DESCRIPTION

For this study, strong ground motion stations of the Istanbul Earthquake Rapid Response System (IERRS), installed by Earthquake Engineering Department, Boğaziçi University were used. 100 strong ground motion stations of IERRS were installed in densely populated settlements of the city along shores of the Marmara Sea (Erdik et al., 2003). Today, the number of the strong ground motion stations operated by IERRS is increased at least to 115 (Figure 2.1). These stations have the capacity of recording ground motions with 100 Hz sampling rate.

In March 2012, the original trigger-based system was updated to incorporate continuous recording capability. For this reason, events that occurred from March 2012 to July 2016 were taken into consideration in this study. This dataset includes more than 13000 records with three components, with a various source, path and site characteristics of 187 earthquakes.

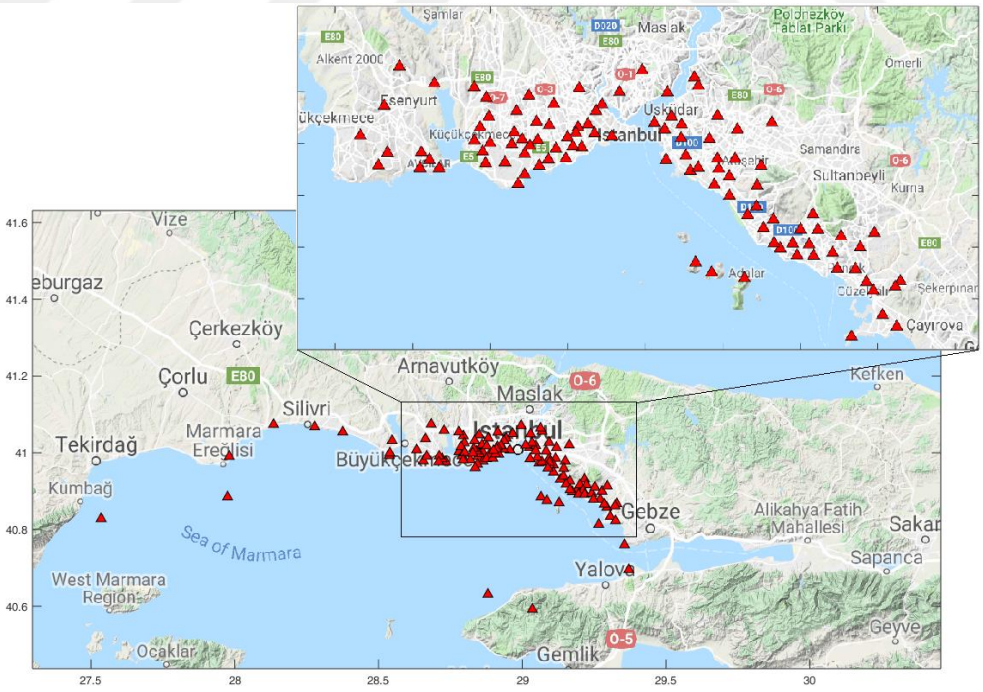

Figure 2.1. Distribution of the IERRS stations operated by Earthquake Engineering Department of Boğaziçi University.

2.1. Selection of the Data

Initially, earthquakes having local magnitudes below M_L = 4 were eliminated – because of the need for low corner frequency levels while measuring κ_r values on the Fourier amplitude spectra (FAS), which is discussed in the section 4.2 in detail. Then, the remaining records were visually checked. It was observed that some of the records were partially useful or fully useless; some strong motion amplitudes were contaminated by ambient noise (Figure 2.2), some were truncated (which usually resulted as partial loss of data; Figure 2.3), some of the records were excessively damaged because of the technical issues related with the instrumentation (Figure 2.4). An independent visual inspection for the same dataset had been previously performed (Malcioglu, personal communication, 2018). Similar amounts of data were eliminated in both visual inspections. Additionally, the data eliminated in both studies were mostly the same recordings.

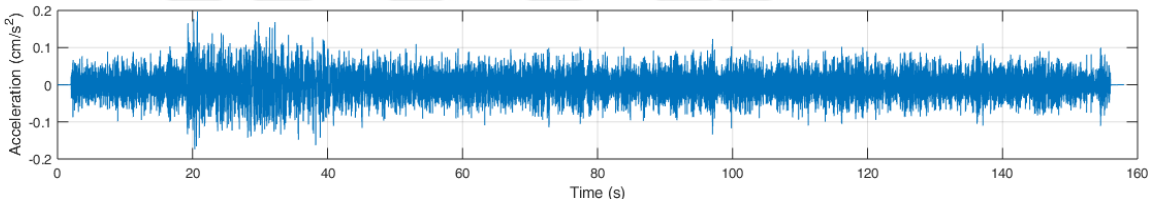

Figure 2.2. Example of a strong motion recording contaminated by ambient noise.

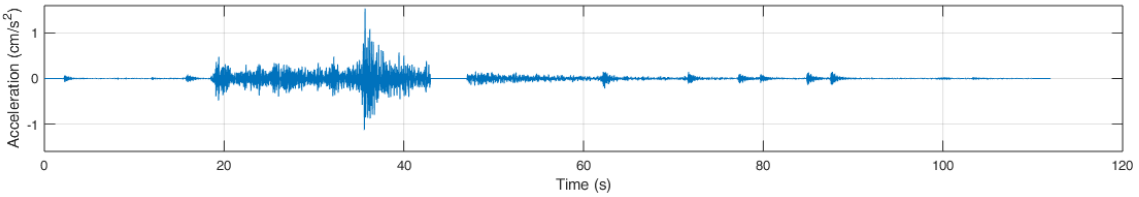

Figure 2.3. An example for partially truncated data.

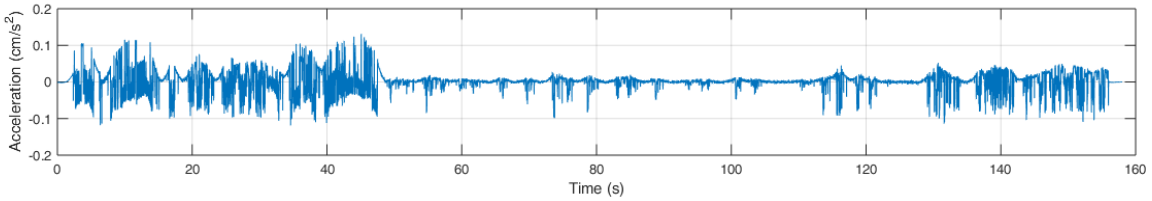

Figure 2.4. Example of a strong ground motion recording damaged because of technical issues related with the instrumentation.

The number of remaining earthquake records in the dataset after the visual inspection was 4677 (1559 × 3 components due to 50 earthquakes). The distribution of the remaining earthquakes which are used in further analyses are presented on a map in Figure 2.5. Moreover, Table 2.1 shows the location names, coordinates, and times of the occurances, along with other information associated with these events. Geographycally, studied earthquakes took place in the northwestern part of Anatolia. Their epicentral distances vary from 2 km up to 444 km. The selected earthquakes have local magnitudes ranging within $4<M_L<6.5$, while their depths range between 2.6-21.2 km (Table 2.1). Thereore, these earthquakes can be considered as shallow earthquakes.

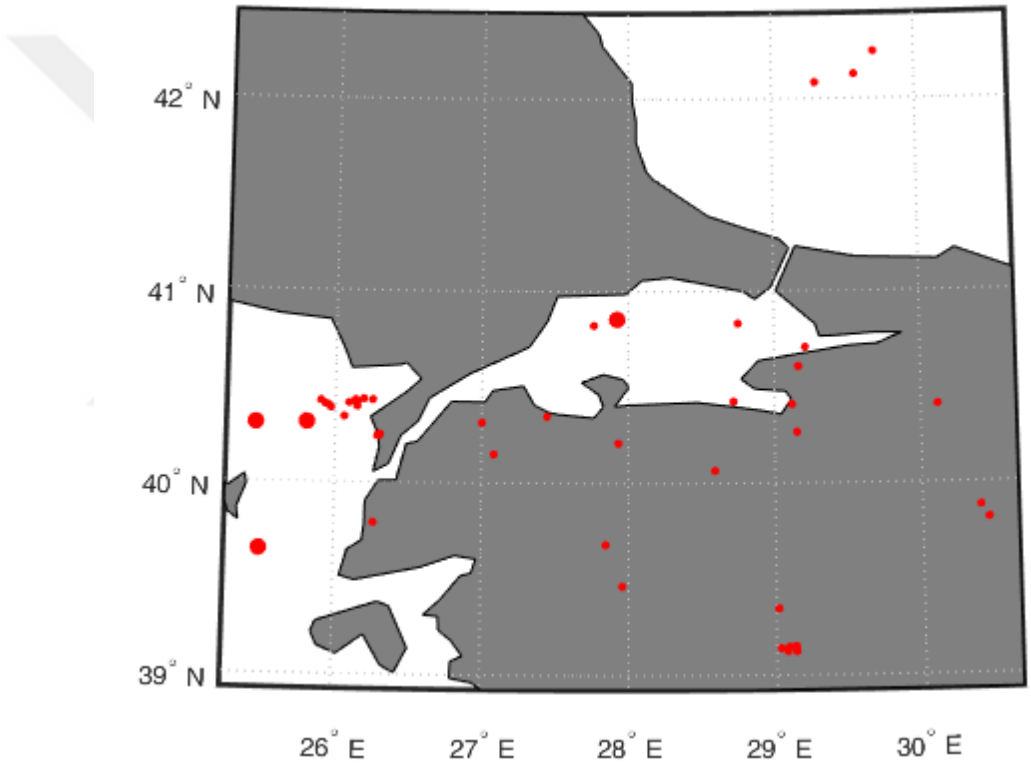

Figure 2.5. Distribution of the selected earthquakes.

By using 43 local magnitudes out of 50 earthquakes, moment magnitudes of which were estimated by Regional Earthquake-Tsunami Monitoring Center of Kandilli Observatory and Earthquake Research Institute, a simple regression model is prepared to estimate the moment magnitudes of remaining earthquakes (Figure 2.6). The model used by the Regional Earthquake-Tsunami Monitoring Center for estimating moment magnitude from local magnitude is given in Equation 2.1 (Pınar, personal commnication, 2018).

$$M_{w,i} = 0.91 \times M_{L,i} + 0.24 \quad (2.1)$$

Parolai et al. (2007), by using 523 earthquakes having magnitudes ranging between 0.5 and 5.9 (M_L), prepared a similar regression model for northwestern Turkey by fitting a second degree polynomial over the M_L-M_w graph (Equation 2.2). The model of Parolai et al. (2007) and the model employed by the Regional Earthquake-Tsunami Monitoring Center are presented in Figure 2.6.

$$M_{w,i} = 0.03 \times {M_{L,i}}^2 + 0.58 \times M_{L,i} + 0.95 \quad (2.2)$$

Geographically, only three of the earthquakes in our dataset occurred in the region considered by that Parolai et al. (2007). The significant difference between the functions is possibly due to this geographical difference. For this reason, to calculate the remaining five unestimated moment magnitudes, the functional form presented in Equation 2.1 was used. In Table 2.1 newly estimated five moment magnitude values are underlined.

The range of moment magnitudes of events in our dataset is between $3.6<M_w<6.8$.

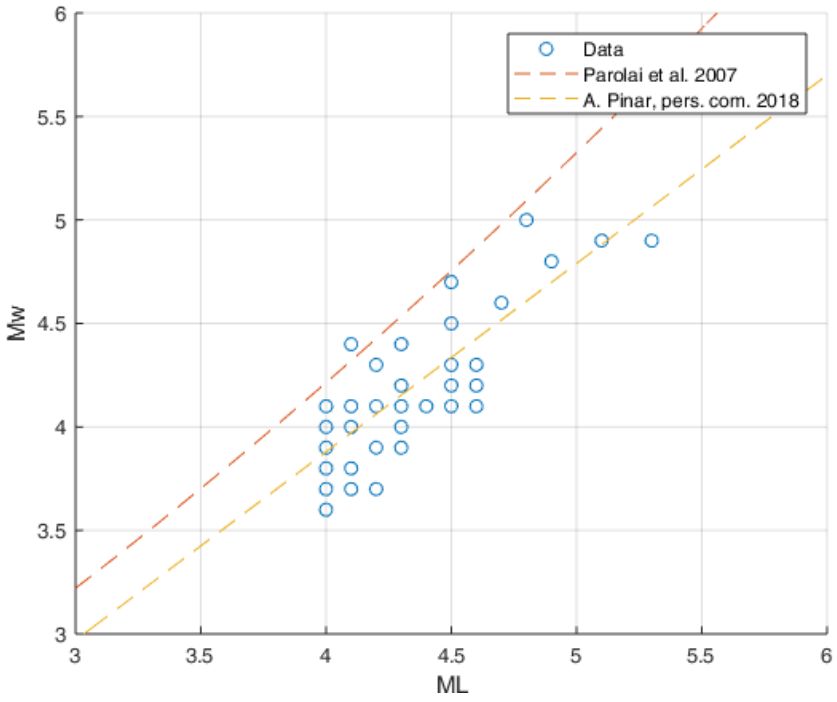

Figure 2.6. M_L-M_w regression models.

Table 2.1. Properties of the selected earthquakes.

Eq. No	Year	Month	Day	Time	Earthquake Location	Earthquake Latitude	Earthquake Longitude	M_L	M_W	Depth (km)
1	2012	4	16	13:10:46(10:10:46)	SIMAV (KUTAHYA)	39.1375	29.1312	4.8	4.6	5.3
2	2012	5	3	19:16:04(16:16:04)	SIMAV (KUTAHYA)	39.1237	29.0737	4.4	4.2	2.6
3	2012	5	4	00:45:17(21:45:17)	SIMAV (KUTAHYA)	39.1472	29.084	4.7	4.5	11.6
4	2012	5	4	08:38:13(05:38:13)	LAPSEKI (CANAKKALE)	40.3147	27.0005	4.3	3.9	12
5	2012	6	7	23:54:25(20:54:25)	MARMARA EREGLISI ACIKLARI	40.854	27.9235	5.1	4.9	14.9
6	2012	7	26	00:28:28(21:28:28)	SAROS KORFEZI	40.4325	26.1952	4.6	4.4	17.3
7	2012	10	26	06:37:36(03:37:36)	GEMLIK KORFEZI	40.4258	28.7203	4	3.6	8.3
8	2012	10	30	02:12:35(00:12:35)	SENKOY-SIMAV (KUTAHYA)	39.124	29.1338	4	3.9	13
9	2013	1	11	23:56:15(21:56:15)	SAROS KORFEZI	40.4243	25.9005	4.3	4.1	13
10	2013	3	19	14:44:30(12:44:30)	KARADENIZ	42.1267	29.5782	4.5	4.7	12
11	2013	7	12	03:36:57(00:36:57)	SAROS KORFEZI	40.386	25.9683	4.3	4.2	16.5
12	2013	7	30	08:33:08(05:33:08)	GOKCEADA(CANAKKALE)	40.3102	25.8067	5.3	4.9	13.2
13	2013	8	17	21:16:31(18:16:31)	GEMLIK(BURSA)	40.4103	29.1193	4.2	4.1	5.5
14	2013	8	29	09:20:34(06:20:34)	BIGA(CANAKKALE)	40.3478	27.4458	4.2	3.9	14.1
15	2013	11	27	06:13:37(04:13:37)	MARMARA E. ACIKLARI	40.8455	27.9187	4.7	4.6	10.8
16	2013	1	8	14:16:07(12:16:07)	EGE DENIZI	39.6482	25.4957	6.2	5.7	8
17	2014	1	10	09:20:46(07:20:46)	YESILDERE-BIGADIC (BALIKESIR)	39.4637	27.9588	4	4.1	12
18	2014	5	24	09:25:01(03:25:01)	EGE DENIZI	40.3043	25.458	6.5	6.8	21.2
19	2014	5	24	13:11:40(10:11:40)	SAROS KORFEZI	40.395	26.1485	4.3	4.4	9.4
20	2014	5	24	13:35:00(10:35:00)	SAROS KORFEZI	40.4278	26.1382	4.1	4.4	4.9
21	2014	5	24	17:49:14(14:49:14)	SAROS KORFEZI	40.3997	25.9523	4.6	4.3	5.6
22	2014	5	25	02:00:35(23:00:35)	SAROS KORFEZI	40.4067	25.9313	4.3	4.1	12
23	2014	5	25	14:38:38(11:38:38)	SAROS KORFEZI	40.4208	26.1515	4.8	5	13
24	2014	5	25	14:47:55(11:47:55)	SAROS KORFEZI	40.4123	26.0925	4.5	4.2	6.8
25	2014	5	28	06:59:51(03:59:51)	SAROS KORFEZI	40.4218	26.1343	4.5	4.3	13.2

Table 2.1. Properties of the selected earthquakes (continued).

Eq. No	Year	Month	Day	Time	Earthquake Location	Earthquake Latitude	Earthquake Longitude	M_L	M_w	Depth (km)
26	2014	7	3	08:04:46(05:04:46)	KUS GOLU(MANYAS)	40.2088	27.9333	4.5	4.3	11.8
27	2014	7	10	02:45:02(23:45:02)	SAROS KORFEZI	40.4298	26.2558	4.3	4	15
28	2014	8	4	01:22:44(22:22:44)	TERMAL (YALOVA)	40.6075	29.1652	4.1	3.8	11.5
29	2014	10	22	20:11:05(17:11:05)	TASOLUK-GEYVE (SAKARYA)	40.4065	30.1147	4.5	4.2	7.5
30	2014	11	28	04:30:06(02:30:06)	SIMAV (KUTAHYA)	39.3465	29.0165	4.5	4.5	3.9
31	2014	12	16	11:02:13(09:02:13)	CELTIK-BIGA (CANAKKALE)	40.1498	27.0835	4.4	4.1	12.9
32	2015	1	17	02:42:34(00:42:34)	KARACOBANPINARI-TEPEBASI (ESKISEHIR)	39.877	30.3947	4.2	4.3	7
33	2015	1	23	12:19:42(10:19:42)	MUSTAFAKEMALPASA (BURSA)	40.0657	28.5903	4.5	4.2	5
34	2015	2	2	06:41:03(04:41:03)	SAROS KORFEZI (EGE DENIZI)	40.3413	26.0612	4.1	4.1	13.1
35	2015	4	29	07:40:53(04:40:53)	KARADENIZ ACIKLARI	42.0845	29.3045	4	3.9	15.2
36	2015	7	3	01:22:26(22:22:26)	KABAKDERE-(BALIKESIR)	39.6805	27.847	4	3.8	5.5
37	2015	7	24	04:26:00(01:26:00)	ECEABAT (CANAKKALE)	40.2427	26.3025	4.5	4.3	11.2
38	2015	7	24	05:39:42(02:39:42)	ECEABAT (CANAKKALE)	40.2435	26.2873	4.9	4.8	11.9
39	2015	7	24	09:54:09(06:54:09)	ECEABAT (CANAKKALE)	40.2513	26.3053	4.6	4.2	10.7
40	2015	9	3	11:23:19(08:23:19)	SIMAV (KUTAHYA)	39.1485	29.131	4.1	4	10.5
41	2015	9	18	01:30:28(22:30:28)	TEPEBASI (ESKISEHIR)	39.8122	30.4488	4	3.7	8.7
42	2015	9	22	09:25:04(06:25:04)	SIMAV (KUTAHYA)	39.1505	29.1297	4.1	3.7	10.7
43	2015	9	22	10:11:11(07:11:11)	SIMAV (KUTAHYA)	39.1495	29.1292	4.1	4.1	11.7
44	2015	10	14	02:18:10(23:18:10)	SIMAV (KUTAHYA)	39.1407	29.0298	4.3	4.2	10.4
45	2015	10	26	23:07:59(20:07:59)	EZINE (CANAKKALE)	39.7903	26.2667	4.3	3.9	6.7
46	2015	10	28	19:20:02(16:20:02)	MARMARA DENIZI	40.822	27.7642	4.5	4.3	14.3
47	2015	11	16	17:45:43(15:45:43)	MARMARA DENIZI	40.8315	28.7535	4.2	3.7	12.6
48	2015	12	15	03:13:38(01:13:38)	KARADENIZ ACIKLARI	42.2452	29.7165	4	4	18.7
49	2016	6	7	07:09:45(04:09:45)	GURSU -BURSA	40.2652	29.1523	4.6	4.1	15.8
50	2016	6	25	08:40:11(05:40:11)	YALOVA ACIKLARI	40.7068	29.2122	4.5	4.1	9.3

2.2. Filtering

The recordings in the remaining dataset were bandpass filtered. The high-cut filter was fixed to 30 Hz. This decision was made because of the need of fitting a straight line on acceleration Fourier amplitude spectra along a relatively wide frequency range after f_{max} for kappa measurements.

Assigning a fixed low-cut filter value to records is widely applied in engineering studies. In general, correcting drifts in displacement time histories is usually a sufficient criterion to be able to accept records as useable or correct. For such needs however, generalizing and using a single low-cut filter for a certain dataset may result in two different cases: either a useful part beneath the fixed low-cut frequency value is lost or an unwanted noise distortion above the fixed low-cut frequency remains.

Malcıoğlu and Süleyman (2018) observed that the smallest useable frequency varies from record to record, which makes it difficult to accept a generally selected low-cut frequency. While the general aim for accepting a low-cut filter as applicable is to be sure if the displacement time history is unshifted from the reference zero-line (true for far field events), Malcıoğlu and Süleyman (2018) observes these shifts by fitting a straight line on displacement time histories and measuring the shift from the reference line as a polynomial function of time. Starting from 0.05 Hz, with 0.01 Hz increments, the amount of the shifts were observed systematically and plotted on shift-frequency graphs (Figure 2.7). Amount of shifts is usually so low that they cannot be visually observed. Our numerical approach, without the need of any individual visual inspection, returns the amounts of shifts with respect to frequencies where the observer can see the dissipation of fluctuations as the low-cut filter value increases (Figure 2.7). To be able to perform these estimations for each record, a semi-automated routine was prepared, which returns similar graphs (Figure 2.7) and allows the user to choose the optimum low-cut frequency level reliably. In the present study, instead of making assumptions on low-cut filter frequencies, the method of Malcıoğlu and Süleyman (2018) is used.

Initially, this method detrends all raw acceleration records. After detrending, the data were zero-padded at the beginning and at the end (Boore, 2005). Then, each record was bandpass filtered for 35 low-cut frequencies, varying between 0.05 Hz and 0.4 Hz with 0.01 Hz increments, while the high-cut corner frequency was fixed at 30 Hz. The resulting set of filtered records belonging to a single record were double integrated and the displacement time histories were obtained. Then, polynomial straight lines are fitted on the displacement graphs. In Figure 2.7, the changes in the initial point of a fitted line (the orange-colored line) and the changes in the final point (the blue-colored line) of a fitted line can be seen for each low-cut corner frequency value. In this example, the little red star represents the selected low-cut filter value that is above the low-cut frequency values where the displacement graph fluctuates. One of the remarkable outputs of this observation is that the change in those two points are almost exactly inversely proportional in all the cases.

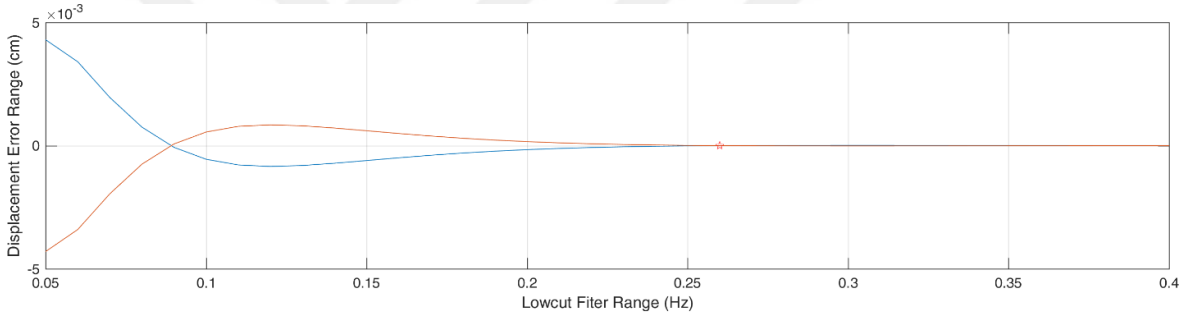

Figure 2.7. Displacement error range – low-cut filter range graph of a single record.

Figure 2.8, Figure 2.9 and Figure 2.10 show the number of records filtered in specific low-cut frequency bins, for north-south, east-west and vertical components respectively. Seven bins are considered representing ranges of 0.05-0.1 Hz, 0.1-0.15 Hz, 0.15-0.2 Hz, 0.2-0.25 Hz, 0.25-0.3 Hz, 0.3-0.35 Hz and 0.35-0.4 Hz. These graphs also show the high quality of the data. As can be seen in the figures, the majority of the data were low-cut filtered at frequencies within 0.05-0.1 Hz range, which mostly means that the noise contamination was relatively minor in those records. While almost two thirds of the whole dataset's low-cut frequency level was below 0.2 Hz, only one third of the dataset's low-cut frequency level was between 0.2-0.4 Hz. Another outcome of these graphs is that each of them follow the same statistical consistency, as the amount of the records filtered in each range is l similar when compared among three components. Moreover, for all components, the number of the

records follows a stable decrease, followed by an increase in the amount of the records as the filter ranges moves towards higher frequencies.

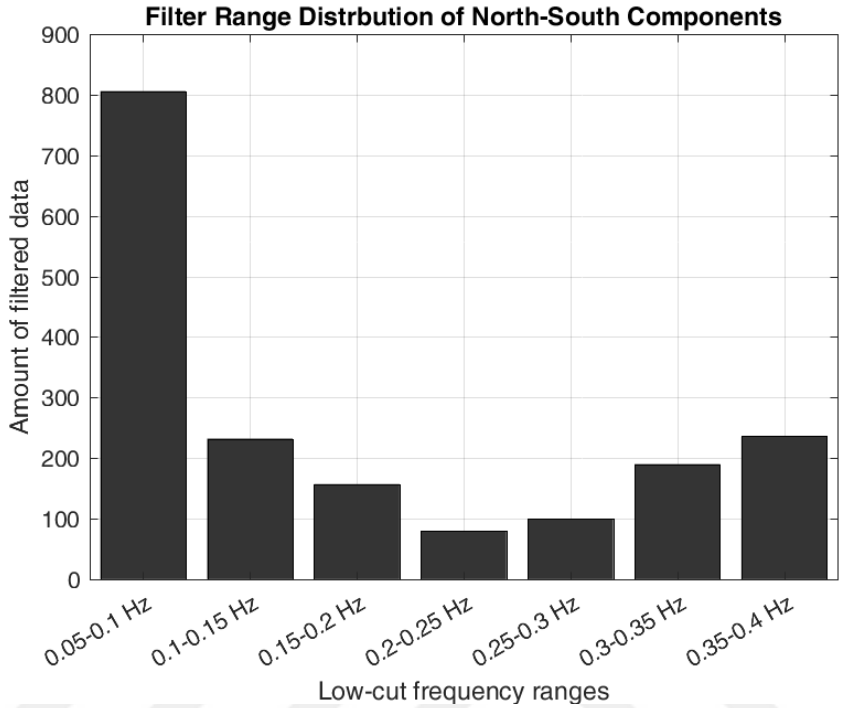

Figure 2.8. Filter range distribution of north-south components of the records.

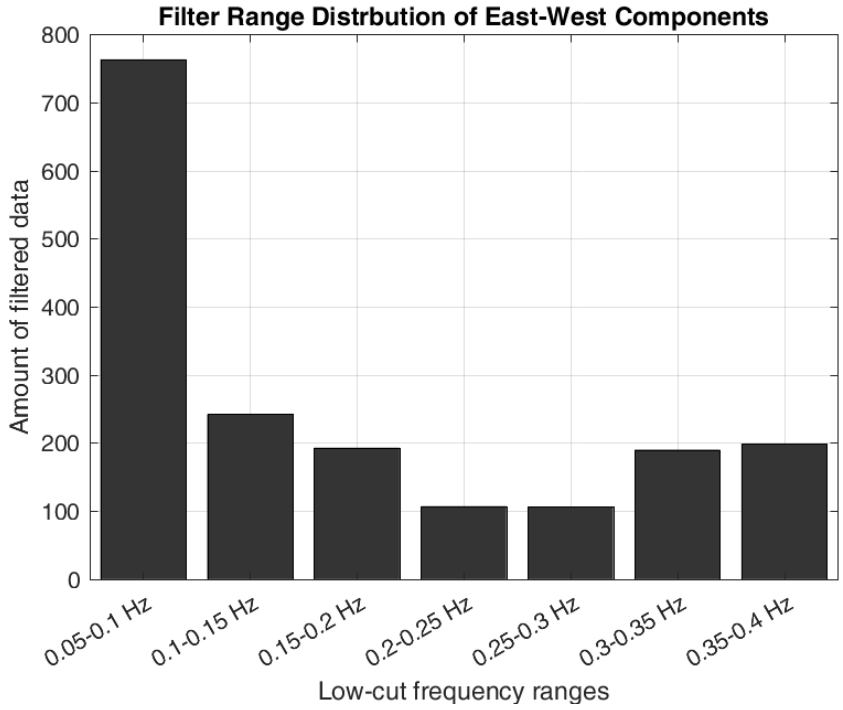

Figure 2.9. Filter range distribution of east-west components of the records.

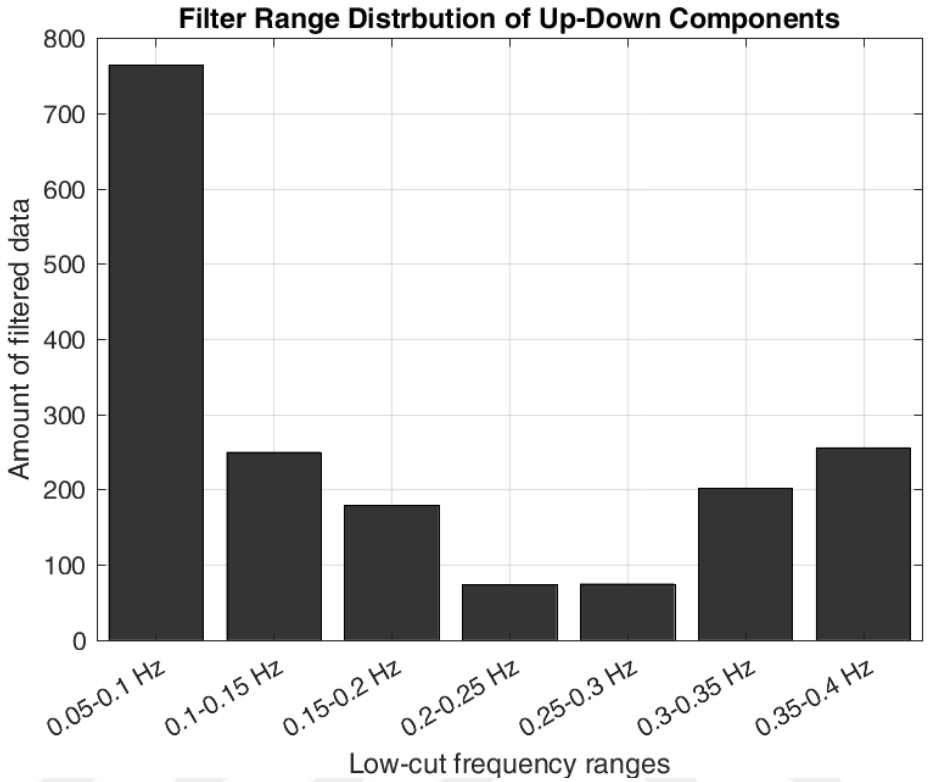

Figure 2.10. Filter range distribution of up-down components of the records.

2.3. S-wave Window Selection

Initial and final points of shear wave windows of 4677 records were visually selected (Figure 2.11; Figure 2.12; Figure 2.13). Because only the S-wave parts of records are to be considered in further analyses, we also made use of truncated records in which S-wave parts were undamaged (such as in Figure 2.3).

The vast majority of the records had lengths between 2-6 minutes. Exceptionally, some of the records were up to one hour long. Such long records are usually not available in most databases worldwide, which can make selection of noise portions difficult. By making use of the advantage of relatively long records, sufficiently long noise windows could be selected.

A routine was prepared in MATLAB for automated selection of noise windows from records. Initially, the routine defines the length of the noise window equal to the S-wave window. Then, it searches for the best amplitude combination that possibly belongs to noise, along the whole length of each record. For a given noise length and given number of trials, the routine sums the absolute value of relevant amplitudes and returns the lowest observed summation as the most suitable noise window option. Noise windows in Figure 2.11, Figure 2.12 and Figure 2.13 were automatically selected through this routine. It is particularly clear in Figure 2.11, that the routine has chosen the most optimal portions in comparison to the other parts of the record, which include minor shocks before and after the main shock.

To prevent possible deviations in auto-selection of the noise, they were also visually checked and corrected, whenever needed. Estimating the most optimum noise window through a computational approach also helps signal-to-noise ratios be higher, which further implies that the analysis results are more reliable.

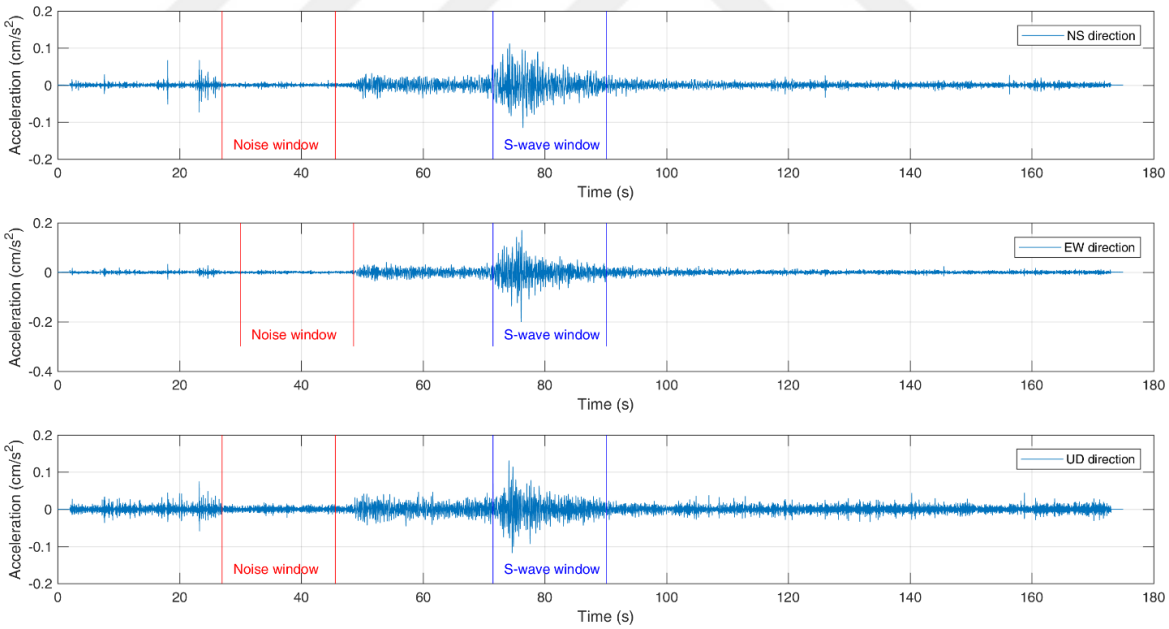

Figure 2.11. An example of three-component S-wave window and noise window selection process (NS: North-South, EW: East-West, UD: Up-Down).

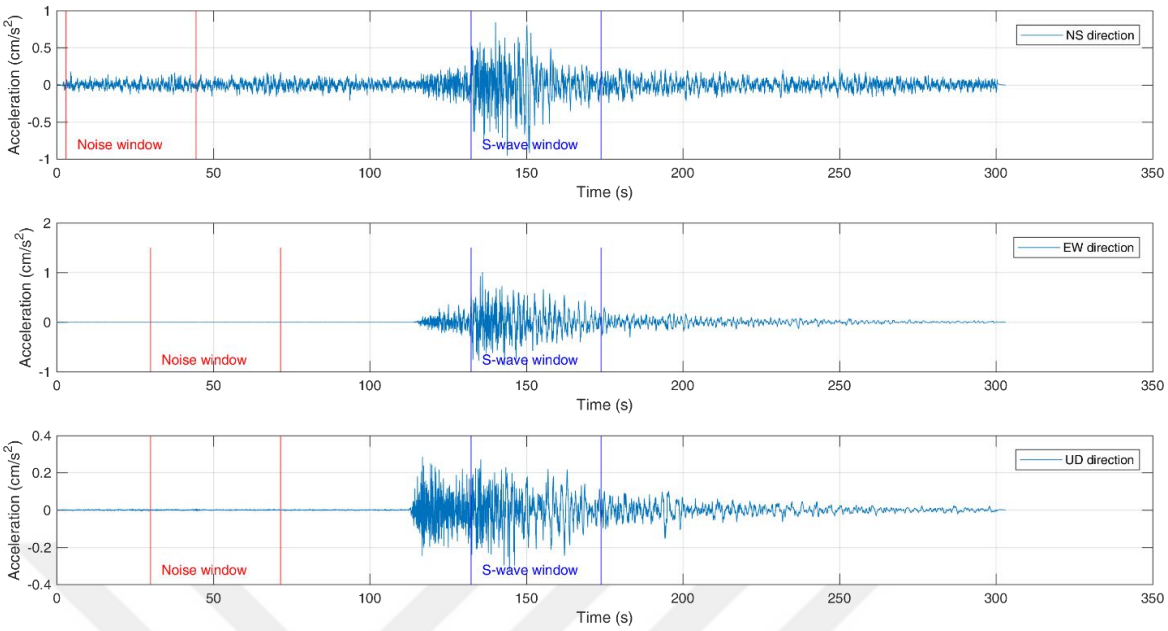

Figure 2.12. An example of three-component S-wave window and noise window selection process (NS: North-South, EW: East-West, UD: Up-Down).

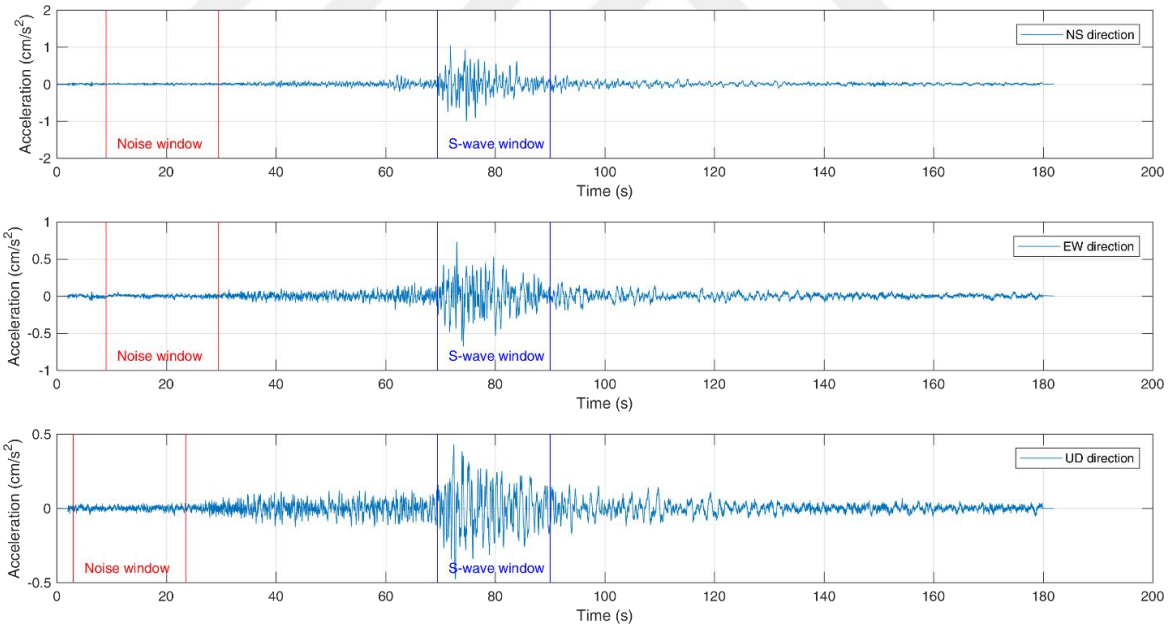

Figure 2.13. An example of three-component S-wave window and noise window selection process (NS: North-South, EW: East-West, UD: Up-Down).

2.4. Signal-to-Noise Ratio

Once noise and shear wave windows are ready, signal-to-noise ratios (SNR) can be estimated. Signal-to-noise ratio is defined as the ratio of summed squared magnitude of the signal to the summed squared magnitude of the noise (Equation 2.3).

$$SNR = \left(\frac{A_{signal}}{A_{noise}}\right)^2 \tag{2.3}$$

In this equation, A is the root-mean-square (RMS) amplitude.

The clear majority of our signals were desirably recorded. Low noise levels were visually observed, and also supported by SNR results. Only 100 records out of 4677 were found to be under the SNR level of 3. Average SNR's of north-south and east-west components were around 27, while the average SNR of up-down components was around 21. Another remarkable observation was that the SNR levels of some of the records were up to 120. Table 2.2 shows the number of records below the level of 3. In further analyses, they were excluded.

Table 2.2 Number of remaining records after visual inspection and SNR analysis.

Record components	**Number of records after visual inspection**	**Number of records below SNR of 3**	**Number of records above SNR of 3**
North-South	1559	19	1540
East-West	1559	20	1539
Up-Down	1559	61	1498
Total:	**4677**	**100**	**4577**

2.5.Cosine Tapering

A cosine taper function of 10% width was applied in time domain to all 4577 records. This process aims to minimize discontinuities at the beginnings and at the ends of records by creating smooth edges on both sides. When records in time domain are cut into shorter time windows without tapering, this may distort the observed spectrum.

3. SITE RESPONSE CHARACTERISTICS

3.1. Geological Setting

Istanbul is mainly on Paleozoic bedrock, which consists of various Devonian and Ordovisian formations. Figure 3.1 shows the geological setting of the European side of the city. In this figure, geologically weak sediments -which are Holocene formations in the southern and western parts- are shown with light grey color. As explained on the figure, this region is separated into eight geological timescales as: late, middle and early Miocene, Oligocene, middle and late Eocene, Carboniferous and Quaternary. Quaternary sediments are mostly composed of alluvial deposits (OYO International Corporation, 2007).

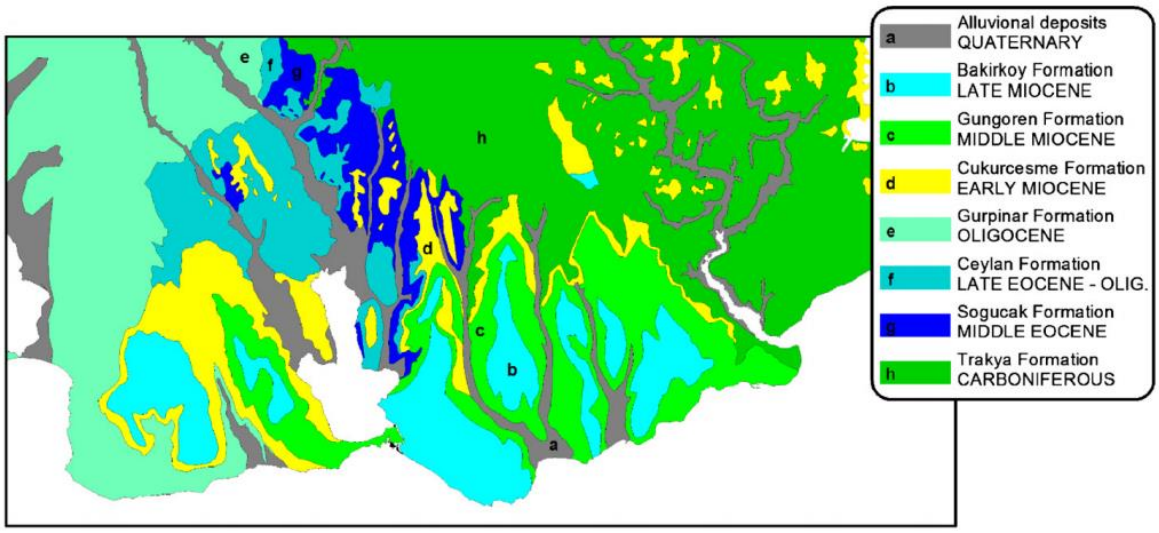

Figure 3.1. Geological setting of the European side of Istanbul (from Picozzi et al., 2009).

Similar to the European side of the city, the Asian side also consists of sediments from similar geological formations (OYO International Corporation, 2009): middle and late Miocene, lower, mid and upper Devonian, lower Ordovician, Carboniferous and Quaternary (Figure 3.2). In contrast to the European side, on the Asian side the alluvial deposits (greyish colors) are not seen in large geographical areas. Rather, they are distributed across the region in small parts. They are most intensely seen in western part of the Maltepe district. Devonian and Ordovician type formations (brownish and purplish colors) are dominating the Asian

side of the city. Miocene type of formations (yellowish colors) are mainly distributed in Ataşehir, Samandıra, Sultanbeyli and Pendik districts.

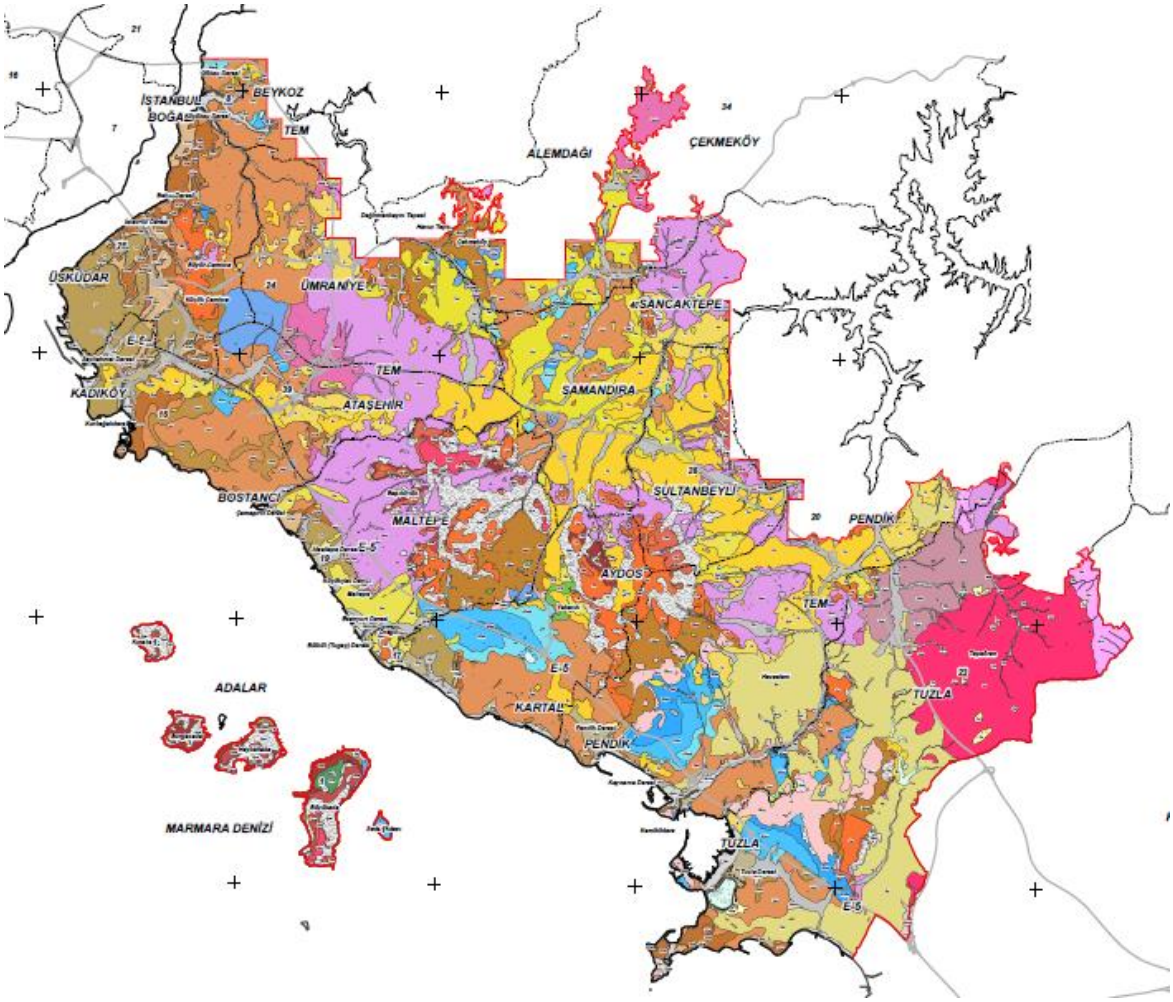

Figure 3.2. Geological setting of the Asian side of Istanbul (adopted from Istanbul Metropolitan Municipality, 2009).

3.2. Horizontal-To-Vertical Spectral Ratios

Nakamura (1989) proposed the horizontal-to-vertical (H/V) spectral ratio method for estimating site response characteristics. This method aims to get the average H/V spectrum for each station by proportioning and averaging horizontal and vertical components in frequency domain (Equation 2.4). Among the studies showing the efficiency of H/V spectral ratio method, Lermo and Chavez-Garcia (1993) expressed it as a simple and stable indicator

of site amplification. The general agreement among researchers is that the outcome of this method can generally be associated with soil amplification effects.

$$\left(\frac{H}{V}\right)(f) = \frac{\sqrt{H_1(f) \times H_2(f)}}{V(f)} \tag{2.4}$$

Figure 3.3 shows the average H/V spectral ratios of all stations. The upper limit of the frequency axis is fixed to 15 Hz. At most stations average maximum amplitudes are found to be below 6-7 Hz. The upper limit of the vertical axis is set to 7 Hz. In some stations amplitude values are much higher than in others. Some of the stations (i.e. OBO3, OBO4 and OBO5) are installed beneath the sea level, on the seabed close to the segments of the North Anatolian Fault within the Marmara Sea, which is one of the reasons of observing higher amplitudes. In some of the stations we had one or two three-component recordings. The higher amplitudes in these stations cannot be taken as a reliable representation of average H/V spectral ratio. Moreover, high amplitudes observed in some stations were thought to possibly due to the instrumental issues. In 32 stations out of a total of 115, the number of three-component recordings is 4 or below. 7 out of 32 stations do not have any data (Figure 3.3).

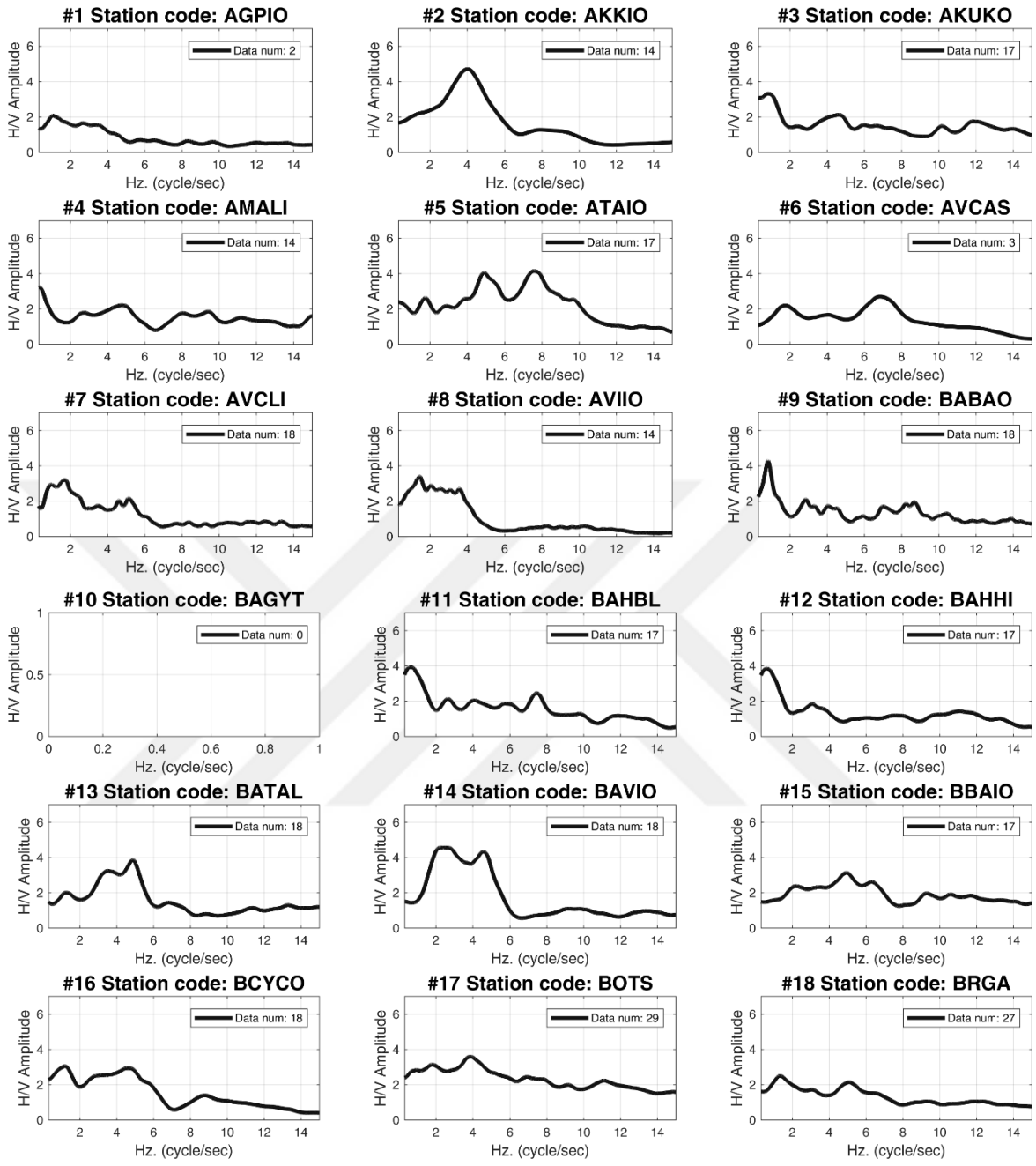

Figure 3.3. Average H/V spectral ratios.

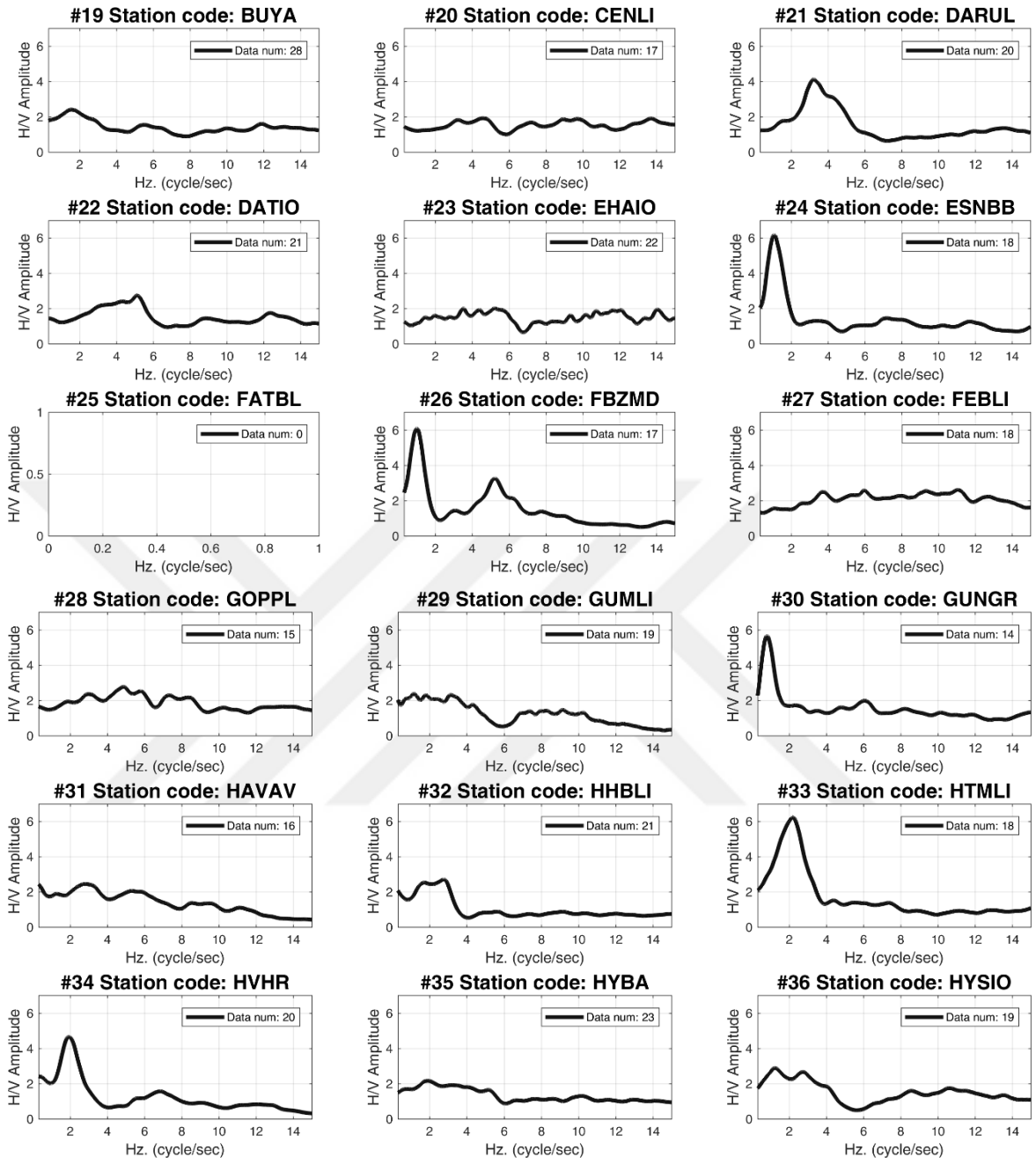

Figure 3.3. Average H/V spectral ratios (continued).

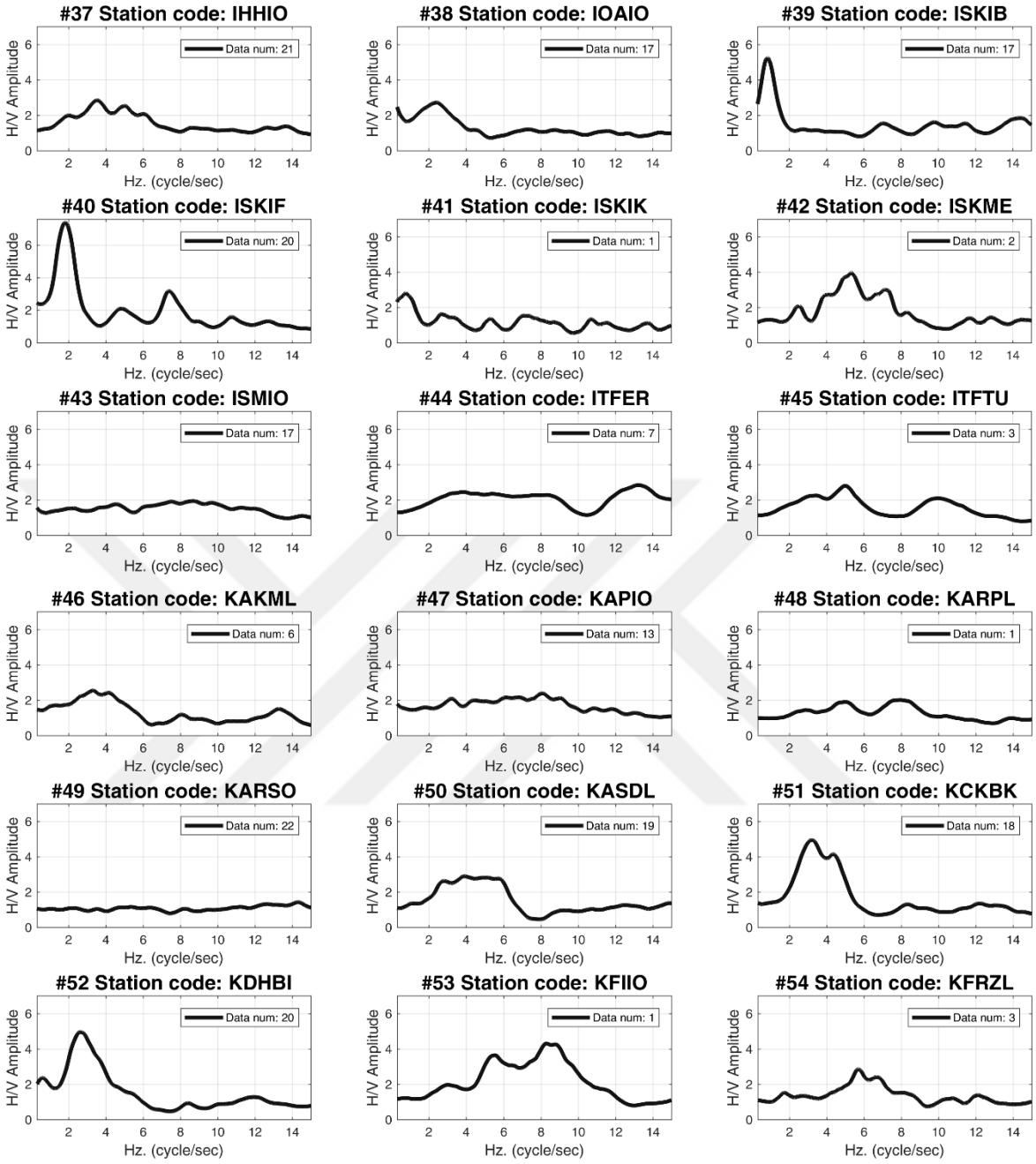

Figure 3.3. Average H/V spectral ratios (continued).

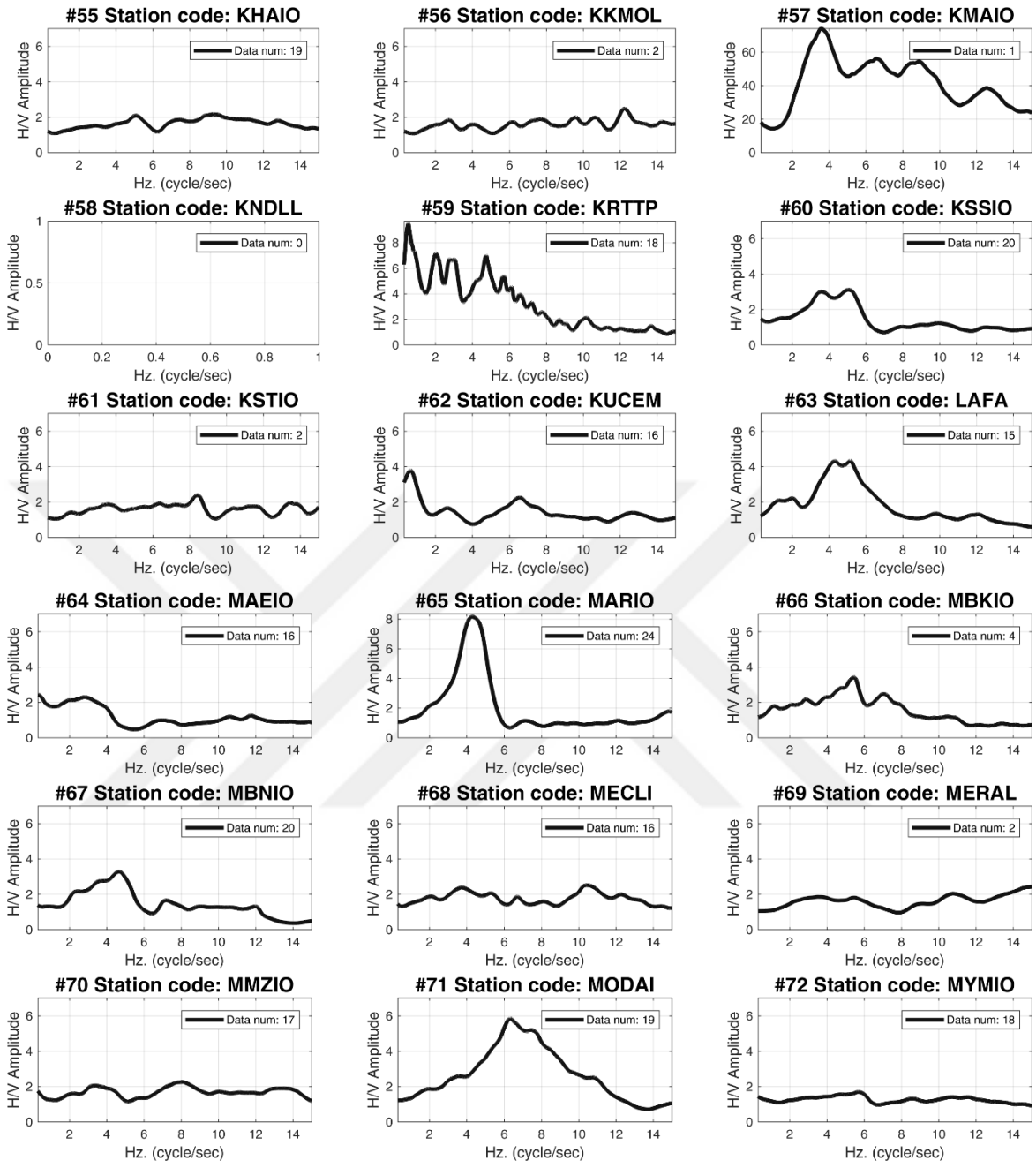

Figure 3.3. Average H/V spectral ratios (continued).

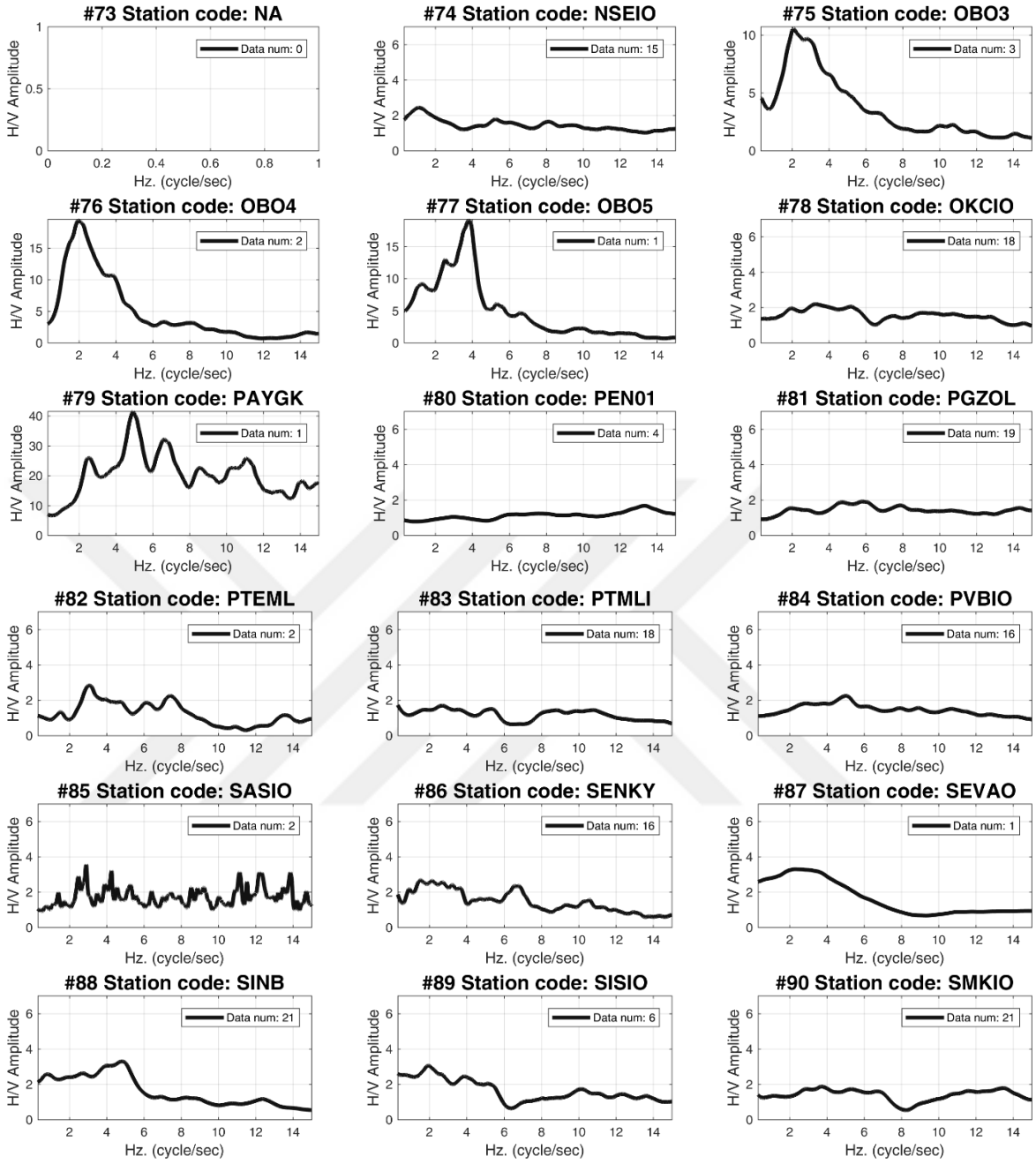

Figure 3.3. Average H/V spectral ratios (continued).

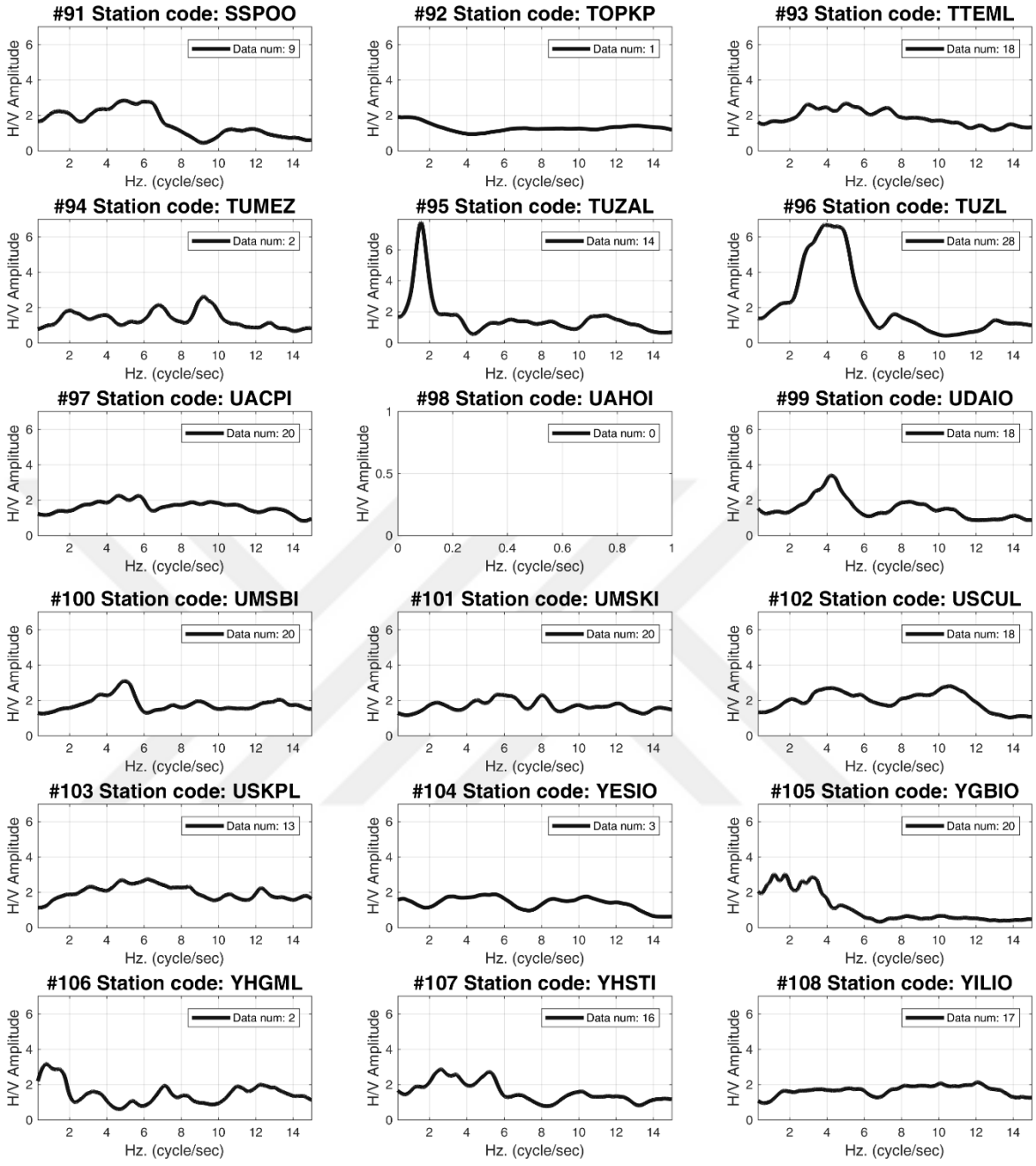

Figure 3.3. Average H/V spectral ratios (continued).

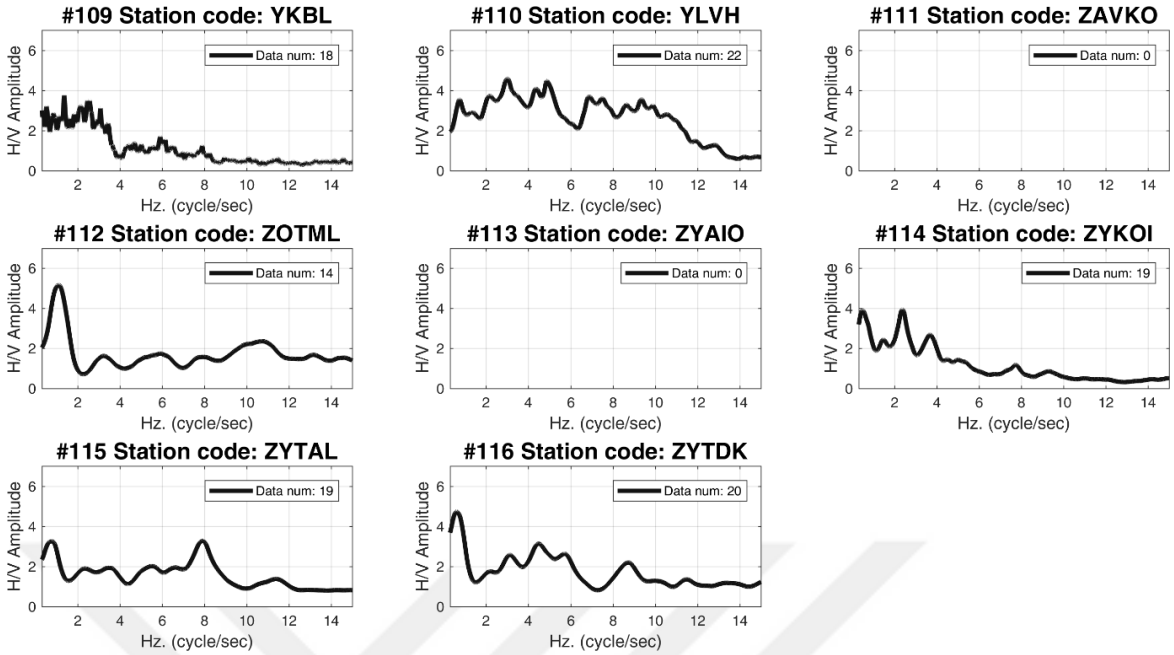

Figure 3.3. Average H/V spectral ratios (continued).

3.3. Fundamental Frequencies

Fundamental frequencies of average H/V spectral ratios were manually selected from the graphs. During the selection process, stations having no, one or two event recordings were excluded. Despite the sufficient amount of recordings and the reliable estimations, it was difficult or sometimes even impossible to select a frequency value associated with the maximum spectral amplitude as in the case shown in Figure 3.4a. Also, in just a few of the cases, the estimations were not found reliable due to the inconsistencies introduced by an individual H/V spectral ratio, as in the case shown in Figure 3.4b. In both cases, average H/V spectral ratios are shown with bold red lines.

The total number of stations where fundamental frequencies could be selected was 82. The average number of three-component data in these stations was around 17, which is sufficient enough for reliable H/V estimations. In 32 out of 82 stations, two fundamental frequency values were selected, because of the observed multiple peaks. Table 3.1 shows the details of the process: the amount of the data used, observed maximum average amplitudes; and primary and secondary fundamental frequencies in Hz.

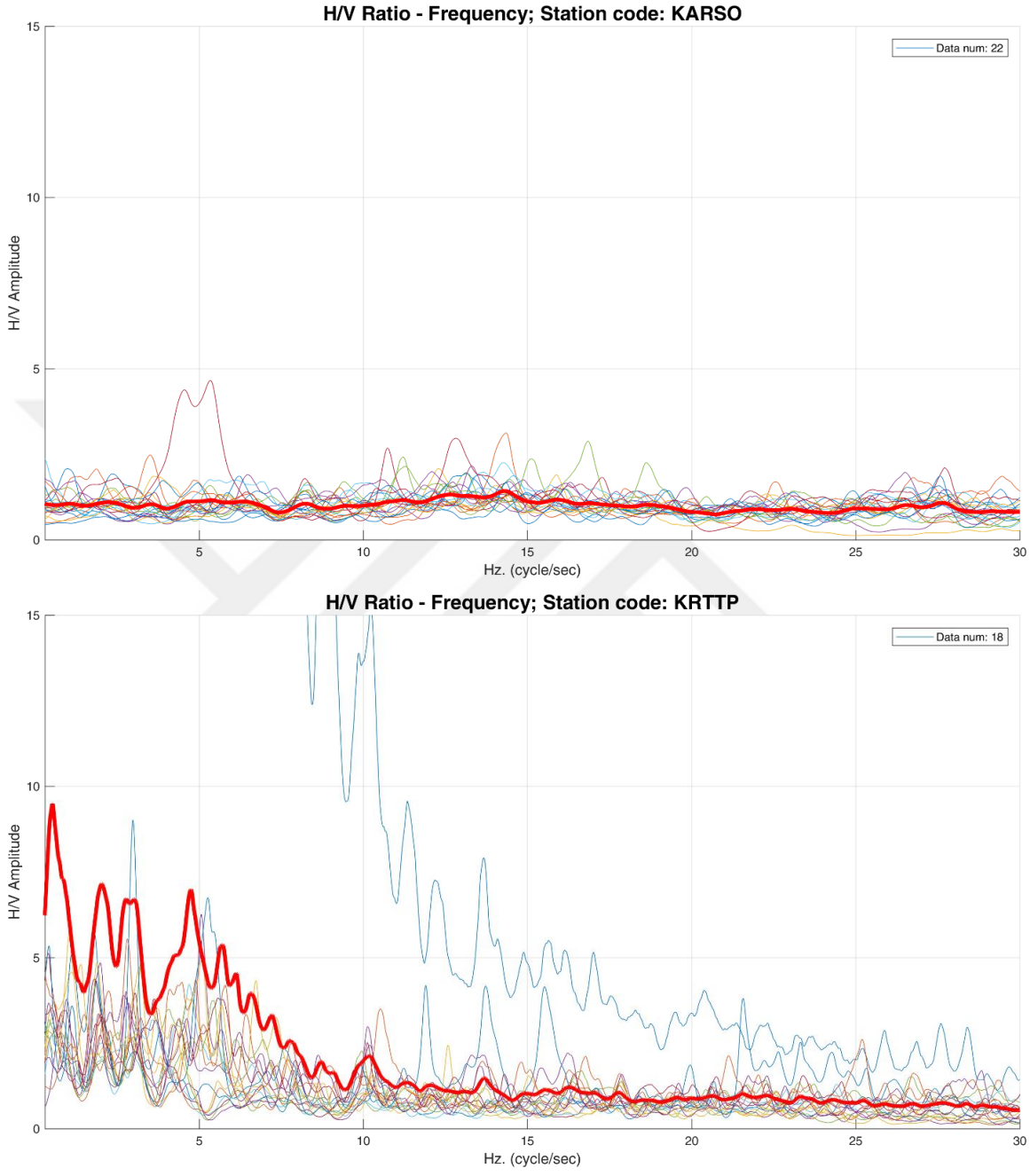

Figure 3.4. H/V spectral ratio estimation in KARSO station; H/V spectral ratio estimation in KRTTP station.

Table 3.1. Fundamental frequencies estimated from H/V spectra.

Station Number	Station Name	Num. of Data	Maximum Amplitude	Fund. Frequency	Second Order Fund. Frequency	NEHRP Site Class
1	AGPIO	2	2.09	-	-	B
2	AKKIO	14	4.69	4.06	-	B
3	AKUKO	17	3.31	0.91	-	B
4	AMALI	14	3.23	0.40	4.83	D
5	ATAIO	17	4.14	4.74	7.70	D
6	AVCAS	3	2.69	1.73	6.90	D
7	AVCLI	18	3.19	1.48	5.00	D
8	AVIIO	14	3.39	1.48	3.64	D
9	BABAO	18	4.27	0.83	-	B
10	BAGYT	0	-	-	-	B
11	BAHBL	17	3.91	0.74	-	B
12	BAHHI	17	3.84	0.65	-	B
13	BATAL	18	3.87	4.83	-	B
14	BAVIO	18	4.56	2.39	4.66	D
15	BBAIO	17	3.13	5.00	-	B
16	BCYCO	18	3.04	1.05	4.74	D
17	BOTS	29	3.58	3.81	-	Unknown
18	BRGA	27	2.49	1.31	5.00	D
19	BUYA	28	2.40	1.65	-	B
20	CENLI	17	1.92	4.57	-	B
21	DARUL	20	4.12	3.24	-	B
22	DATIO	21	2.74	5.11	-	B
23	EHAIO	22	2.02	5.34	-	B
24	ESNBB	18	6.17	1.08	-	B
25	FATBL	0	-	-	-	B
26	FBZMD	17	6.08	0.97	-	B
27	FEBLI	18	2.61	3.69	10.73	D
28	GOPPL	15	2.77	4.83	-	B
29	GUMLI	19	2.91	1.17	3.18	D
30	GUNGR	14	5.65	0.80	-	B
31	HAVAV	16	2.55	2.88	5.45	D
32	HHBLI	21	2.74	1.71	3.25	D
33	HTMLI	18	6.24	2.16	-	B
34	HVHR	20	4.65	1.99	-	B
35	HYBA	23	2.16	1.90	5.28	D
36	HYSIO	19	2.88	1.28	2.70	D
37	IHHIO	21	2.84	3.49	-	B
38	IOAIO	17	2.77	2.42	-	B
39	ISKIB	17	5.24	0.85	-	B
40	ISKIF	20	7.40	1.85	-	B
41	ISKIK	1	2.82	-	-	B
42	ISKME	2	3.96	-	-	B
43	ISMIO	17	2.02	-	-	B
44	ITFER	7	2.84	3.78	8.32	D
45	ITFTU	3	2.79	5.08	-	B
46	KAKML	6	2.56	3.35	-	B
47	KAPIO	13	2.45	-	-	B

Table 3.1. Fundamental frequencies estimated from H/V spectra (continued).

Station Numbe	Station Name	Num. of Data	Maximum Amplitude	Fund. Frequency	Second Order Fund. Frequency	NEHRP Site Class
48	KARPL	1	2.01	-	-	B
49	KARSO	22	1.84	-	-	B
50	KASDL	19	2.90	2.81	5.48	D
51	KCKBK	18	4.95	3.15	4.35	D
52	KDHBI	20	4.94	2.70	-	B
53	KFIIO	1	4.30	-	-	B
54	KFRZL	3	2.85	5.74	-	B
55	KHAIO	19	2.16	5.20	9.34	D
56	KKMOL	2	2.48	-	-	B
57	KMAIO	1	73.93	-	-	B
58	KNDLL	0	-	-	-	B
59	KRTTP	18	9.49	-	-	B
60	KSSIO	20	3.11	3.61	5.14	Unknown
61	KSTIO	2	2.37	-	-	B
62	KUCEM	16	3.77	0.65	-	B
63	LAFA	15	4.31	4.69	-	Unknown
64	MAEIO	16	2.43	2.81	-	B
65	MARIO	24	8.17	4.35	-	B
66	MBKIO	4	3.41	5.43	-	B
67	MBNIO	20	3.28	4.69	-	B
68	MECLI	16	2.51	3.69	-	B
69	MERAL	2	2.48	-	-	B
70	MMZIO	17	2.25	3.35	-	B
71	MODAI	19	5.83	6.36	-	B
72	MYMIO	18	1.69	-	-	B
73	NSEIO	15	2.43	1.17	-	B
74	OBO3	3	10.51	2.44	-	Unknown
75	OBO4	2	19.37	-	-	Unknown
76	OBO5	1	19.06	-	-	Unknown
77	OKCIO	18	2.19	3.21	5.20	D
78	PAYGK	1	41.39	-	-	B
79	PEN01	4	1.67	-	-	B
80	PGZOL	19	1.91	-	-	B
81	PTEML	2	2.83	-	-	B
82	PTMLI	18	2.29	2.59	5.48	D
83	PVBIO	16	2.24	5.08	-	B
84	SASIO	2	3.99	-	-	B
85	SENKY	16	2.69	1.68	6.67	D
86	SEVAO	1	3.30	-	-	B
87	SINB	21	3.29	4.77	-	B
88	SISIO	6	3.17	1.90	-	B
89	SMKIO	21	1.87	3.75	6.70	D
90	SSPOO	9	2.83	5.28	-	B
91	TOPKP	1	1.90	-	-	B
92	TTEML	18	2.66	2.98	5.14	D
93	TUMEZ	2	2.62	-	-	B
94	TUZAL	14	7.75	1.54	-	B
95	TUZL	28	6.69	3.98	-	B
96	UACPI	20	2.24	4.74	-	B

Table 3.1. Fundamental frequencies estimated from H/V spectra (continued).

Station Numbe	Station Name	Num. of Data	Maximum Amplitude	Fund. Frequency	Second Order Fund. Frequency	NEHRP Site Class
97	UAHOI	0	-	-	-	B
98	UDAIO	18	3.38	4.20	-	B
99	UMSBI	20	3.09	5.00	-	B
100	UMSKI	20	2.32	5.74	-	B
101	USCUL	18	2.81	4.03	10.39	D
102	USKPL	13	2.74	5.68	-	B
103	YESIO	3	1.88	-	-	B
104	YGBIO	20	3.03	1.34	3.07	D
105	YHGML	2	3.16	-	-	B
106	YHSTI	16	2.86	2.81	5.20	D
107	YILIO	17	2.13	-	-	B
108	YKBL	18	3.69	1.34	2.56	D
109	YLVH	22	4.49	2.95	4.94	Unknown
110	ZAVKO	0	-	-	-	B
111	ZOTML	14	5.11	1.14	-	B
112	ZYAIO	0	-	-	-	B
113	ZYKOI	19	3.81	0.48	2.42	D
114	ZYTAL	19	3.21	0.74	7.90	D
115	ZYTDK	20	4.59	0.65	4.49	D

Figure 3.5 shows the interpolated distribution of primary resonance frequencies on the European side of Istanbul using information from 43 stations. A general decrease is observed in resonance frequencies from north towards south. One of the exceptions that is not following this pattern is the station ATAIO (in south part on the map) where the resonance frequency is much higher than the surrounding region. This is rather unexpected because this station is located on alluvial deposits. By comparing the fundamental frequencies of the stations with underlying soil conditions, it is seen that in most of the stations the agreement of them with geology is quite good.

Picozzi et al. (2009), by making use of ambient noise and two earthquake records of the western stations of the IERRS estimated H/V spectral ratios for the European part of Istanbul. It is worth mentioning that despite the limited number of records employed in Picozzi et al. (2009), the H/V estimations of the two studies show a general agreement. Zülfikar et al. (2012), used some the stations of IERRS located in the historical part of Istanbul, which is in the European side of the city. Their all fundamental frequency estimations in these stations are below 5 Hz, similar to ours. As seen in Figure 3.5, none of our fundamental frequency estimations in the European side is above 5 Hz. Another overlapping estimation between Zülfikar et al. (2012) and our study is that in some of the

stations with D type site classes, unexpectedly, the fundamental frequencies are between 4-5 Hz.

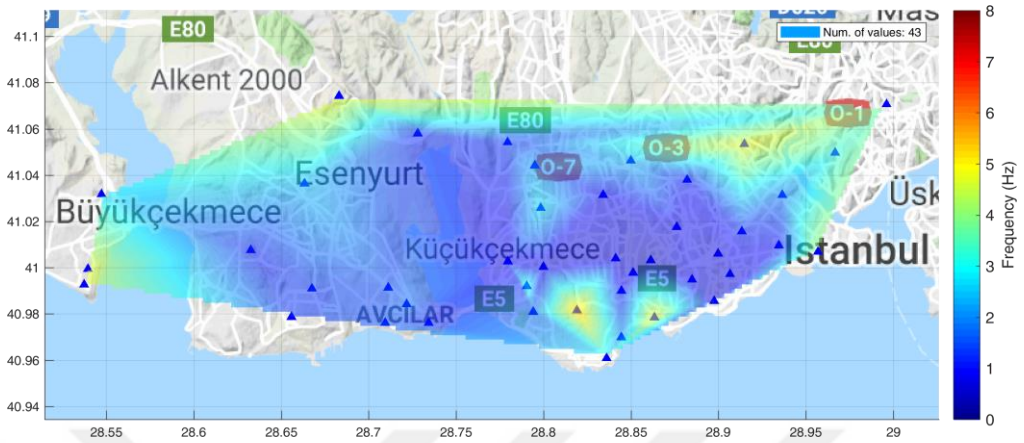

Figure 3.5. Map of resonance frequencies estimated for the European side of Istanbul.

In Figure 3.6, the interpolated distribution of primary resonance frequencies along the Asian side of the city is presented through 33 stations. Fundamental frequencies in the north-western part are relatively high, as well as in some southern regions. We also see that the frequency distribution changes irregularly along the map (Figure 3.6), just as the geological settings of this region variate.

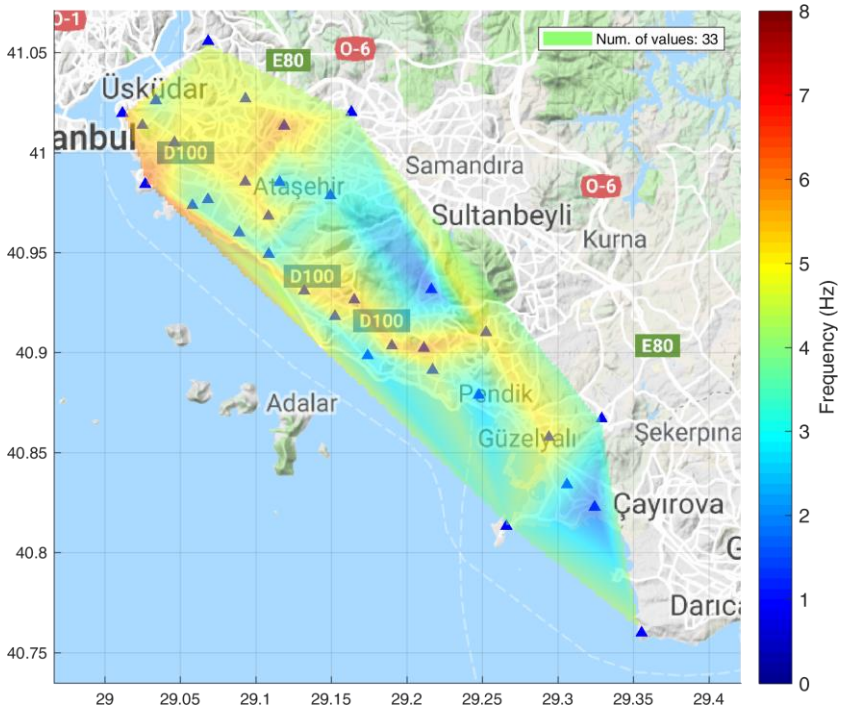

Figure 3.6. Map of resonance frequencies estimated for the Asian side of Istanbul.

4. THE HIGH FREQUENCY DECAY PARAMETER κ (KAPPA)

4.1. Methodology

Amplitudes of acceleration spectra of shear waves at higher frequencies are subjected to a rapid decay, above the frequency called f_{max} (Hanks, 1982). Hanks defined this decay with the term f_{max}. Different from Hanks's approach, Anderson and Hough (1984) define this decay with a fitted straight line on the observed amplitude decay which they name as kappa (κ). They fitted κ over the amplitudes above the frequencies higher than f_e, which is a subjectively selected parameter on acceleration spectra, slightly different from the theoretical f_{max}. κ is calculated related to the slope of the fitted line as,

$$\kappa = -\frac{\lambda}{\pi} \tag{4.1}$$

$$\lambda = \frac{\Delta(lna)}{\Delta f} \tag{4.2}$$

Anderson and Hough (1984), use the observed κ values for its distance dependence analysis. The linear increment of κ with distance is modeled as,

$$\kappa_r = \kappa_0 + m \times R \tag{4.3}$$

where κ_0 is the intersection of the observed linear fit at zero distance, while m is the slope of the linear fit and R is the distance. κ_0 is defined as a near-surface parameter, attributed to the attenuation of shear waves while traveling along the near-surface geological structure.

It is expected that harder sites should have lower attenuation and κ_0 should also decrease as the shear-wave velocity increases. When V_{S30} values are available, κ_0 is usually correlated with those values (Van Houtte et al., 2011; Ktenidou et al., 2013). To make such

a correlation meaningful enough, κ_0 should be compared with several site classes because of the large scatter in the data (Ktenidou et al., 2014).

Several studies show that the selection of κ by fitting a straight line on amplitude spectra involves not only site and path properties, but also source properties (Tsai and Chen, 2000; Van Houtte et al.,2011, among others). In most of them, the source contribution is related to the scatter of κ measurements (Ktenidou et al., 2014).

4.2. Measuring Criteria

Following the approach of Anderson and Hough (1984), κ_r was directly measured by fitting a straight line in semi logarithmic space of the Fourier amplitude spectra of horizontal and vertical components of the shear waves.

Shear wave amplitude spectra were plotted within the bandpassed frequency ranges. Our low-cut frequency levels varied in every record, while the high-cut frequency was fixed to 30 Hz. Despite the fact that the frequency range used in estimations was usually quite long, in order to make shorter ones reliable, entire spectra were slightly smoothed.

The length of the fitted straight line was not shorter than 8 Hz, but usually much above this level (Figure 4.1). In this study, the average frequency range of the fitted line selection for north-south and east-west components was 14.89 Hz and 14.87 Hz respectively; while the average fitting range for the vertical component was 14.20 Hz.

In order to exclude the unwanted manipulation of noise, related spectra of noise windows were also plotted beneath the shear wave spectra. Thus, the involvement of the noise at higher frequencies could be seen clearly. and the selected range for fitting the straight line was left within frequencies where the shear wave was clearly dominant.

As mentioned earlier, to avoid any trade-off with the source while measuring κ_r, source corner frequency (f_c) levels are expected to be low. The scaling law of Aki (1967) expressed the inversely proportional relation between event magnitude and source corner frequency.

For such a purpose, f_c was calculated for each record through the approach of Andrews (1986), as shown in the equation 4.4. Ktenidou et al. (2016) proposed to measure κ_r above $1.5 \times f_c$ level, which we applied to every single κ_r measurement.

$$f_c = \frac{\sqrt{\frac{S_v}{S_d}}}{2\pi} \tag{4.4}$$

where S_v and S_D are the integral sums of velocity and displacement spectra respectively. With the help of the estimated H/V spectral ratio estimations, possible biases while measuring κ_r were avoided. In the cases where resonant peaks were strong, κ_r was measured after or before them. In some cases, strong peaks were avoided by measuring κ_r over a wide frequency range so that it crossed a single peak or several peaks while the measurement was not biased.

Two straight line fitting options were applied at the same time. While the red colored fittings (Figure 4.1) represent the standard first-degree polynomial fitting, the other first-degree polynomial fittings represented with blue color (Figure 4.1) provides an additional robust option which is less effected by the fluctuations and peaks along the observed range. While estimated κ_r values through both fittings were usually close, the one being closer to represent the decreasing trend was assigned as a representative κ_r value.

During this process, we could measure kappa effectively along the whole dataset except for 75 records of which FAS's were biased by noise contamination. In these cases, the usable frequency range for measuring kappa was usually less than 8 Hz.

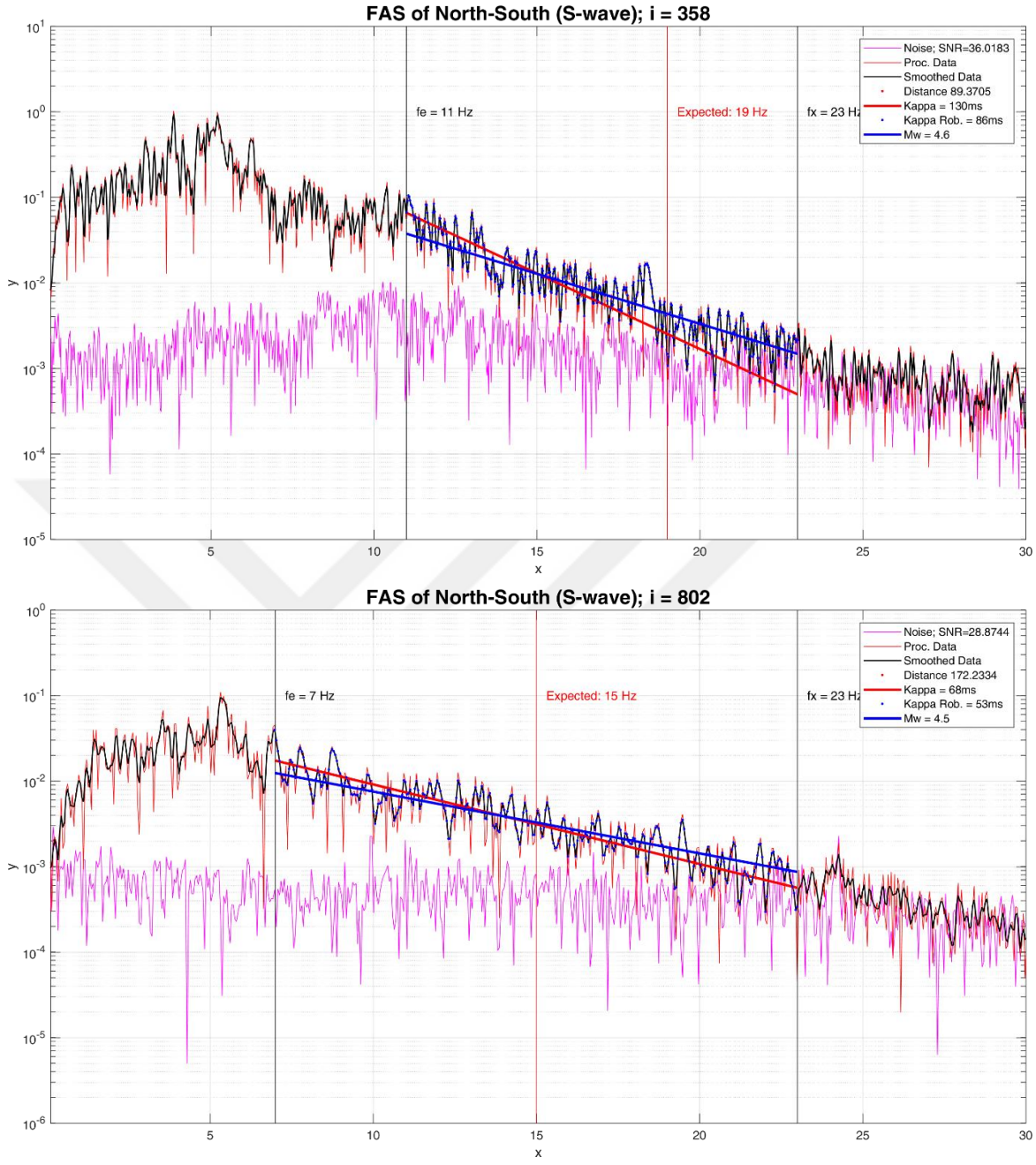

Figure 4.1. Sample κ_r measurements.

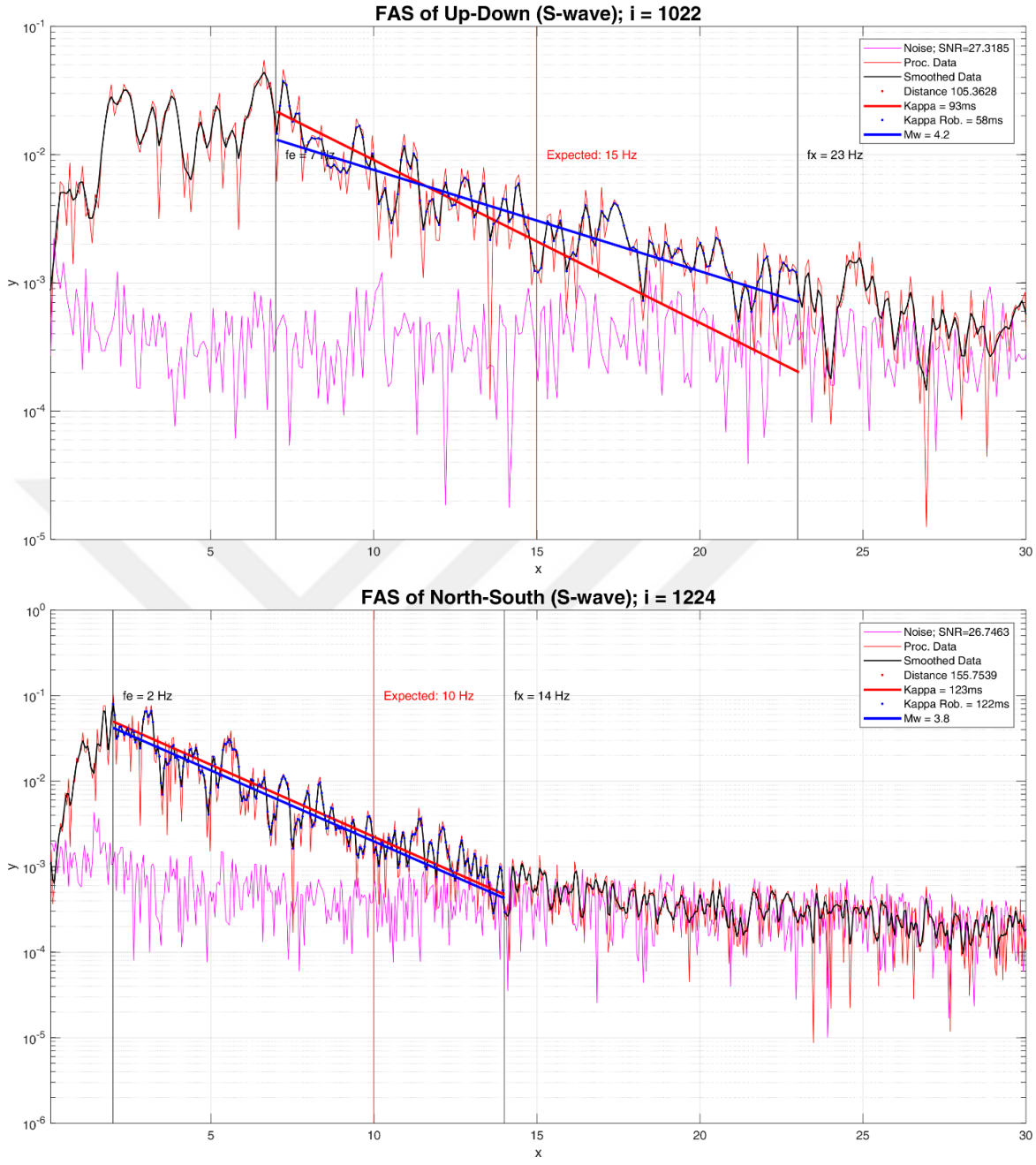

Figure 4.1. Sample κ_r measurements (continued).

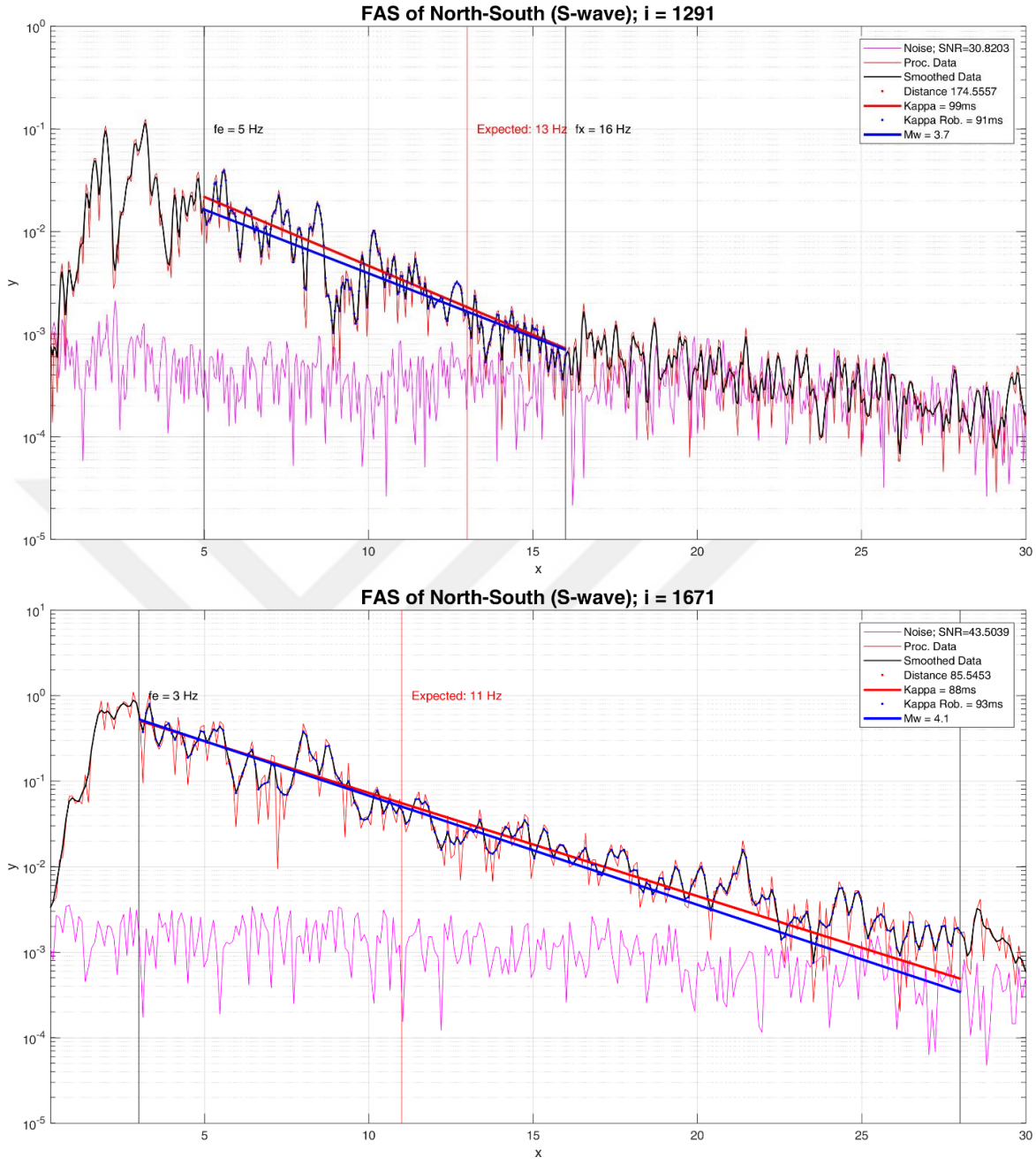

Figure 4.1. Sample κ_r measurements (continued).

4.3. Regional Kappa Model for Istanbul

Before regressing the estimated κ_r values, measurements on two horizontal components (north-south and east-west) were averaged. This only could be realized if only two of the horizontal components existed. Additionally, we also checked how different each κ_r for two horizontal components were measured. 1208 out of 1401 averaged horizontal values of north-south and east-west components had individual κ_r estimations closer than 70%, while only 16 out of 1401 averaged values had lower approximation than 50%. When the data with 70% approximation were used, the difference in κ_0 results were only around 1%. We concluded that it is acceptable to use the whole dataset consisting 1401 values and we made use of the whole dataset, regardless the amount of κ_r approximations between two horizontal components.

Initially, the linear increment of κ with distance along the whole dataset was observed. Because of the high values estimated at long distances (>260 km), a non-linear trend was observed on κ_r-distance graph. Furthermore, all immediate earthquake sources posing a seismic threat to Istanbul are within 250 km. Therefore, κ_r values having >260 km epicentral distances were excluded in the further analysis. Figure 4.2 shows the results of the κ_r-distance regression for horizontal and vertical components. The amount of the data used for regressing the horizontal component was 1401, while the amount of the data used for regressing the vertical component was 1390.

The change in κ_r regression according to the two major regions in Istanbul was also observed, namely, the European and Asian sides of the city (Figure 4.3 and Figure 4.4). The difference in horizontal κ_0 estimations (Table 4.1) is insignificant, while the slight difference matches with the surface geology - soil properties of the European side is known as weaker than the Asian side on average (Figure 4.5), as the horizontal component of κ_0 is higher than the one estimated at the Asian side. Figure 4.5 demonstrates that on the southern part of the European side V_{S30} values commonly range between 200-400 m/s, while on the Asian side -within the region of interest-, V_{S30} values range within 400-1000 m/s.

Judging by the regression lines, it is clearly seen that a slight change with respect to distance is observed (Figure 4.2, Figure 4.3 and Figure 4.4). This slight correlation with distance is also supported with low R^2 values -which are plotted in the figure legends-, while at the same time it shows that the data is scattered along the graph.

Each error bar that can be seen on the following graphs, include the mean value (μ) estimated within a specific distance range, while the edges of those bars represent ±1 standard deviation (σ). These bars mainly follow an increasing trend with distance. As can be observed, this trend doesn't follow a constant change – it is more likely to be evaluated as a wavy increase along the distance axis. The regression line is within the ±1σ almost along all error bars in these models which supports the convenience of the data for a linear regression (Figure 4.2, Figure 4.3 and Figure 4.4).

Table 4.1. Regional regression results on κ.

Description of the regression	κ_0 (ms)	m (ms/R)
All data (Hor. Comp.)	53.72	0.11
All data (Ver. Comp.)	44.49	0.09
European side of Istanbul (Hor. Comp.)	55.86	0.12
European side of Istanbul (Ver. Comp.)	44.3	0.09
Asian side of Istanbul (Hor. Comp.)	50.87	0.11
Asian side of Istanbul (Ver. Comp.)	44.65	0.08

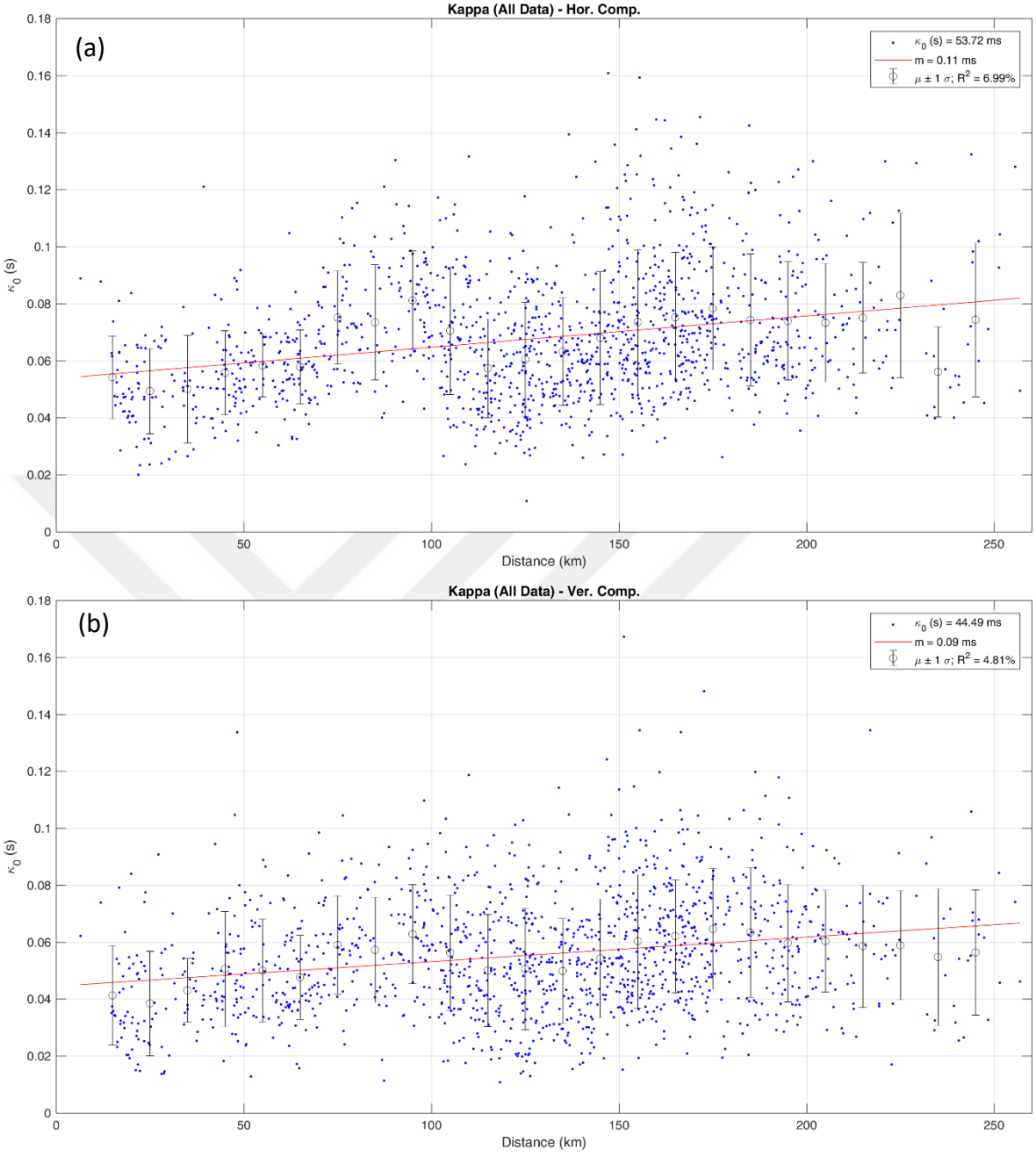

Figure 4.2. (a) Average horizontal kappa distribution with respect to distance (by using data below 260 km) (b) Average vertical kappa distribution with respect to distance (by using data below 260 km).

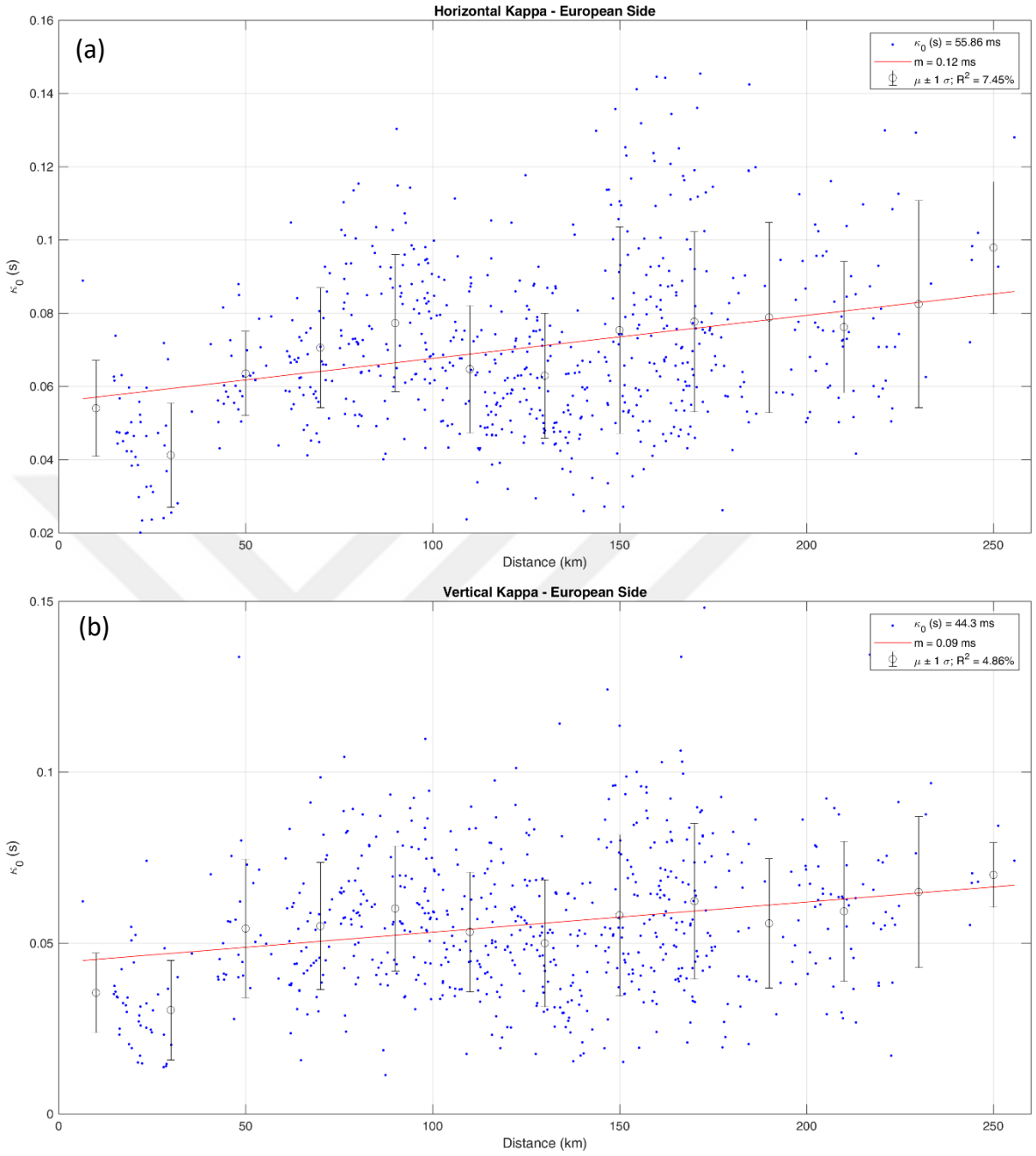

Figure 4.3. (a) Avg. horizontal kappa distribution on European side of the city with respect to distance (b) Avg. vertical kappa distribution with respect to distance on European side of the city with respect to distance.

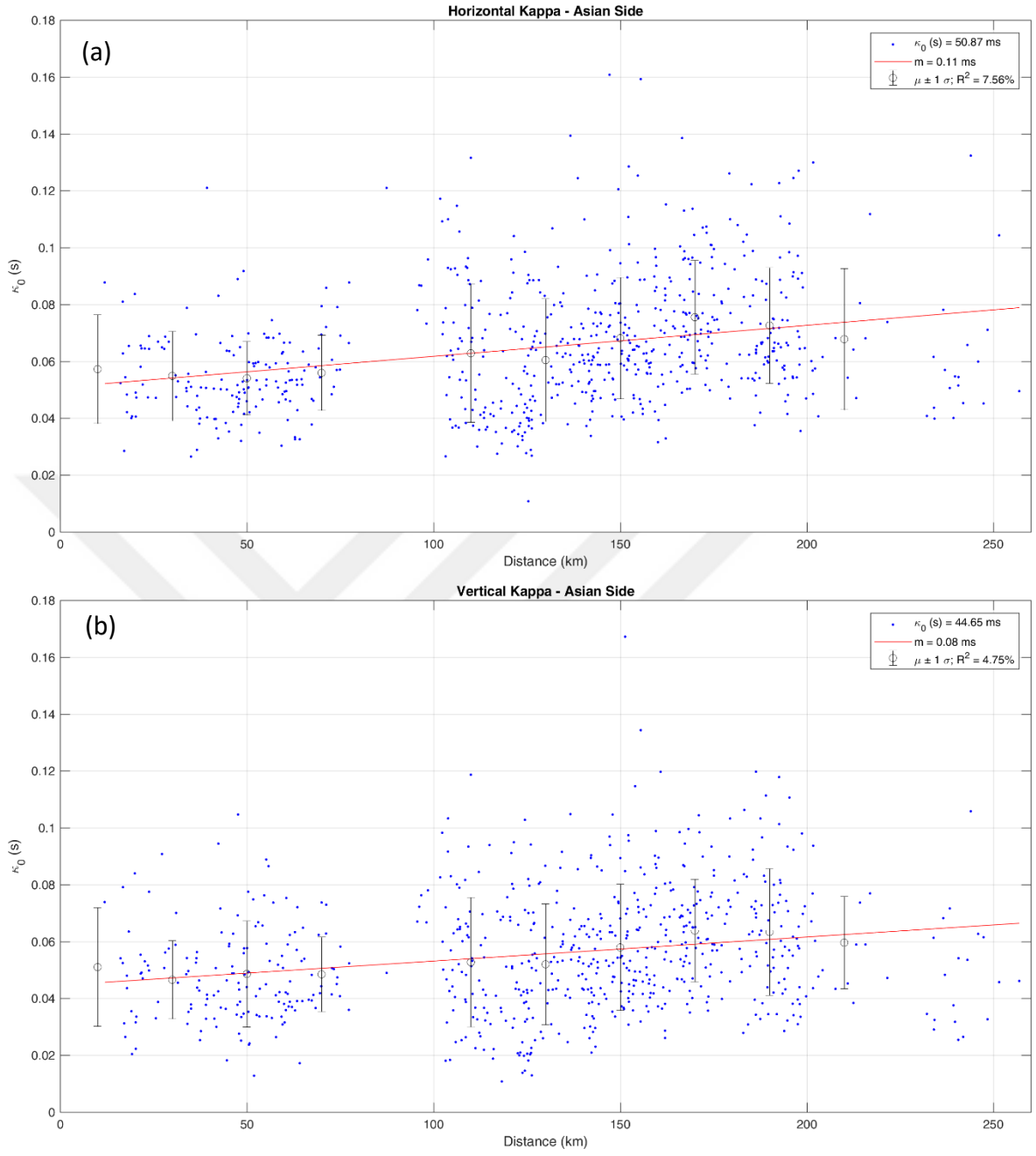

Figure 4.4. (a) Avg. horizontal kappa distribution on Asian side of the city with respect to distance (b) Avg. vertical kappa distribution with respect to distance on Asian side of the city with respect to distance.

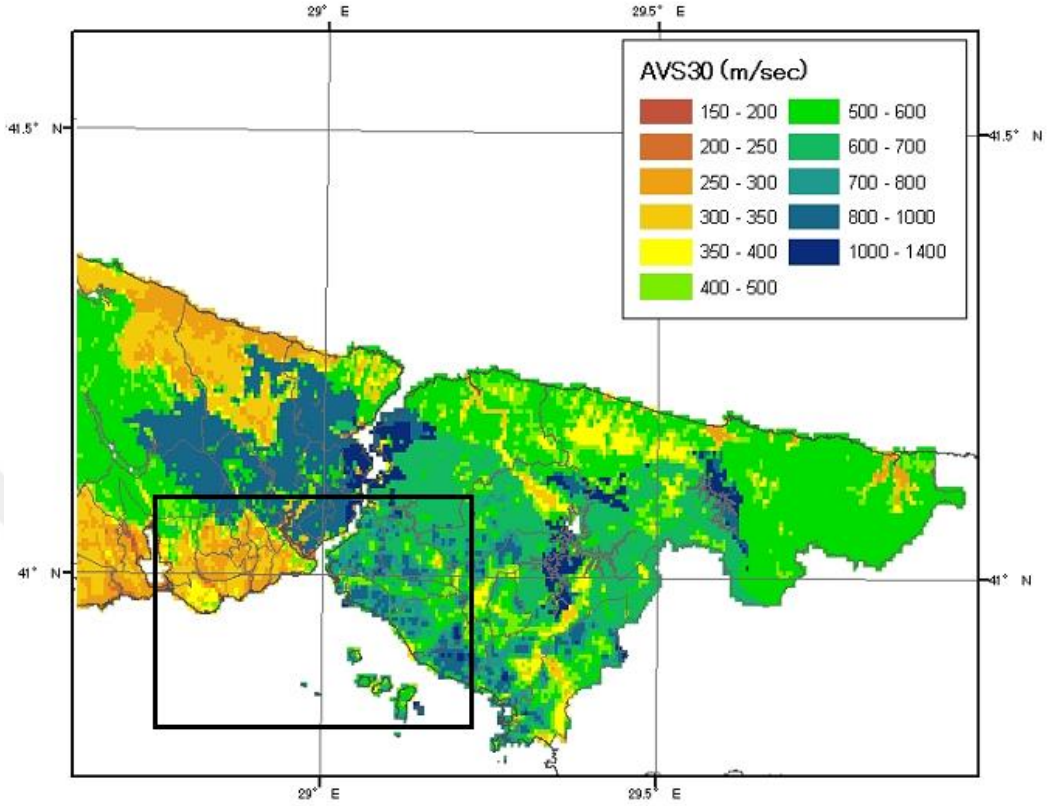

Figure 4.5. Regional V_{S30} distribution – our region of interest is denoted with the black rectangle (adopted from IBB-OYO-KOERI, 2009).

We compared our results with the ones previously reported in the literature in Table 4.2. Tanırcan and Dikmen (2018), considers stations only on the European side. Their κ_0 estimations reach up to 54 ms (Table 4.2). Askan et al. (2014) focuses on the northwestern Turkey, while they only have a single station in Istanbul. Despite the fact that their region of interest is larger than ours, their average horizontal κ_0 estimation is 50 ms, which is close to our estimations. Akinci et al. (2006) estimate κ_0 for Marmara region as 55 ms, for the horizontal component and D type site class. Durukal and Çatalyürekli (2004) focus on estimating source parameters from 1999 Kocaeli and Düzce earthquake sequences. They estimate κ_0 for horizontal component as 41.3 and 56, for the C and D type of soils respectively. Our results apparently support these previous estimations for Istanbul and for the nearby region.

Table 4.2. Previous relevant studies prepared in regions of northwestern Turkey.

Studies	Number of earthquakes used	Number of records used	Number of Stations	Distance from source	Magnitude range	K_0 (ms)	m (ms/km)
This Study	50	4192	115	<260 km	4.0<=ML<=5.7	Hor/All Data: **54** Ver/All Data: **45**	Hor/All Data: **0.11** Ver/All Data: **0.08**
Tanırcan and Dikmen, 2018	52	131	5 (5)	<200 km	3.0<= ML <=4.8	Hor/Surface: **26-54**	-
Aşkan et al., 2014	142	174x3	15 (1)	<200 km	3.0<=Mw <=6.0	Hor/SiteC: **37.7** Hor/SiteD: **45.5** Avg. Hor: **50**	Hor/SiteC: **0.132** Hor/SiteD: **0.132**
Akıncı et al., 2006	462	2400x3	53	5-250 km	2.5<=Mw <=7.2	Avg. hor/SiteD: **55**	-
Durukal and Çatalyürekli, 2004	84	494x2	58 (9)	5.77-39.89 km	1.93<=ML <=6.04	Hor/SiteC: **41.3** Hor/SiteD: **56**	Hor/SiteC: **0.1** Hor/SiteD: **0.3**
Durukal, 2002	2	59x3	27; 32	<200 km	7.1; 7.4	Avg. hor: **63 and 65;** Avg hor/SiteD: **72 and 73;** Avg hor/SiteB-C: **48 and 54;**	-

[1]Number of stations located in Istanbul, out of total

4.4. Dependence of Kappa on Signal-to-Noise Ratio

Since the amount of data was high, we also had the opportunity to check the effect of noise by categorizing κ_r-distance regressions according to signal-to-noise ratio values. Initially, we filtered the κ_r values that were estimated through records having SNR's over 25 and then over 40 for both horizontal and vertical components (Figure 4.6 and Figure 4.7). The results show that κ_0 values decreased as the SNR values increased, while also the slopes decreased at the same time. The amount of data was less as the higher SNR's were considered in such regressions. For the regression in which κ_r values that were estimated through records having SNR's over 25 were estimated, the whole amount of used data decreased to 882 for horizontal and 596 for the vertical component; while for the case of SNR's over 40, the amount of data decreased to 180 for horizontal and to 86 for vertical component.

Judging by the error bar trends, again the wavy trend is seen in the graph prepared with κ_r values having SNR values higher than 25 (Figure 4.6), while it is difficult to make a similar observation in the graph with κ_r values with SNR>40 (Figure 4.7).

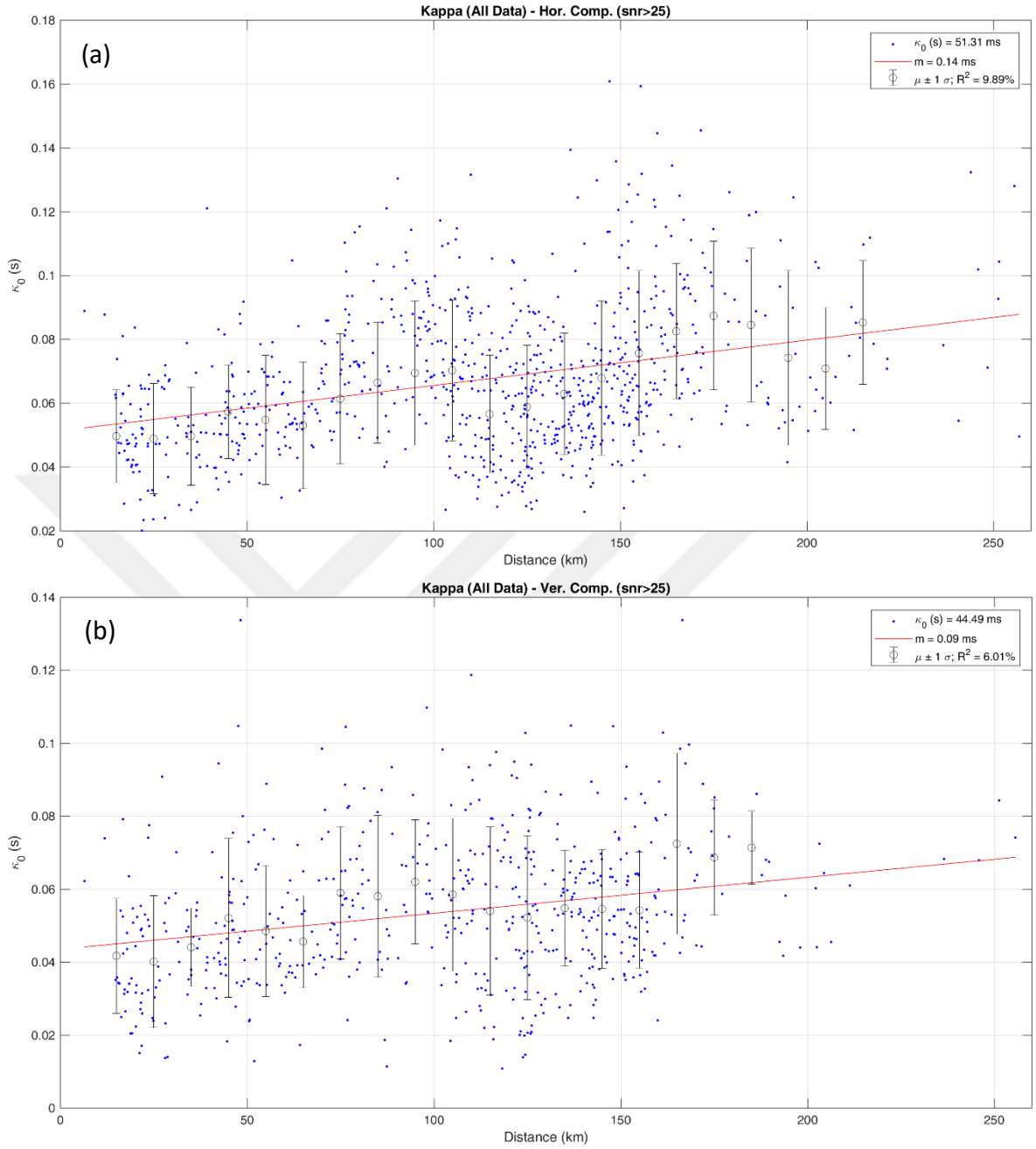

Figure 4.6. (a) Horizontal κ_r-distance regression with data estimated through records having SNR>25; (b) Vertical κ_r-distance regression with data estimated through records having SNR>25.

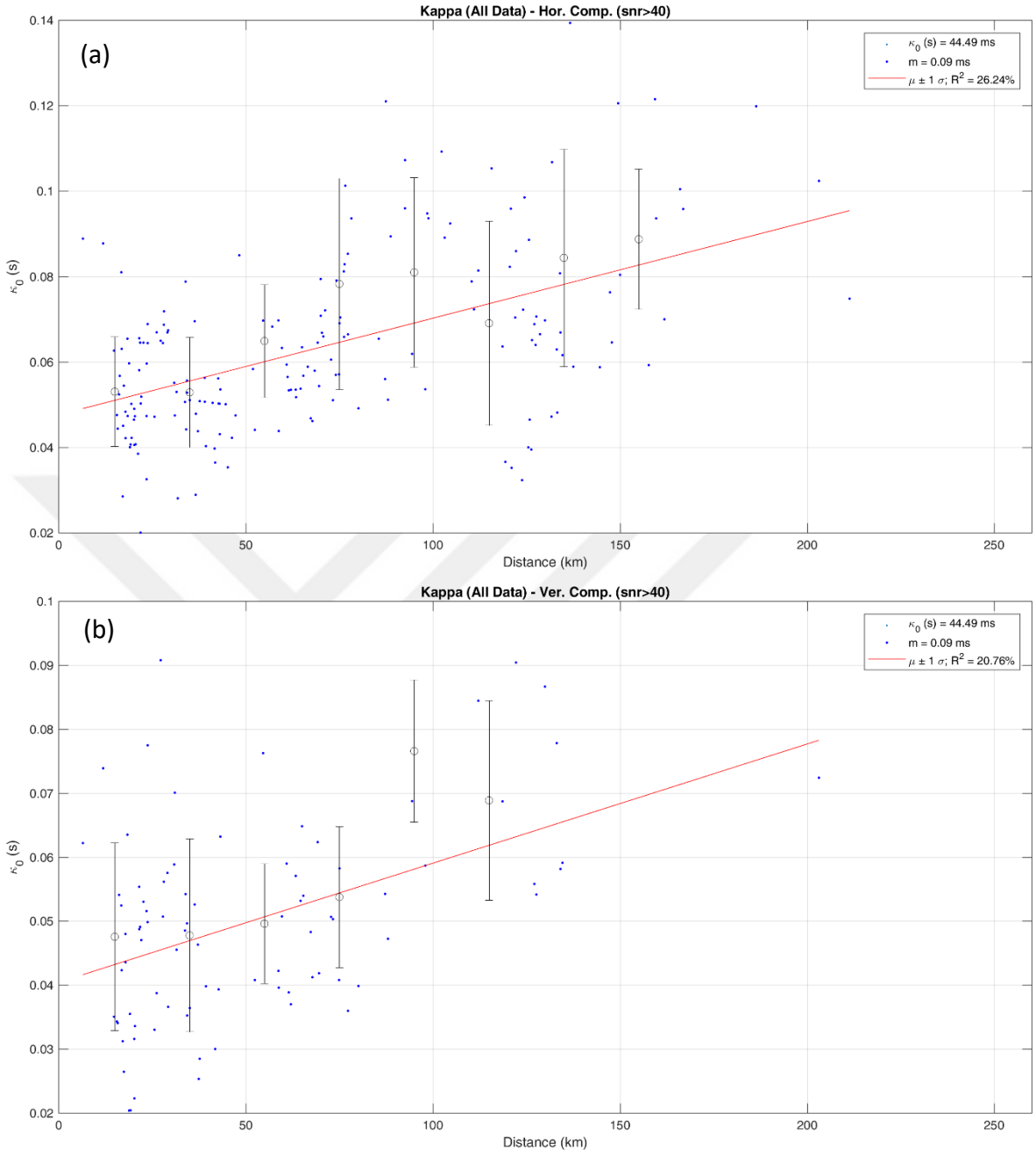

Figure 4.7. (a) Horizontal κ_r-distance regression with data estimated through records having SNR>40; (b) Vertical κ_r-distance regression with data estimated through records having SNR>40.

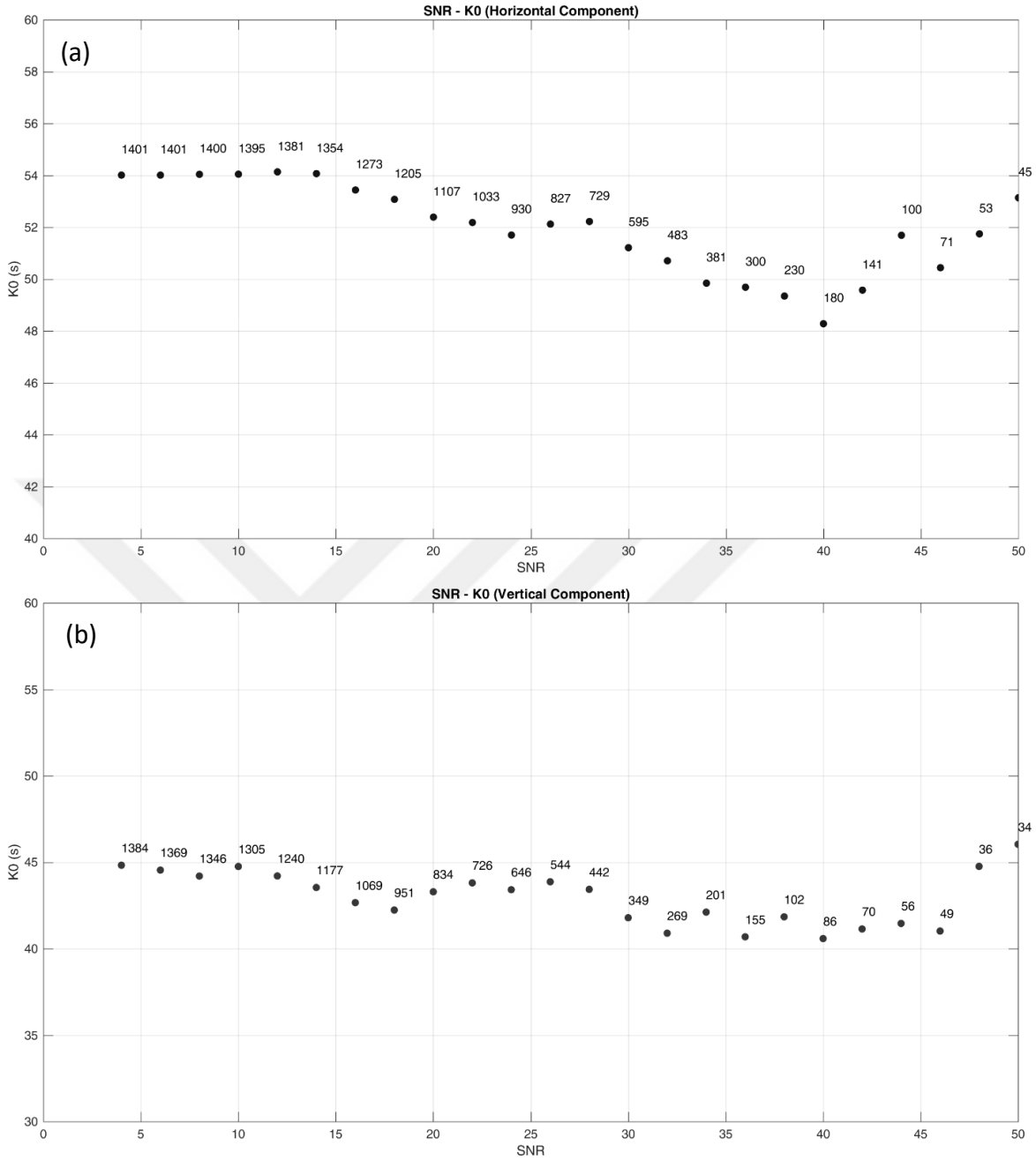

Figure 4.8. (a) κ_0-SNR graph for horizontal component, amount of data used in each regression plotted on the graph; (b) κ_0-SNR graph for vertical component, amount of data used in each regression plotted on the graph.

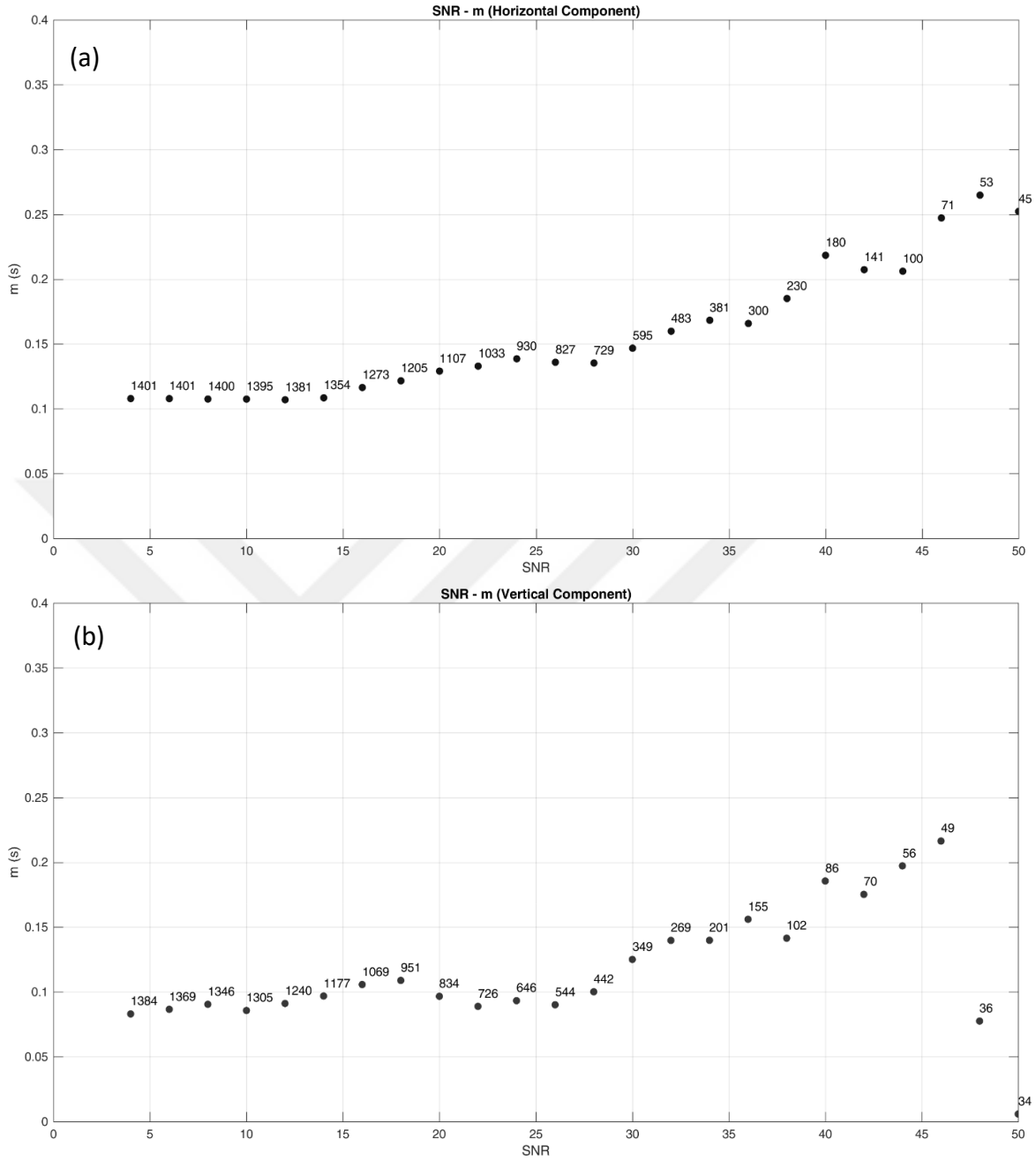

Figure 4.9. (a) m-SNR graph for horizontal component, amount of data used in each regression plotted on the graph; (b) m-SNR graph for vertical component, amount of data used in each regression plotted on the graph.

Throughout the graphs in Figure 4.8 and Figure 4.9 we see a consistent change in our estimations as the SNR values increase. First of all, it is possible that the decrease of the number of the data used (plotted next to the data points on both graphs) as the SNR values increase could have manipulated our results - especially if the data is lacking in higher distances. Since the fluctuation in our κ_0-distance graph -that we observed in previous sections- is considered, m values might easily differ when a remarkable amount of data lacks at distant regions. Meanwhile, these observations and thoughts are not enough for a reliable conclusion, yet, sufficient amount of data is still needed at higher SNRs, in which the regression analyses will be prepared upon homogenously oriented data along the distance axis. Besides that, also the other possible contributions from source, path and site effects should be studied better.

These correlations prepared so far, -regardless how reliable they are-, lead us to new discussions - whether there is or not any significant contribution of noise in κ_r measurements. So far, these preliminary results on discussing the possible manipulations of noise is encouraging for taking this part of the study a step further.

4.5. Dependence of Kappa on Earthquake Azimuth

In this section we discuss the differences regarding the azimuthal changes. This approach will show us the path effects of certain traveling paths - from sources to the stations used in this study, taking the stations as reference points. Figure 4.10 shows us azimuthal distribution of the records with respect to epicentral distance. For further regression analysis, we decided to categorize records between the ranges of 359-40 degrees, 102-150 degrees, 150-195 degrees, 195-240 and 240-288 degrees.

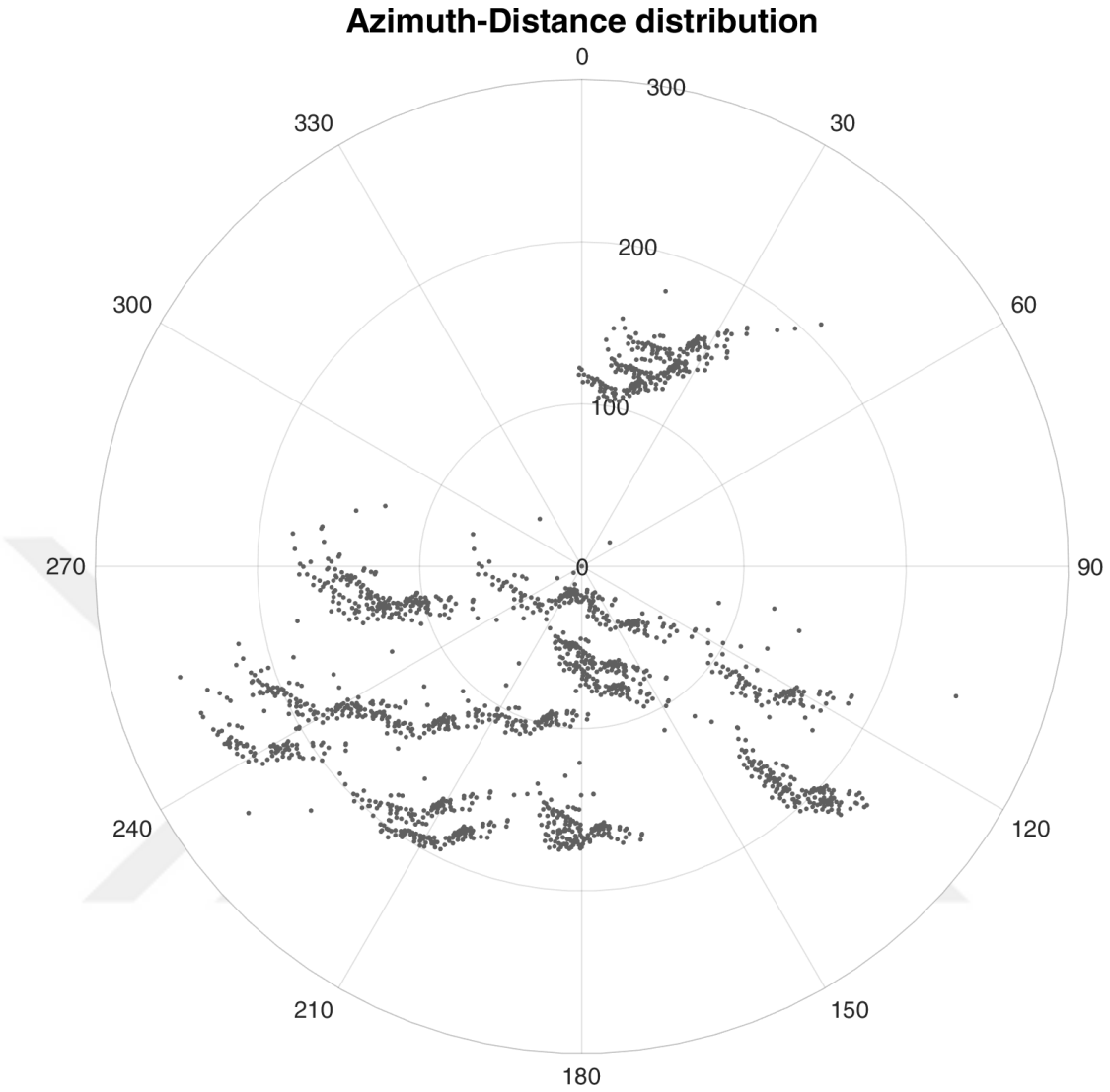

Figure 4.10. Azimuth-distance distribution of the records.

As can be seen in Figure 4.10, between 359-40 degrees, the distance of the data from the stations is almost only between 100-190 km, which makes any kind of regression unreliable for this case. Similarly, in Figure 4.11, the same data can be seen distributed over distance. Therefore, we find the remaining estimations more meaningful, even though still some data is yet to be added. They can be seen represented in Figure 4.12, Figure 4.13, Figure 4.14 and Figure 4.15. The results of the regression analyses can also be found in Table 4.3, including the amount of the data used.

Table 4.3. κ_0 and m estimations regarding azimuths.

Azimuthal Range	κ_0 (ms)	m (ms/R)	Amount of used data
102-150 degrees (Hor. Comp.)	61.72	0.12	233
102-150 degrees (Ver. Comp.)	52.03	0.09	230
150-195 degrees (Hor. Comp.)	50.27	0.2	337
150-195 degrees (Ver. Comp.)	41.66	0.16	344
195-240 degrees (Hor. Comp.)	53.9	0.12	317
195-240 degrees (Ver. Comp.)	44.07	0.09	307
240-288 degrees (Hor. Comp.)	62.73	0.03	282
240-288 degrees (Ver. Comp.)	53.22	0.02	278

As can be seen in Table 4.3, results significantly variate according the changing azimuths. Among these four azimuthal categorizations, the horizontal and vertical components of κ_0 differ up to 25%. It is also possible that different azimuthal combinations will result in higher differences.

Similar to the previous section, some data is lacking at certain distances, which makes it highly possible that the reason of the difference between the κ_0 estimations is that. But at the same time, categorizing our dataset according to azimuths means categorizing them according to slightly different upper-crustal properties – where some differences in m values can be expected. Once the data needed at certain distances will be added, the meaningfulness of these differences will also be compared with the Q model prepared within this study.

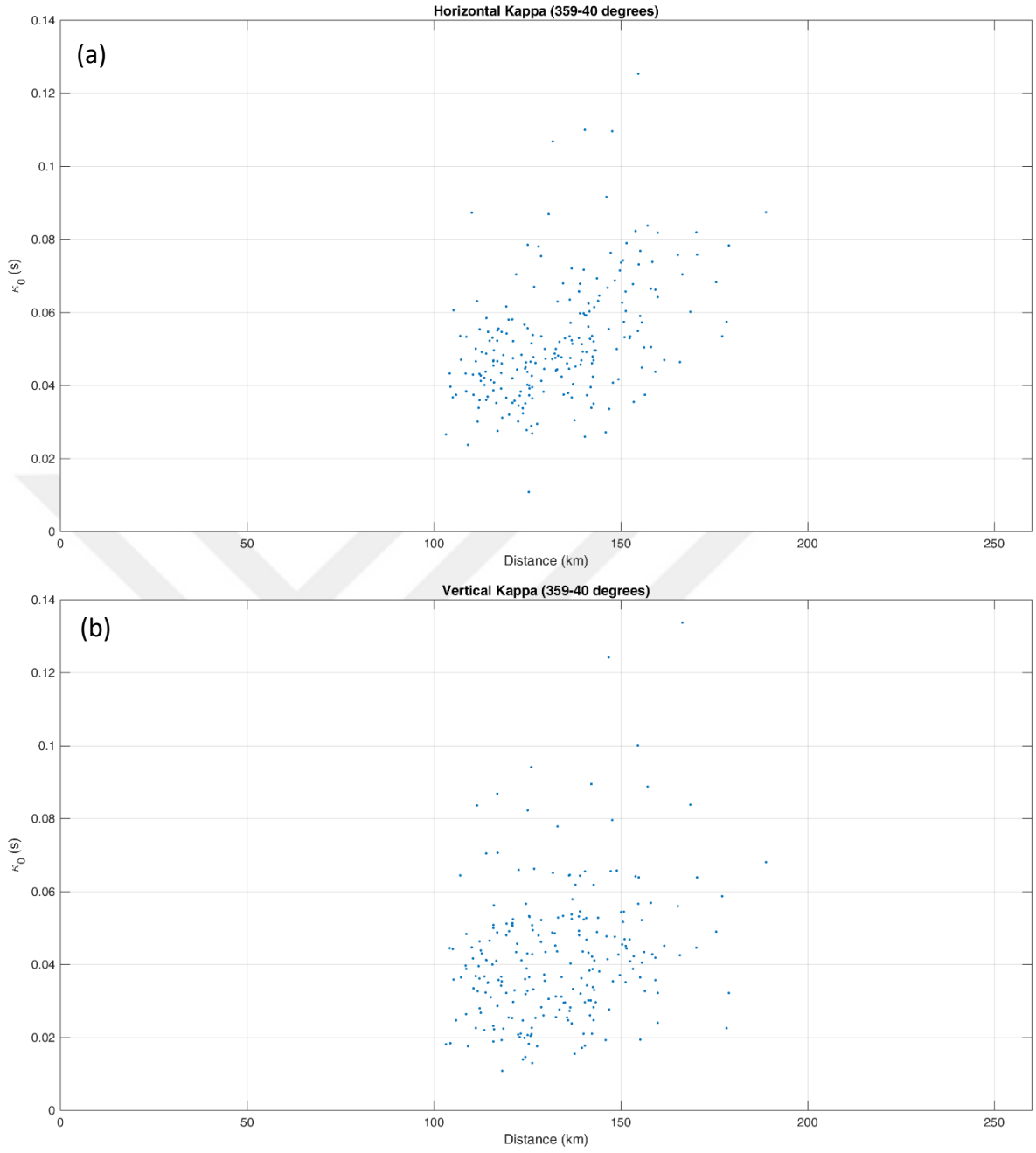

Figure 4.11. (a) Horizontal κ_r-distance regression with data between 359-40 degrees (b) Vertical κ_r-distance regression with data between 359-40 degrees.

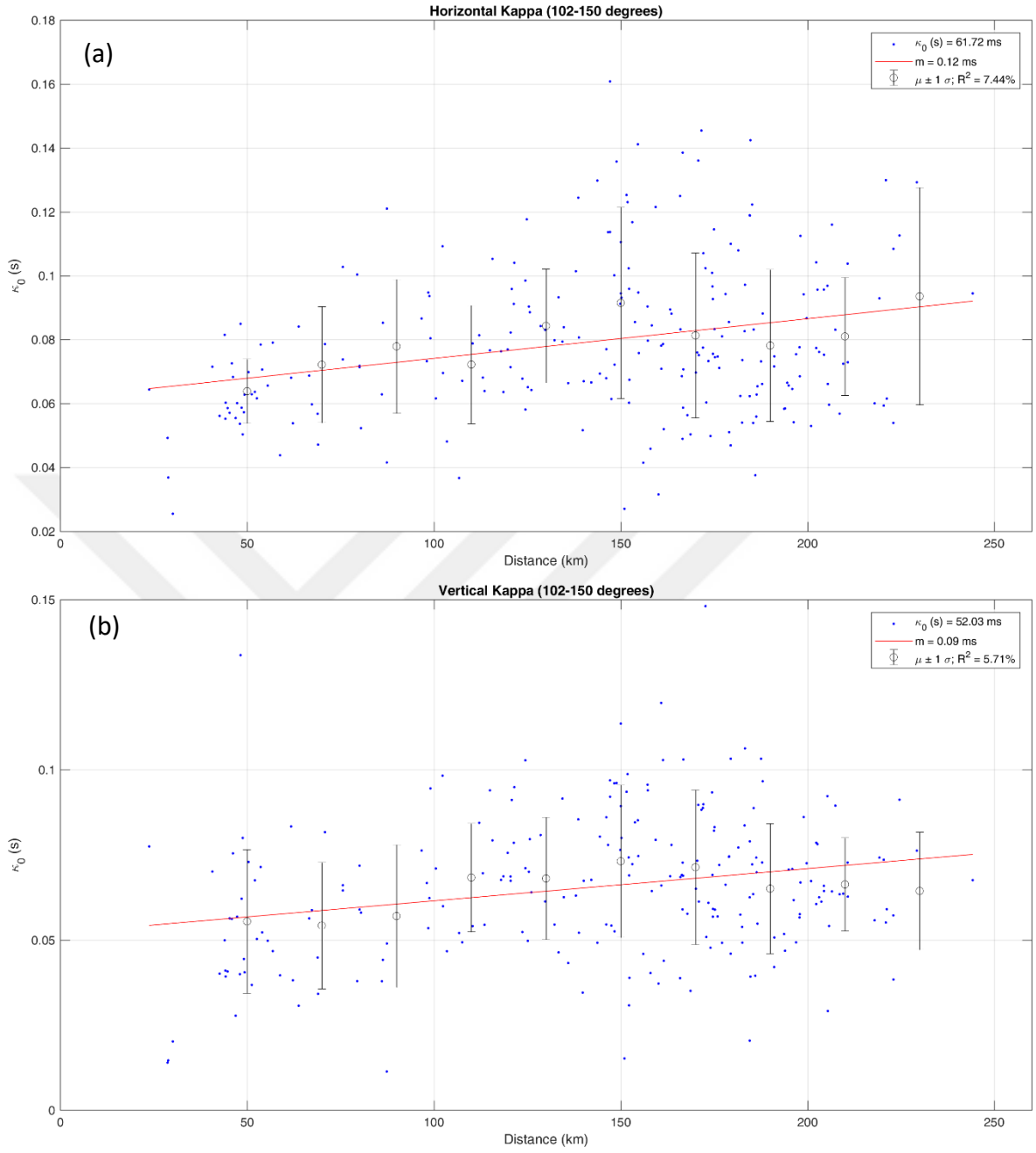

Figure 4.12. (a) Horizontal κ_r-distance regression with data between 102-150 degrees (b) Vertical κ_r-distance regression with data between 102-150 degrees.

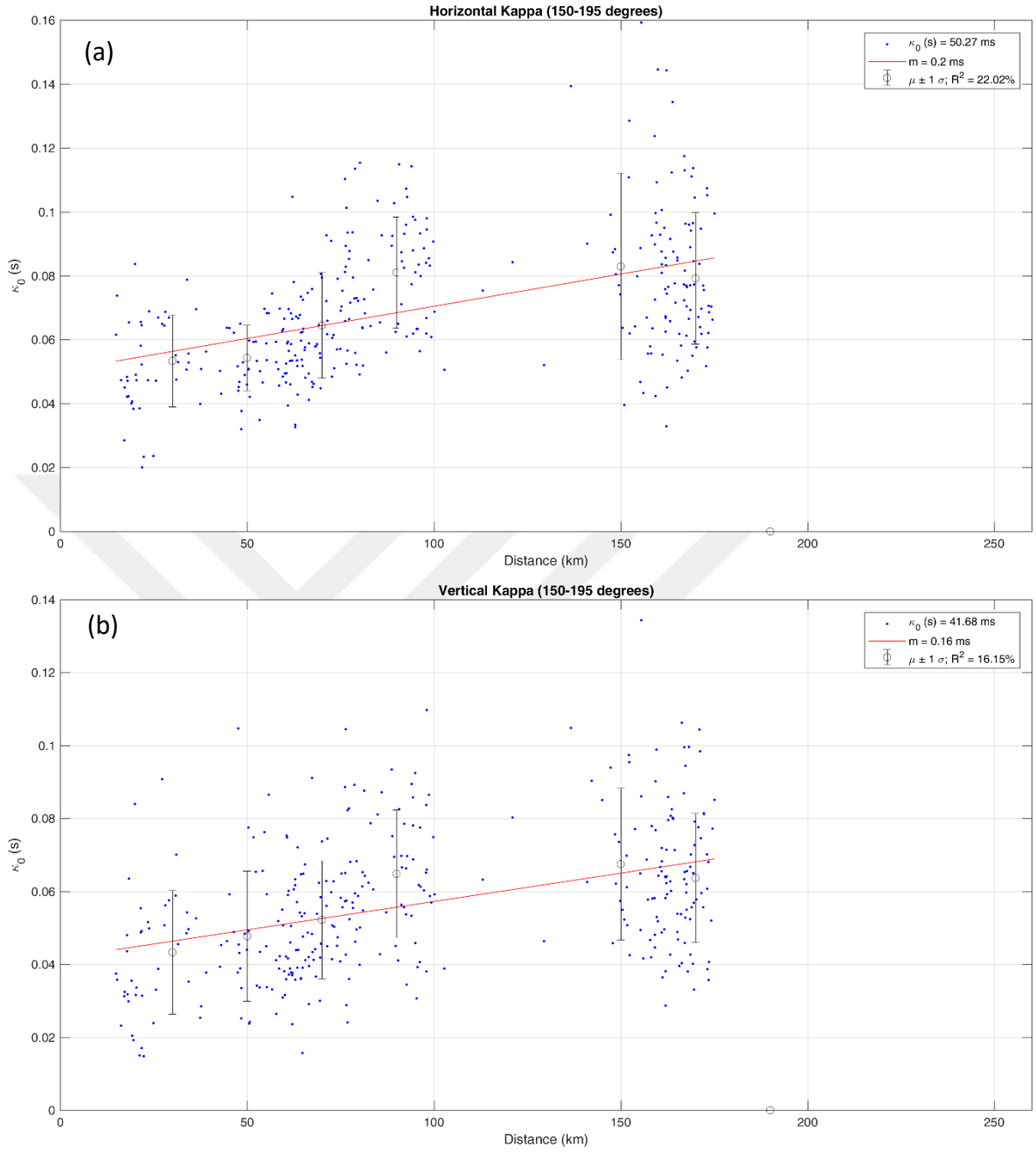

Figure 4.13. (a) Horizontal κr-distance regression with data between 150-195 degrees (b) Vertical κr-distance regression with data between 150-195 degrees.

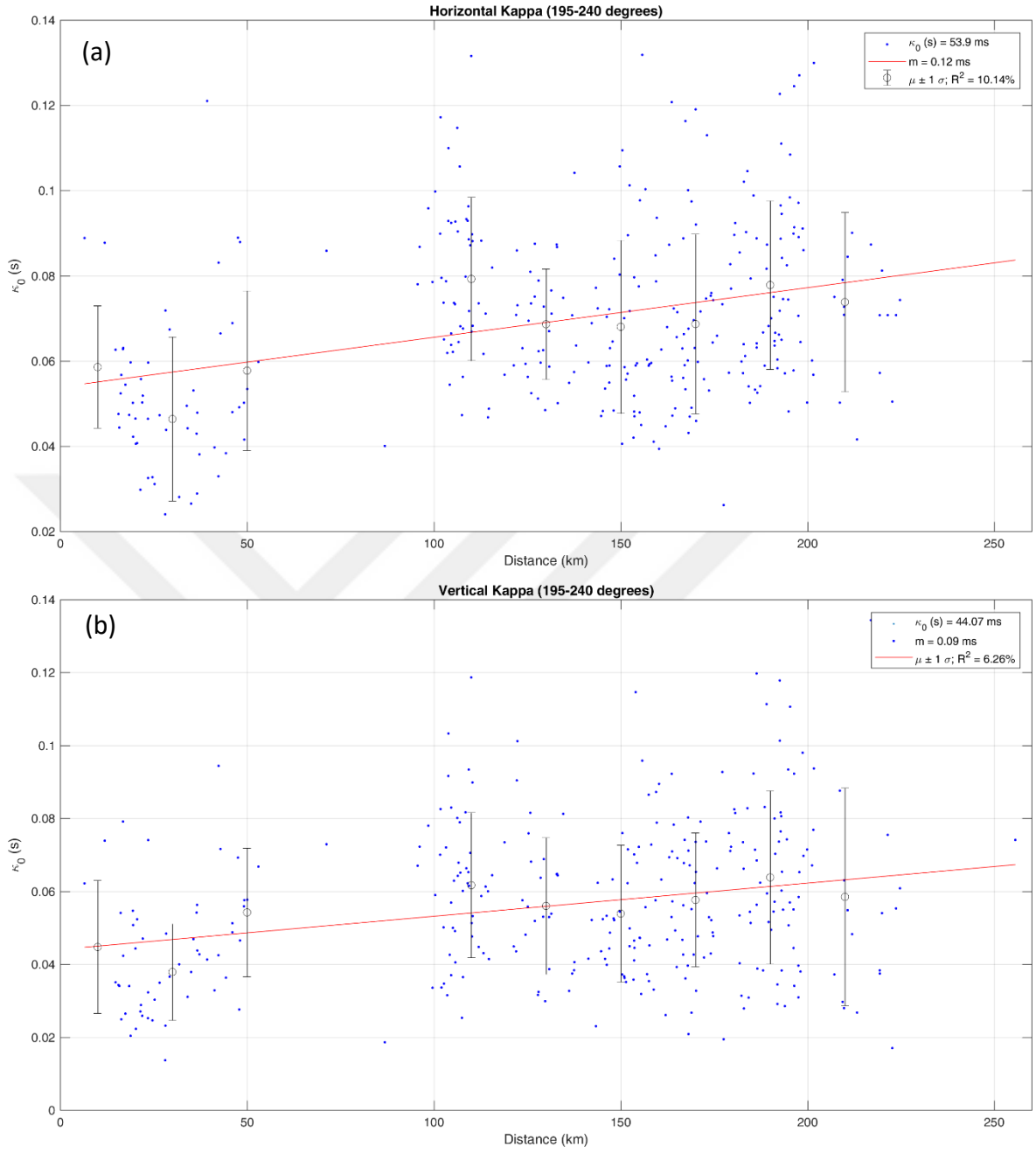

Figure 4.14. (a) Horizontal κr-distance regression with data between 195-240 degrees (b) Vertical κr-distance regression with data between 195-240 degrees.

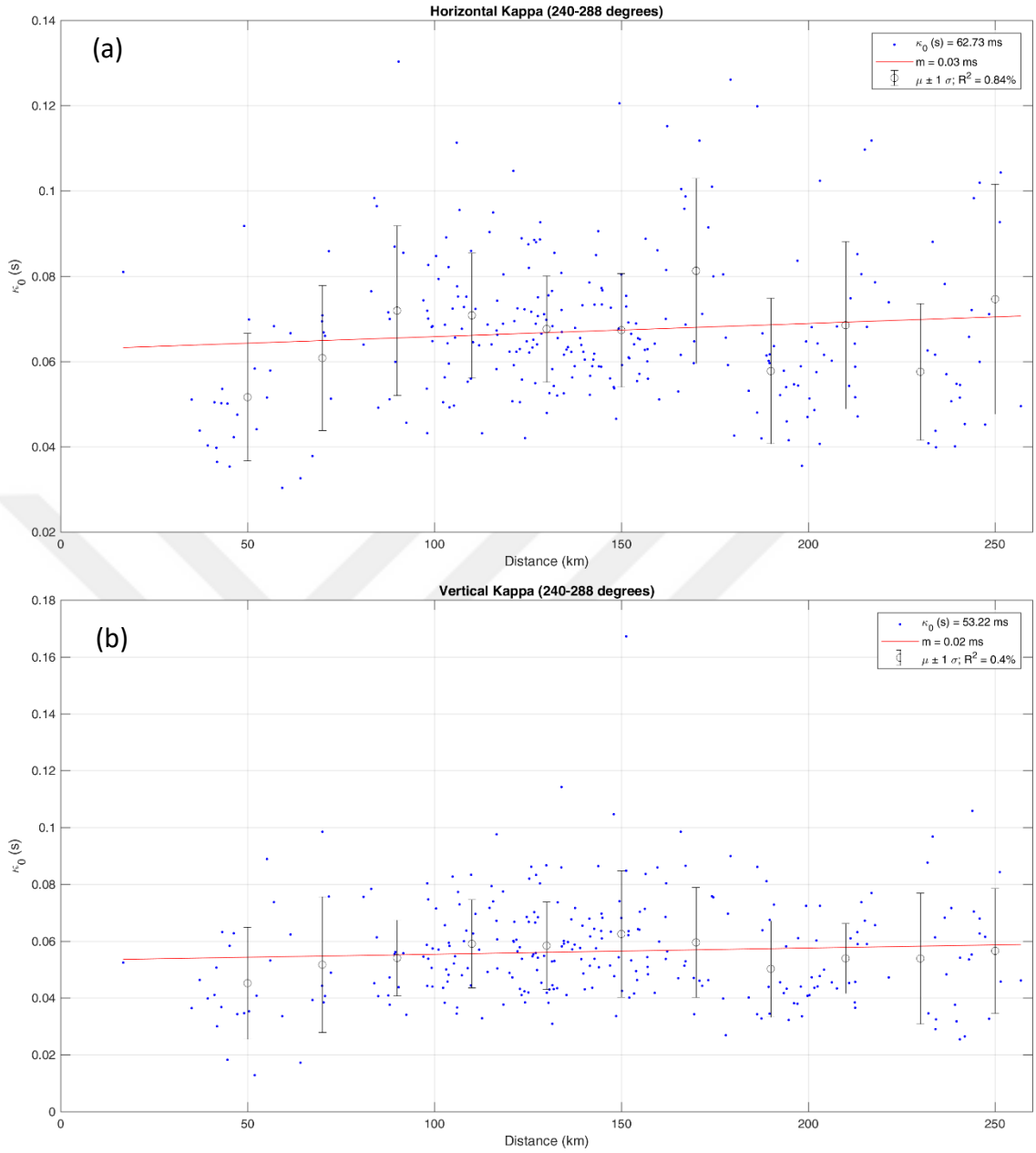

Figure 4.15. (a) Horizontal κr-distance regression with data between 240-288 degrees (b) Vertical κr-distance regression with data between 240-288 degrees.

4.6. Station-Specific Kappa

Due to the sufficient amount of data, we also had the opportunity to check the κ_0s of every station individually. As most of the stations had enough data for individual regressions, those who had less than six were neglected. Also, the regression models with a slope less than 0 or above 0.25 ms/R were also not considered.

Table 4.4. Station-specific horizontal κ_0 and m estimations.

Station	κ_0 (ms)	m	Num. of data
AKUKO	57.6	0.07	15
ATAIO	79.2	0.03	16
AVCLI	64.19	0.16	16
BABAO	69.33	0.03	16
BAHBL	47.64	0.16	15
BAHHI	51.67	0.12	14
BATAL	44.68	0.08	17
BAVIO	51.46	0.09	15
BBAIO	50.32	0.02	16
BOTS	46.64	0.12	28
BRGA	54.47	0.15	25
BUYA	61.61	0.08	25
CENLI	31.79	0.15	15
DATIO	52.44	0.06	20
EHAIO	53.61	0.04	20
ESNBB	36.81	0.18	16
FBZMD	56.7	0.07	16
FEBLI	47.92	0.08	17
GOPPL	35.33	0.04	12
GUMLI	66.09	0.13	16
GUNGR	56.78	0.15	13
HAVAV	68.27	0.1	14
HTMLI	49.17	0.2	17
HVHR	77.8	0.12	18
HYBA	59.47	0.1	21
HYSIO	40.41	0.13	18
IHHIO	37.7	0.17	18
IOAIO	27.08	0.24	16
ISMIO	43.12	0.18	16
ITFER	64.5	0.01	7
KAPIO	41.18	0.15	12
KARSO	55.88	0.01	20
KASDL	46.49	0.1	17
KCKBK	71.63	0.03	17

Station	κ_0 (ms)	m	Num. of data
KDHBI	49.65	0.11	18
KHAIO	52.02	0	17
KRTTP	61.46	0.12	15
KSSIO	71.21	0.03	18
KUCEM	55.98	0.05	14
LAFA	62.65	0.08	11
MARIO	42.1	0.21	21
MBNIO	41.34	0.21	19
MECLI	48.52	0.05	14
MMZIO	51.67	0.06	15
MODAI	71.18	0.02	16
MYMIO	40.17	0.09	16
OKCIO	43.07	0.12	15
PGZOL	47.06	0.07	16
PTMLI	39.78	0.02	16
PVBIO	43.84	0.08	15
SINB	59.21	0.14	17
SMKIO	46.7	0.07	19
SSPOO	70.13	0.08	9
TTEML	51.65	0.12	17
TUZAL	60.99	0.18	13
UACPI	60.01	0.03	17
UDAIO	48.72	0.11	16
UMSBI	53.06	0.05	19
UMSKI	43.58	0.1	19
USCUL	55.28	0.04	16
USKPL	43.78	0.06	12
YHSTI	55.79	0.16	14
YILIO	45.51	0.1	16
YKBL	83.19	0	14
YLVH	105.26	0.11	18
ZOTML	43.41	0.19	13
ZYTAL	63.83	0.04	18
ZYTDK	53.57	0.16	18

After applying these filters, 68 stations were left. The lowest observed κ_0 is 27.08 ms, while the highest one is 105.29 ms. κ_0s tend to variate usually between 40-70 in most of the cases in this set of analyses. Table 4.4 show the results of this regression analyses for the horizontal component, as the relevant graphs can be seen in Figure 4.16 as well.

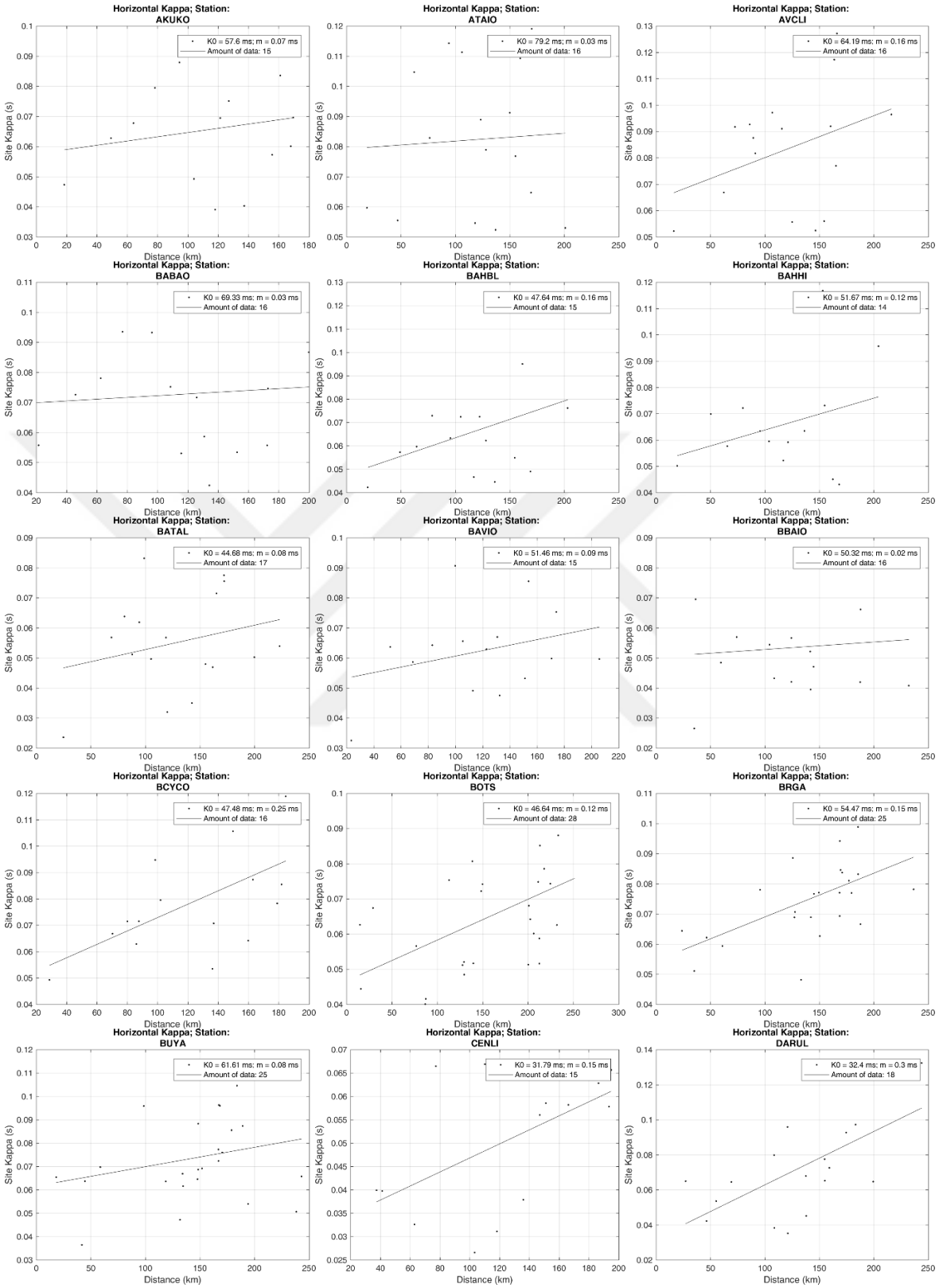

Figure 4.16. Horizontal κ_r-distance regression in each station fulfilling the criteria.

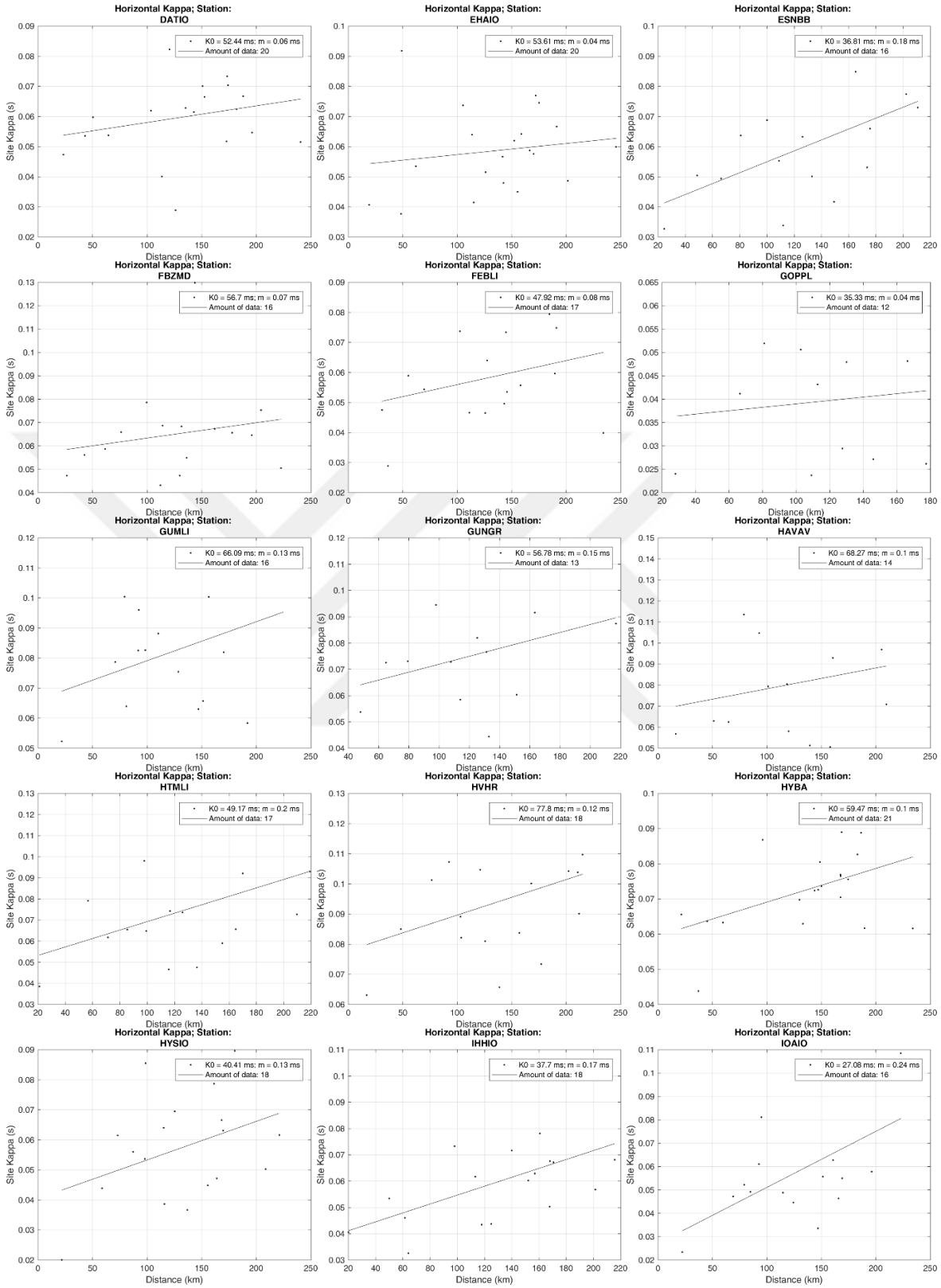

Figure 4.16. Horizontal κ_r-distance regression in each station fulfilling the criteria (continued).

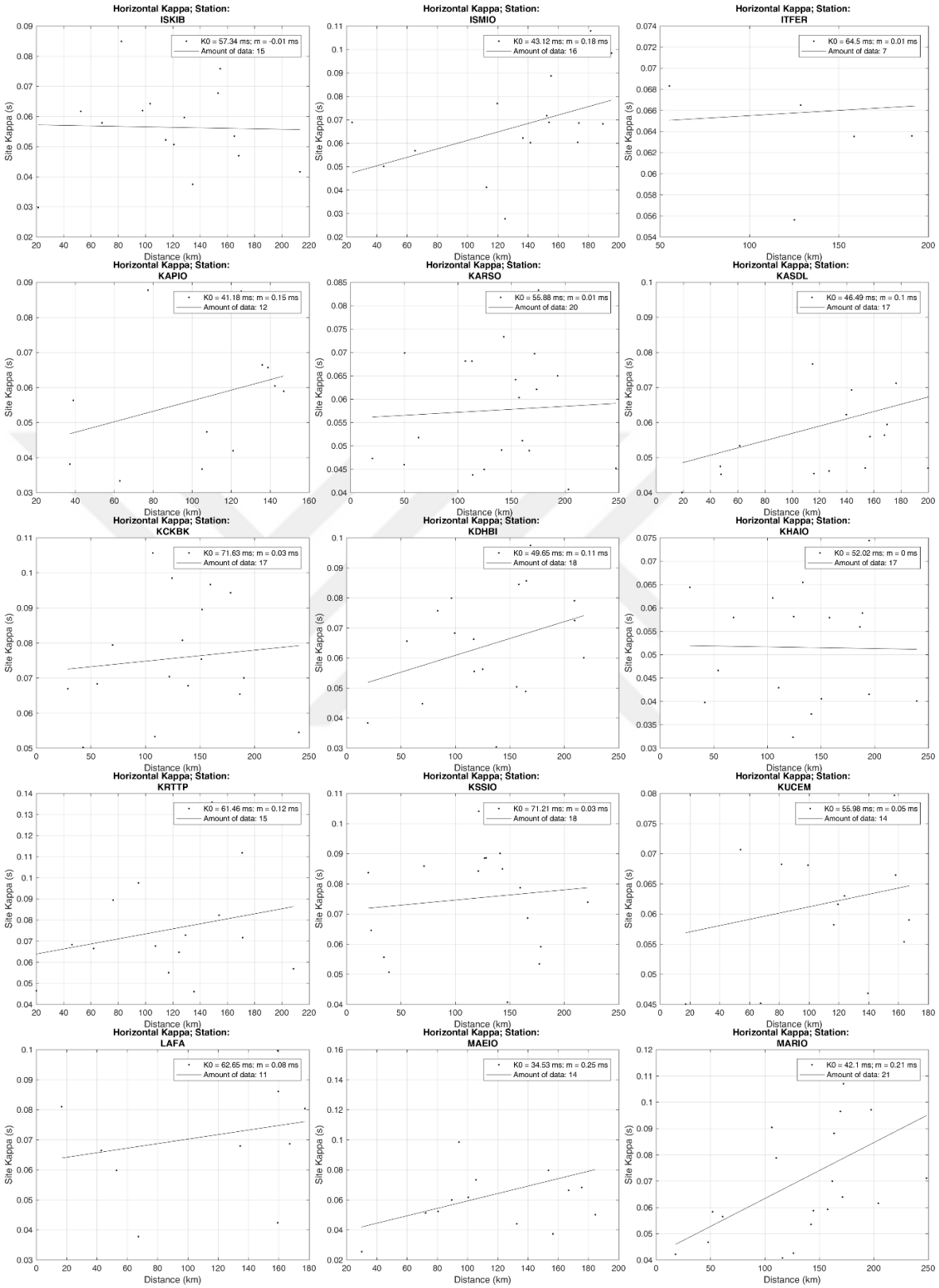

Figure 4.16. Horizontal κ_r-distance regression in each station fulfilling the criteria (continued).

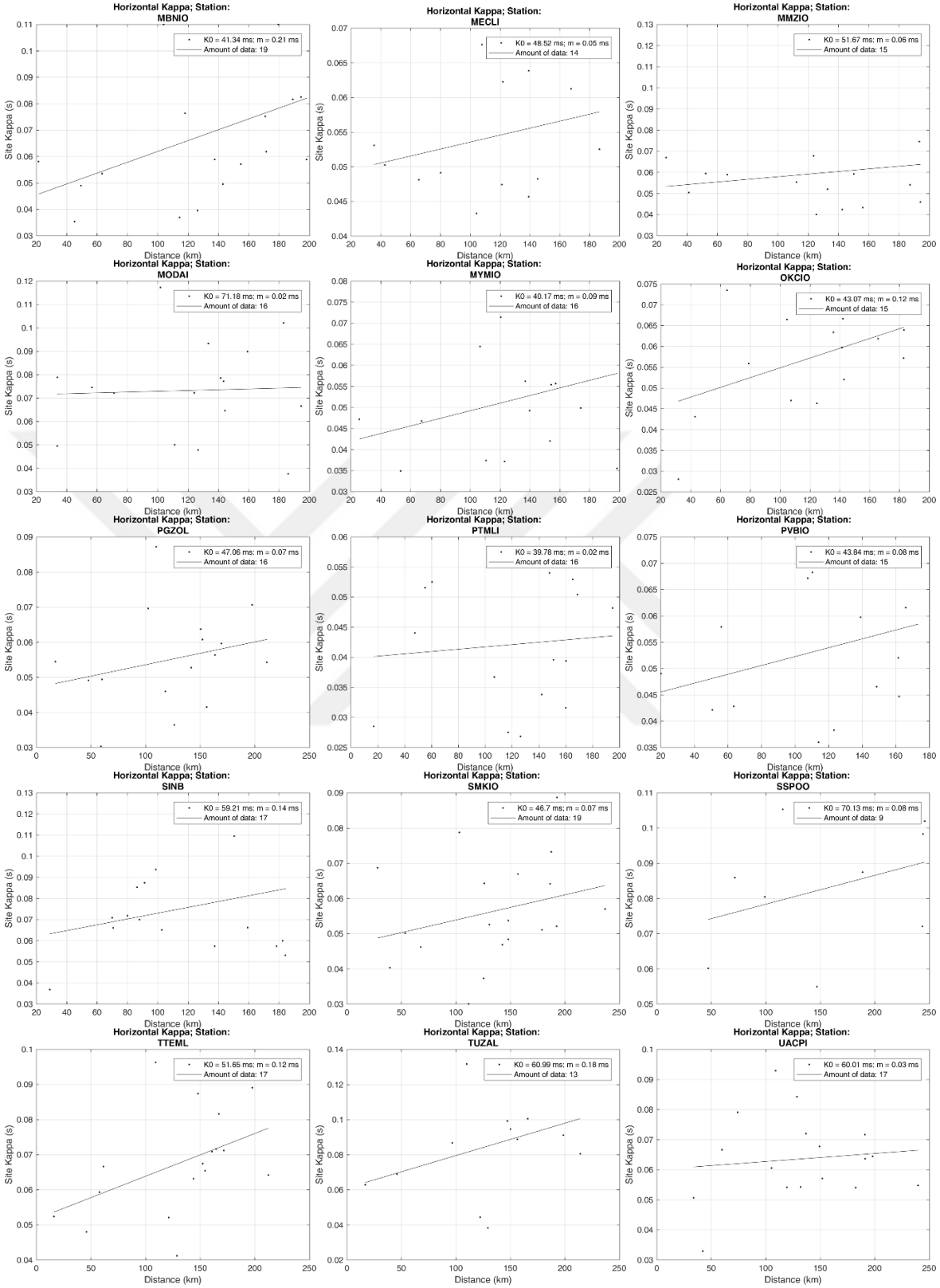

Figure 4.16. Horizontal κ_r-distance regression in each station fulfilling the criteria (continued).

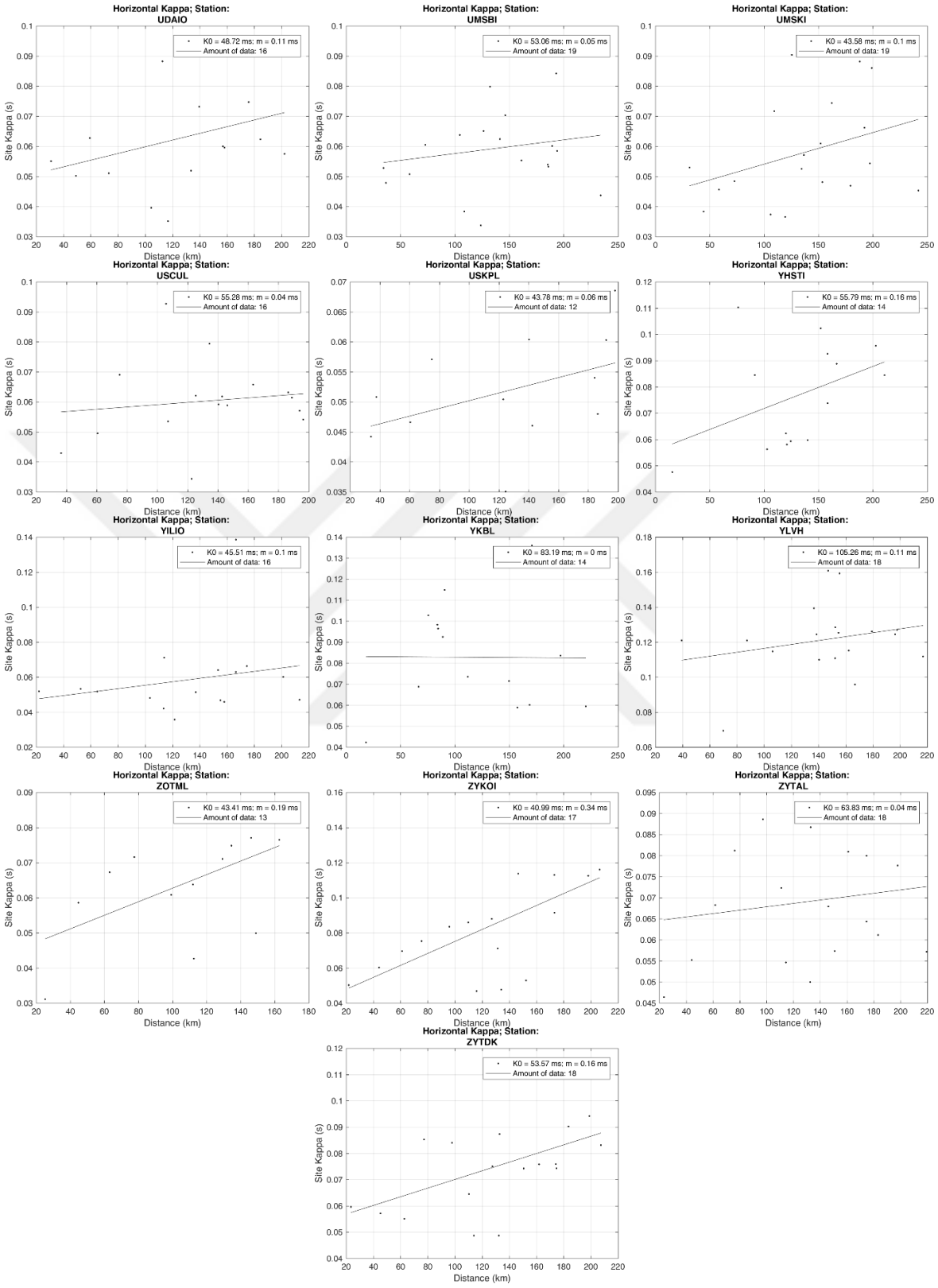

Figure 4.16. Horizontal κ_r-distance regression in each station fulfilling the criteria (continued).

The same process was applied to vertical component κ_r values also. 66 stations were left in which the regression process was applied after filtering the data with the same criteria: we used stations which had more than five data and fitting slopes with more than zero but less than 0.25 ms/R. 12.14 ms and 69.04 ms are the minimum and the maximum vertical values observed in the stations. Similarly, the overall results can be found in Table 4.5 and in Figure 4.17.

Table 4.5. Station-specific vertical κ_0 and m estimations.

Station	κ_0 (ms)	m (ms/R)	Num. of data
AKKIO	60.64	0.15	11
AKUKO	47.18	0.03	14
ATAIO	19.08	0.18	16
AVCLI	48.87	0.13	16
AVIIO	53.36	0.12	13
BABAO	49.87	0.09	16
BAHBL	55.09	0.1	14
BATAL	36.04	0.16	17
BAVIO	52.25	0.05	16
BBAIO	40.25	0.01	16
BCYCO	28.28	0.13	16
BOTS	18.27	0.19	28
BRGA	50.82	0.1	25
BUYA	47.38	0.12	25
CENLI	12.14	0.24	15
DARUL	56.16	0.12	18
EHAIO	24.14	0.16	20
ESNBB	45.91	0.08	16
FBZMD	40.44	0.03	16
GOPPL	26.41	0.04	12
GUMLI	44.67	0.09	17
HAVAV	26.47	0.18	13
HHBLI	47.51	0.15	19
HTMLI	29.84	0.2	17
HVHR	69.04	0.01	18
HYBA	49.26	0.13	21
HYSIO	41.77	0.18	17
IHHIO	23.6	0.24	19
IOAIO	20.92	0.2	15
ISKIF	43.91	0.08	18
ISMIO	35.19	0.11	16
KARSO	33.64	0.14	20
KASDL	37.39	0.12	18

Station	κ_0 (ms)	m (ms/R)	Num. of data
KCKBK	67.45	0	17
KDHBI	44.34	0.02	18
KHAIO	45.91	0.05	17
KRTTP	57.25	0.04	16
KSSIO	61.35	0.04	18
KUCEM	35.79	0.22	15
LAFA	53.5	0.13	12
MAEIO	45.14	0.07	15
MARIO	33.59	0.13	22
MBNIO	48.96	0.11	18
MECLI	38.82	0.08	14
MMZIO	38.25	0.06	15
MYMIO	38.85	0.05	16
NSEIO	17.55	0.18	14
OKCIO	33.19	0.16	16
PGZOL	29.61	0.09	16
PVBIO	37.98	0.08	15
SISIO	46.96	0.05	6
SMKIO	39.53	0.12	19
TUZAL	62.58	0.11	12
UACPI	50.53	0	18
UDAIO	50.34	0.03	17
UMSBI	42.9	0.04	19
UMSKI	36.03	0.12	19
USKPL	30.85	0.03	12
YGBIO	58.09	0.04	18
YHSTI	42.02	0.09	14
YILIO	29.75	0.16	16
YKBL	47.51	0.12	14
YLVH	41.44	0.23	19
ZYKOI	43.86	0.1	17
ZYTAL	42.22	0.07	16
ZYTDK	63.29	0.03	17

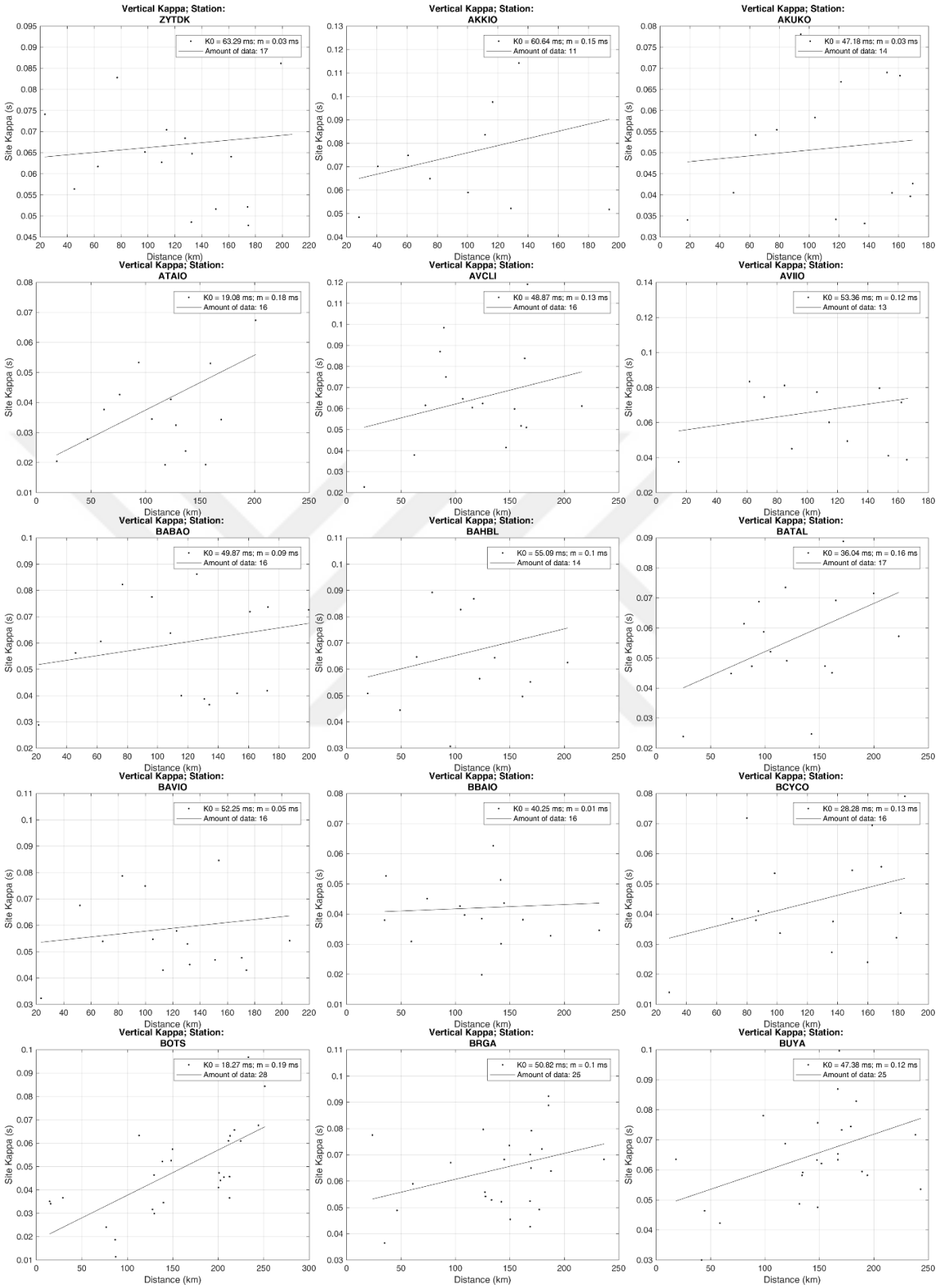

Figure 4.17. Vertical κ_r-distance regression in each station fulfilling the criteria.

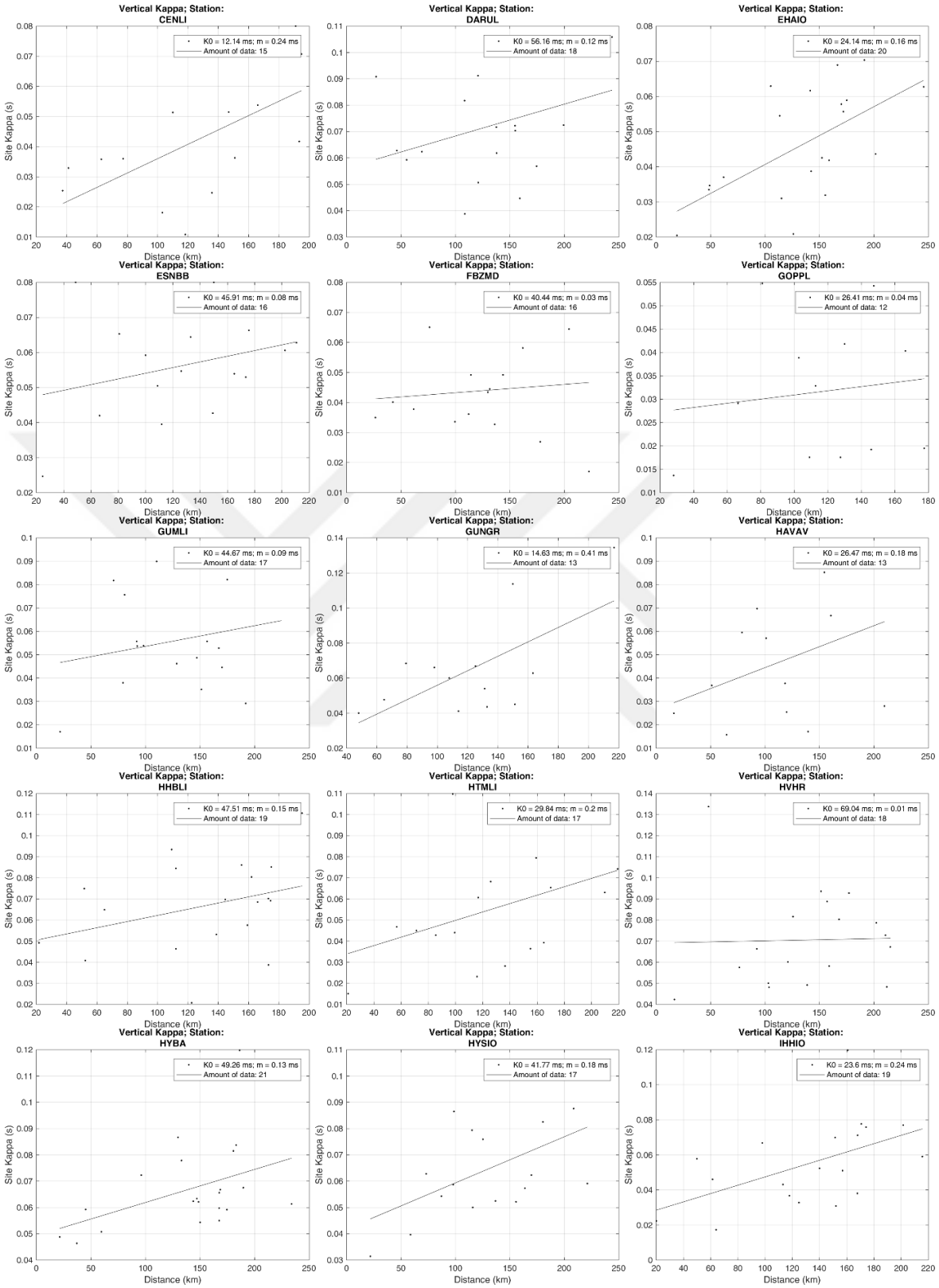

Figure 4.17. Vertical κ_r-distance regression in each station fulfilling the criteria (continued).

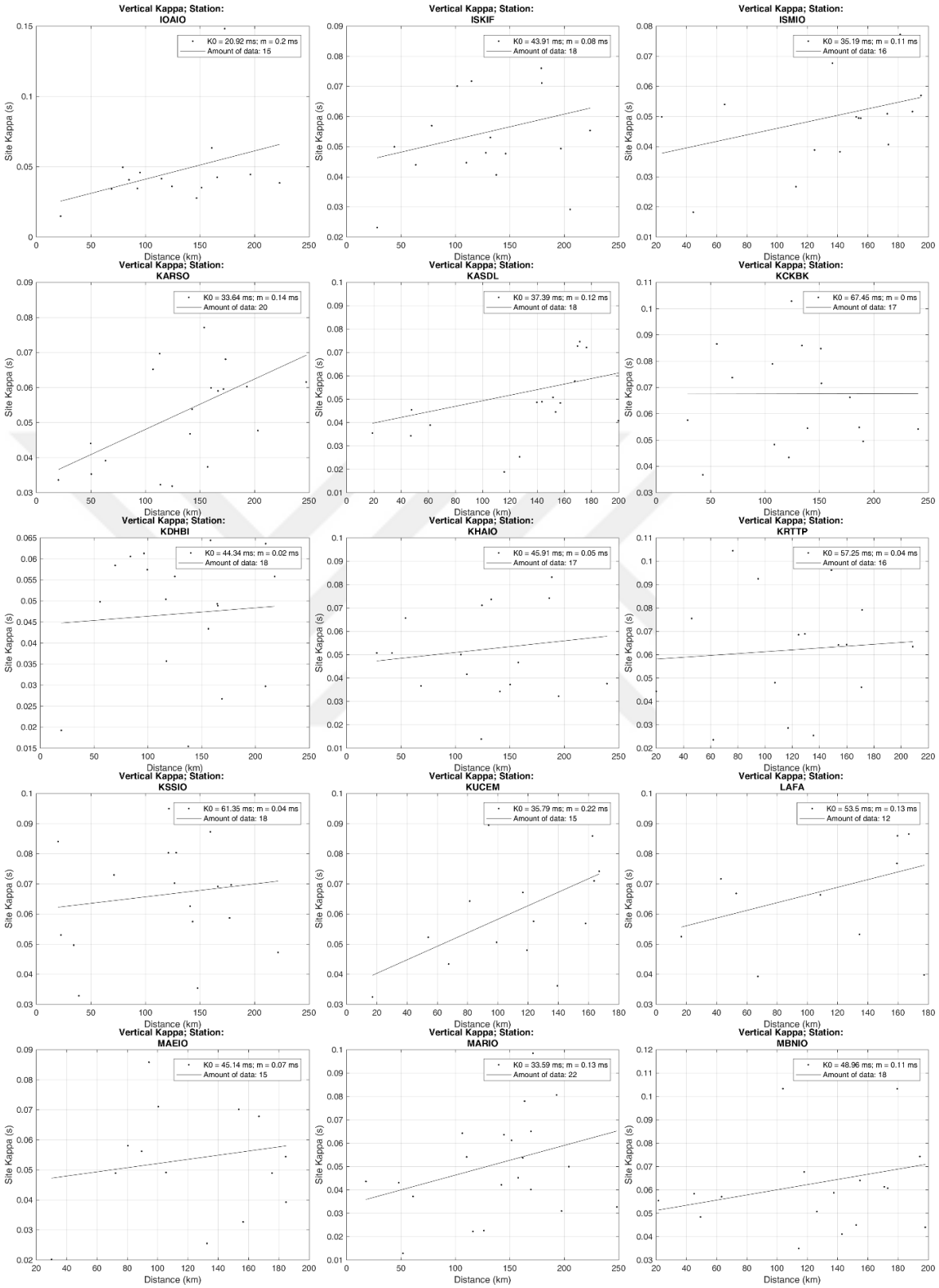

Figure 4.17. Vertical κ_r-distance regression in each station fulfilling the criteria (continued).

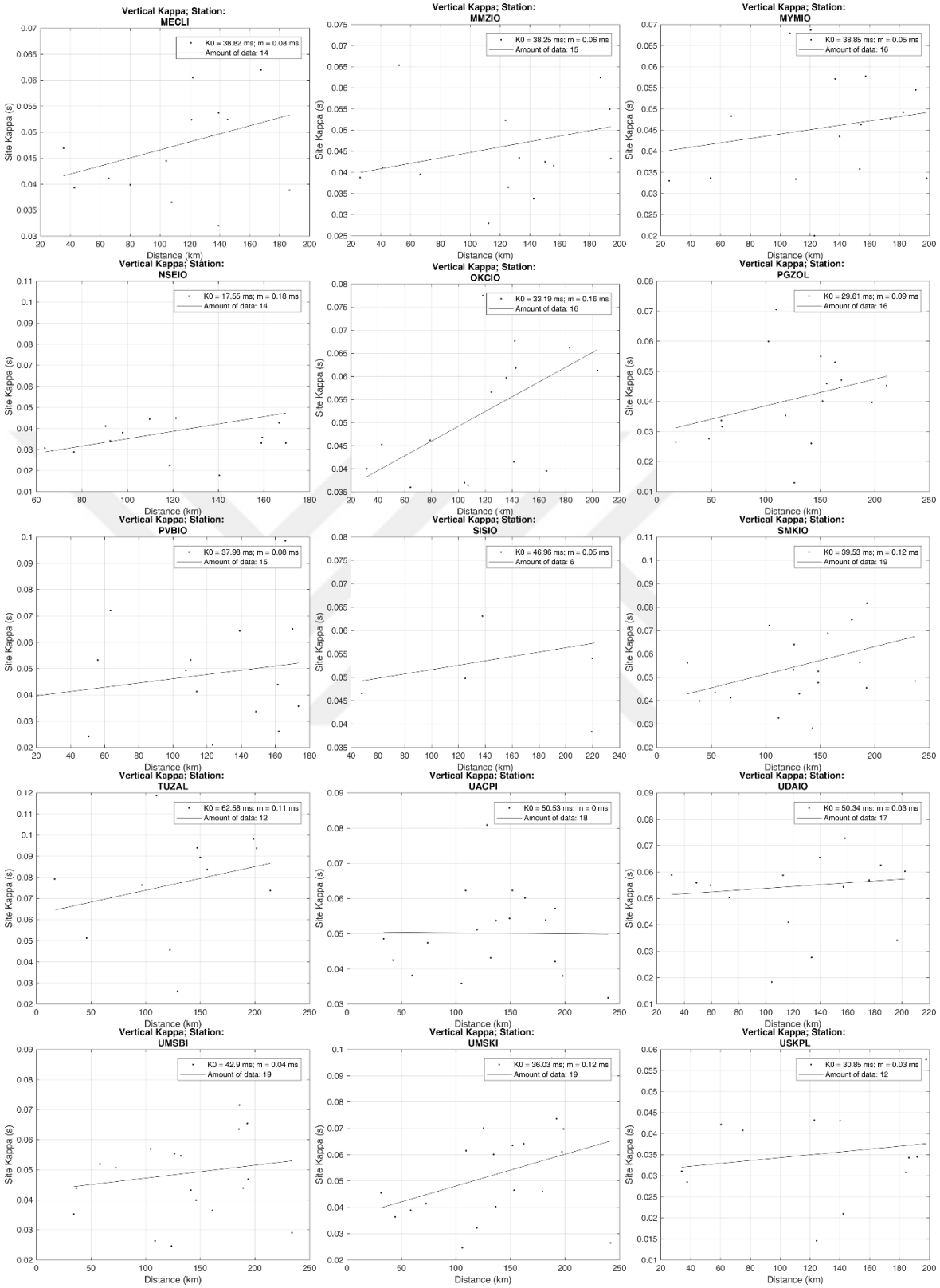

Figure 4.17. Vertical κ_r-distance regression in each station fulfilling the criteria (continued).

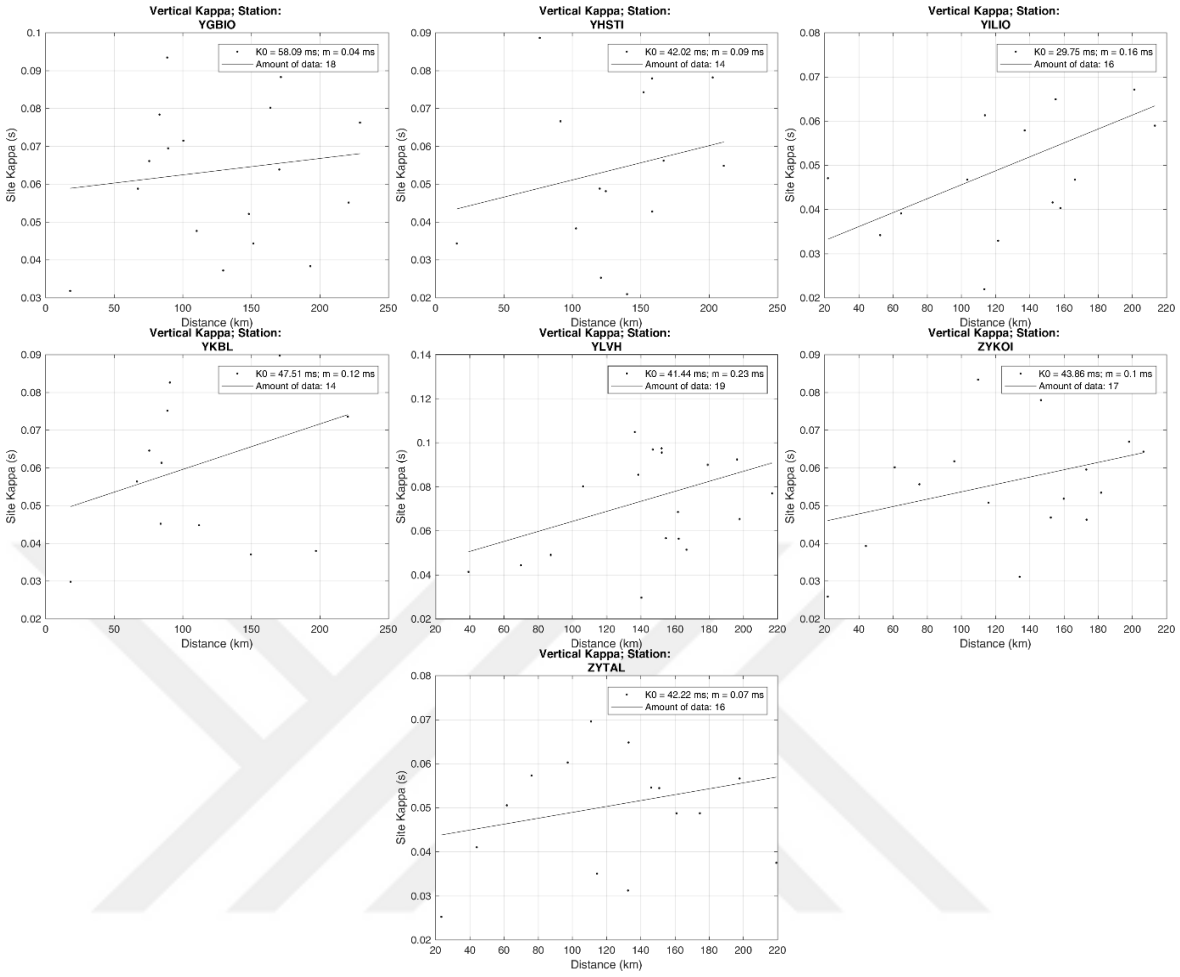

Figure 4.17. Vertical κ_r-distance regression in each station fulfilling the criteria (continued).

The results presented above are also plotted on maps and compared with estimated V_{S30} values, for both components. For the horizontal component's κ_0 distribution on map, 30 data for the European and 31 data for the Asian side were used out of 68 estimations (Figure 4.18a and Figure 4.20a). Nevertheless, for the vertical component, 33 data were used for the European side and 26 data for the Asian side, out of 66 κ_0 estimations. (Figure 4.18b and Figure 4.20b).

As mentioned before, and as can be seen from Figure 4.19, V_{S30} values are weaker in the European side of the city – they mostly vary between 180-460 m/s, while in some parts (especially in northern parts) they reach up to 1000 m/s. It is expected that soil with weak strength properties should diminish waves more; with the other words, more attenuation is expected in weaker soils, in contrast to the stiffer soils. It is clearly seen that, individually,

most of the values in this side of the city fulfill these expectations. At the southern parts we observed that some of the κ_0 values are higher than the other regions, where also the soil is weaker, for both horizontal and vertical components.

V_{S30} distribution in the Asian side is much complex according to the European side (Figure 4.21), which makes it hard to say that a certain level is dominating along this region. Rather, despite the complexity, high V_{S30} values are observed in this side which was barely seen in the European side. We see that V_{S30} values reach up to 1500 m/s, in this region. This also makes us expect lower κ_0 in some of the stations. In Figure 4.20, horizontal and vertical estimations match with a quite good agreement. We again see that some of the stations which are located over weak soils, and the κ_0 estimations are also observed as high (i.e. MODAI). Similar to the V_{S30} distribution in the Asian side, relatedly, κ_0 values are also disorderly distributed.

For a better agreement of V_{S30} and κ_0 values on the maps, the number of stations should be denser, due to the varying V_{S30} values in Istanbul. Nevertheless, the correlation of the V_{S30} and κ_0 is quite good, which is also an encouragement for more specific and detailed further studies.

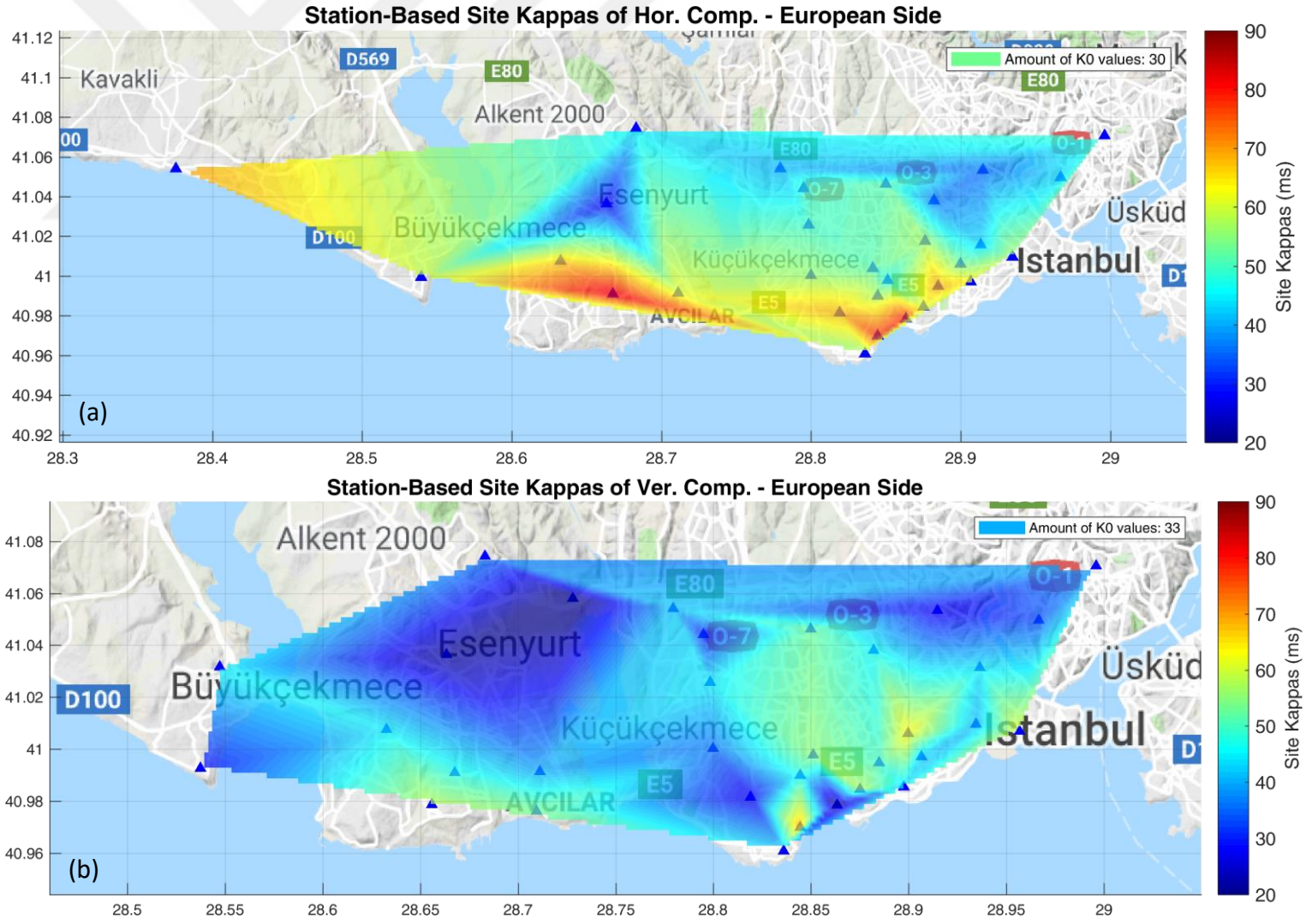

Figure 4.18. (a) Horizontal and (b) vertical κ_0 distribution for the European side of the city.

Figure 4.19. V_{S30} distribution for the European side of the city (adopted from Istanbul Metropolitan Municipality, 2007).

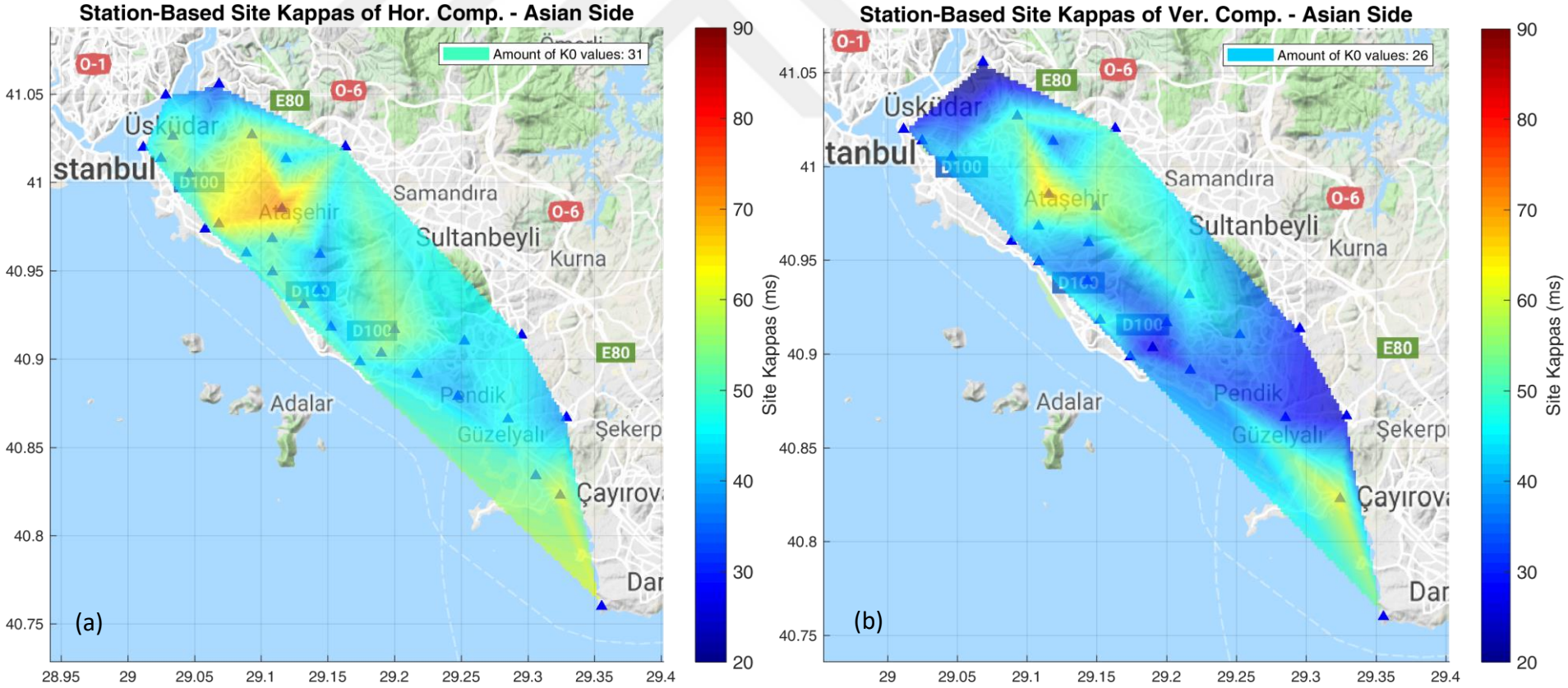

Figure 4.20. (a) Horizontal and (b) vertical κ_0 distribution for the Asian side of the city.

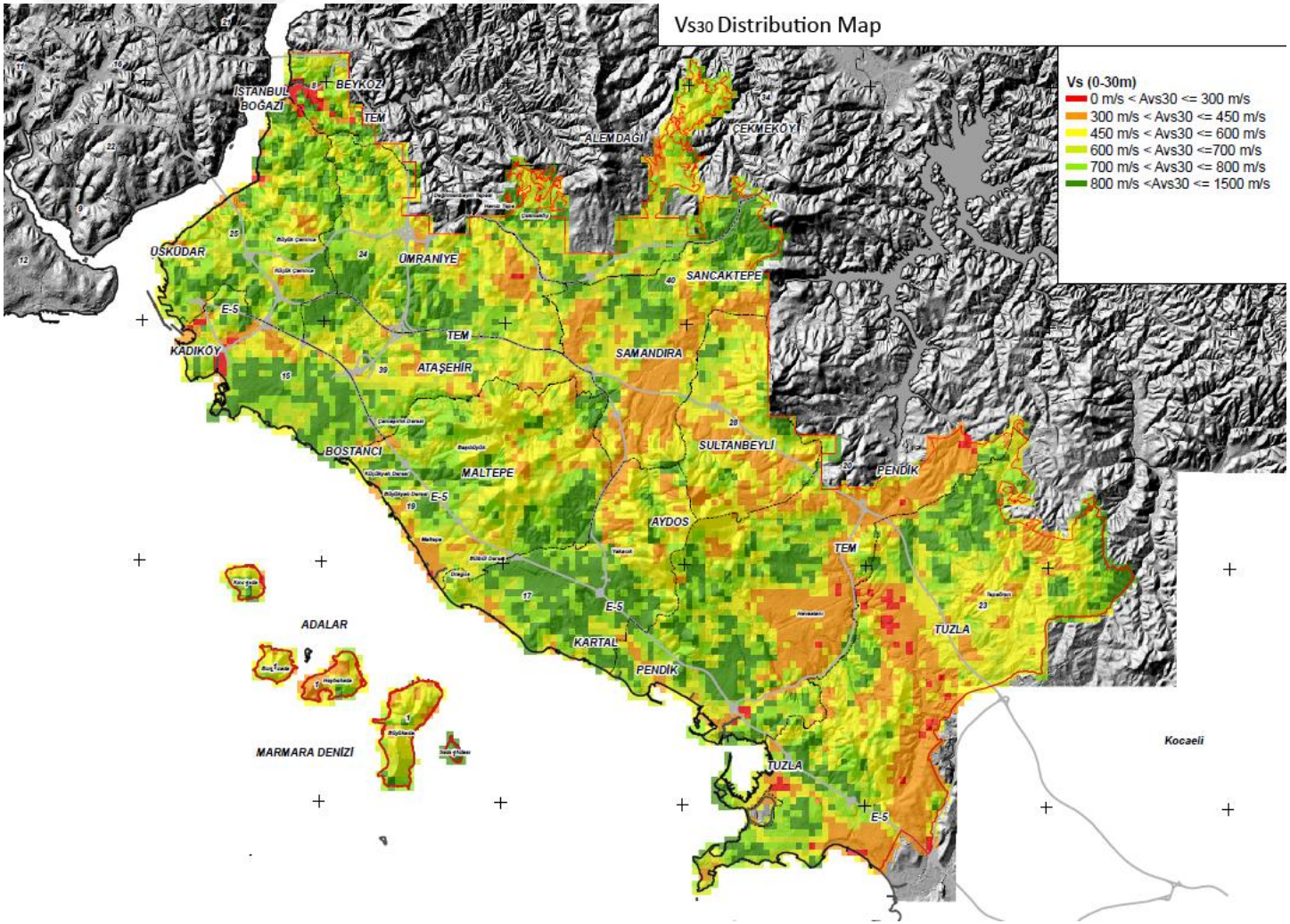

Figure 4.21. V_{S30} distribution for the Asian side of the city (adopted from Istanbul Metropolitan Municipality, 2009).

5. ANELASTIC ATTENUATION FACTOR (Q)

While seismic waves travel along the crust, they suffer attenuation as the result of two major factors, absorption and dispersion. As a vital property of seismic waves, attenuation has long been investigated by researchers. By the definition of Campbell (2009), seismic attenuation can be thought of as either the fractional loss of energy per cycle of oscillation or the exponential decrease in amplitude with time or distance.

Kjartansson (1979) showed that attenuation has linear frequency dependence. Because of such dependence, generally, the constant Q model is used. This model derives a single parameter expressing the absorption within the medium, which is the effective quality factor Q. Although there are several approaches for defining Q, they are all based on the original definition of Knopoff and MacDonald (1958),

$$Q = 2\pi \frac{E_0}{\Delta E} \tag{5.1}$$

where E_0 is the maximum strain energy in a cycle and ΔE is the energy dissipation in this cycle. As the linear geometrical attenuation is the basis of estimations nowadays, its frequency dependence is still being studied, but included as a crucial parameter.

Theoretical methods developed to estimate Q as a function require a constant Q value. Therefore, theoretical spectra can be derived and used for further investigations and simulations of wave propagation.

5.1. Methodology

Q has several uses once it is estimated from the seismic data. Most generally, it can give an idea about the regional stratigraphic properties, help on classifying data and simulating the region-specific attenuation. Both time-domain and frequency-domain approaches are developed so far to estimate Q. They are seismological and based on energy loss between two sequent wavelets and involve vertical seismic profiles (VSP) derived

through geophone records. But those who aim to determine Q for engineering purposes (as for ground motion simulations), mainly use different techniques, based on spectral amplitude decay.

Attenuation is observed through the spectral amplitude decay with respect to hypocentral distance (Castro et al. 1990),

$$D_i(f,R) = M_i(f)A(f,R) \tag{5.2}$$

where D_i (f,R) is the observed spectral amplitude of event i, while M_i(f) and A(f,R) represent the source term and the attenuation function, respectively. M_i(f) is a scalar related to the size of an earthquake.

To see a linearized shape of the equation above, it can be rewritten as in the following form.

$$logD_{ij}(f,R) = logM_i(f) + logA_j(f,R) \tag{5.3}$$

The total attenuation is defined with two parameters,

$$A(f,R) = G(R)e^{-\pi fR/vQ} \tag{5.4}$$

where G(R) represents the geometrical spreading and the exponential term represents the decay above corner frequency.

After plotting the $logD_{ij}$(f,R)-distance graph using the estimated values for chosen frequency, a straight line is fitted using the least-squares fitting method to estimate a constant Q for that specific frequency. By repeating the same step for several frequencies, a Q-frequency graph is used to observe the Q(f) function. The resultant function is written as defined by Nuttli (1973),

$$Q(f) = Q_0 f^a \tag{5.5}$$

5.2. Estimation Through Spectral Decay Method

To be able to estimate the frequency dependent anelastic attenuation parameter using the spectral decay method (Castro and Ruiz-Cruz, 2005; Safarshahi et al., 2013; Zengin and Çaktı, 2013), initially, regional path dependent parameters should be estimated. Geometrical spreading parameter is one of them. At close distances geometrical spreading is controlled by direct-wave amplitudes decaying along the crust, while at larger distances reflections and refractions from Moho and surface-wave spreading contributions exist. Geometrical spreading function is considered as equal to 1/R in uniform half space, while it can also be defined as a complex function (Atkinson and Boore, 2013; Atkinson, 2012).After observing the amplitudes at chosen central frequencies (1,1.5,3,5,7,10,13,18 Hz), to balance the irregularities of amplitudes at certain distance ranges, we concluded to use a triplet geometrical spreading model G(R):

$$G(R) = \begin{cases} R^{-1}, & R < 70\ km \\ R^{-0.7}, & 70\ km \leq R < 100\ km \\ R^{-0.5}, & 100\ km < R \end{cases} \tag{5.6}$$

where R is hypocentral distance. In order to minimize the amplification effects, only the vertical component of the recordings are selected. The following equation defines the observed spectral amplitude U(f,R) at hypocentral distance, R as:

$$U(f,R) = S \times G(R) \times \exp(-\pi f R \beta Q_S) \tag{5.7}$$

where S is the source-dependent scalar, G(R) is the hypocentral distance, β is the average shear wave velocity and Q_S is a constant value estimated by regression analyses (Figure 5.1) β is 3.42 km/s, for source depths beneath 31.6 km according to the model used by Regional Earthquake-Tsunami Monitoring Center, KOERI (RETMC, personal communication, 2018). The logarithm of equation 5.7 is taken, so that a single degree polynomial equation can be established as,

$$u(R) = a - bR \tag{5.8}$$

u(R), a and b can be expanded as,

$$u(R) = \log[U(f,R)/G(R)] \quad (5.9)$$

$$\mathrm{a} = \log \mathrm{S}\,; \quad \mathrm{b} = (\pi \mathrm{f}/\beta Q_S) \quad (5.10)$$

where u(R) is a distance dependent function, which represents the source amplitude corrected for geometric spreading function. The corrected amplitudes are regressed with respect to hypocentral distance at each central frequency separately. Q_S values are calculated at central frequencies of 1, 1.5, 3, 5, 7, 10, 13, and 18 Hz. Figure 5.1 shows the regression results along the selected central frequencies. After applying the geometrical spreading correction, the data spread along the distance axis was lumped. Due to the exceptionally high scatter above 200 km distances, the data was robust to the geometrical spreading model. So that they were removed from this analysis. The data up to 200 km shows good correlation with distance which is also supported by R^2 estimations. In our Q_S estimations, R^2 values range between 63%-68%, which is quite satisfying for such amount of data. At the same time, error range is another parameter showing us that the fitted lines plotted on the graphs are in trustworthy ranges.

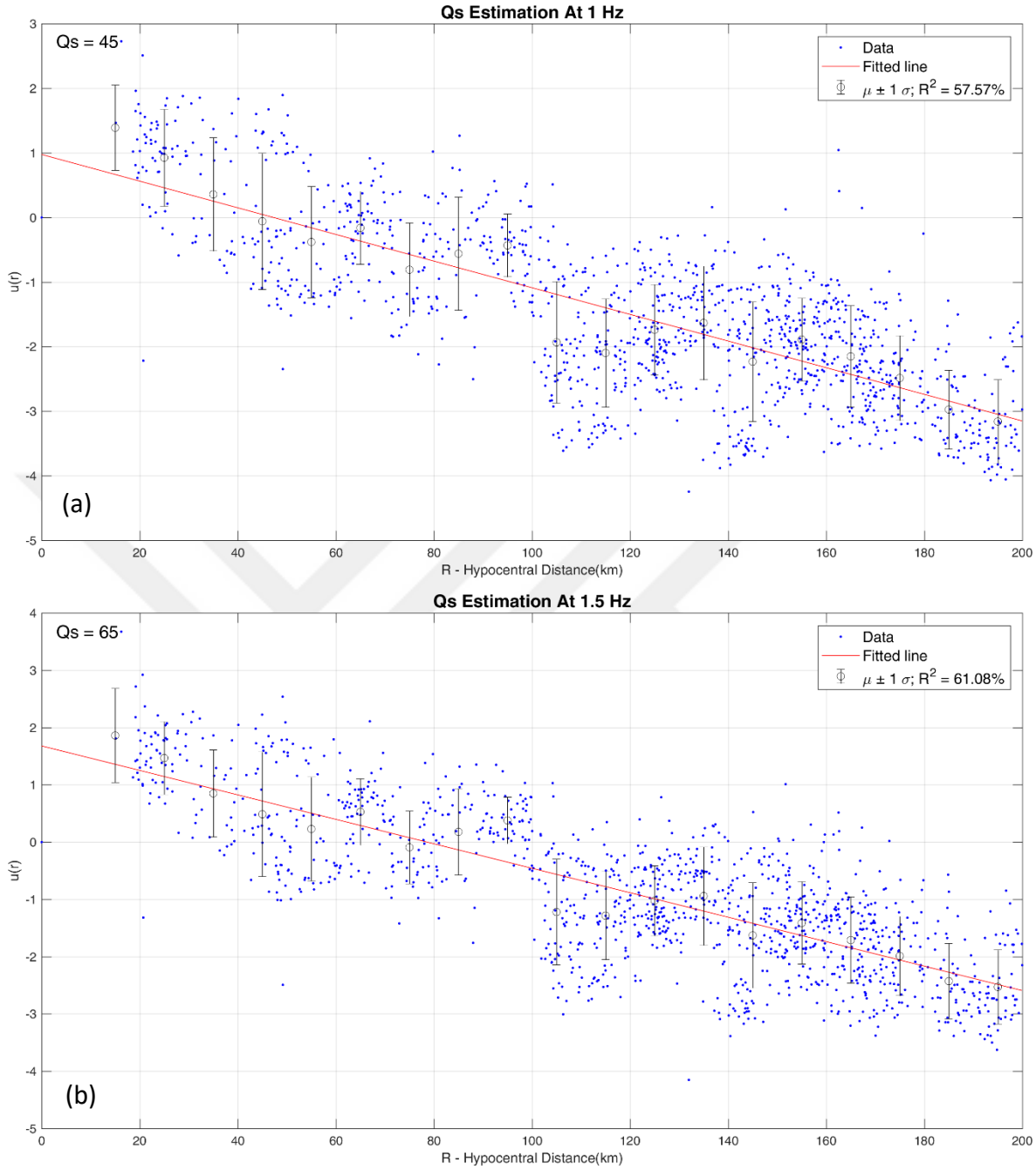

Figure 5.1. Qs estimations at (a) 1 Hz, (b) 1.5 Hz, (c) 3 Hz, (d) 5 Hz, (e) 7 Hz, (f) 10 Hz, (g) 13 Hz, (h) 18 Hz.

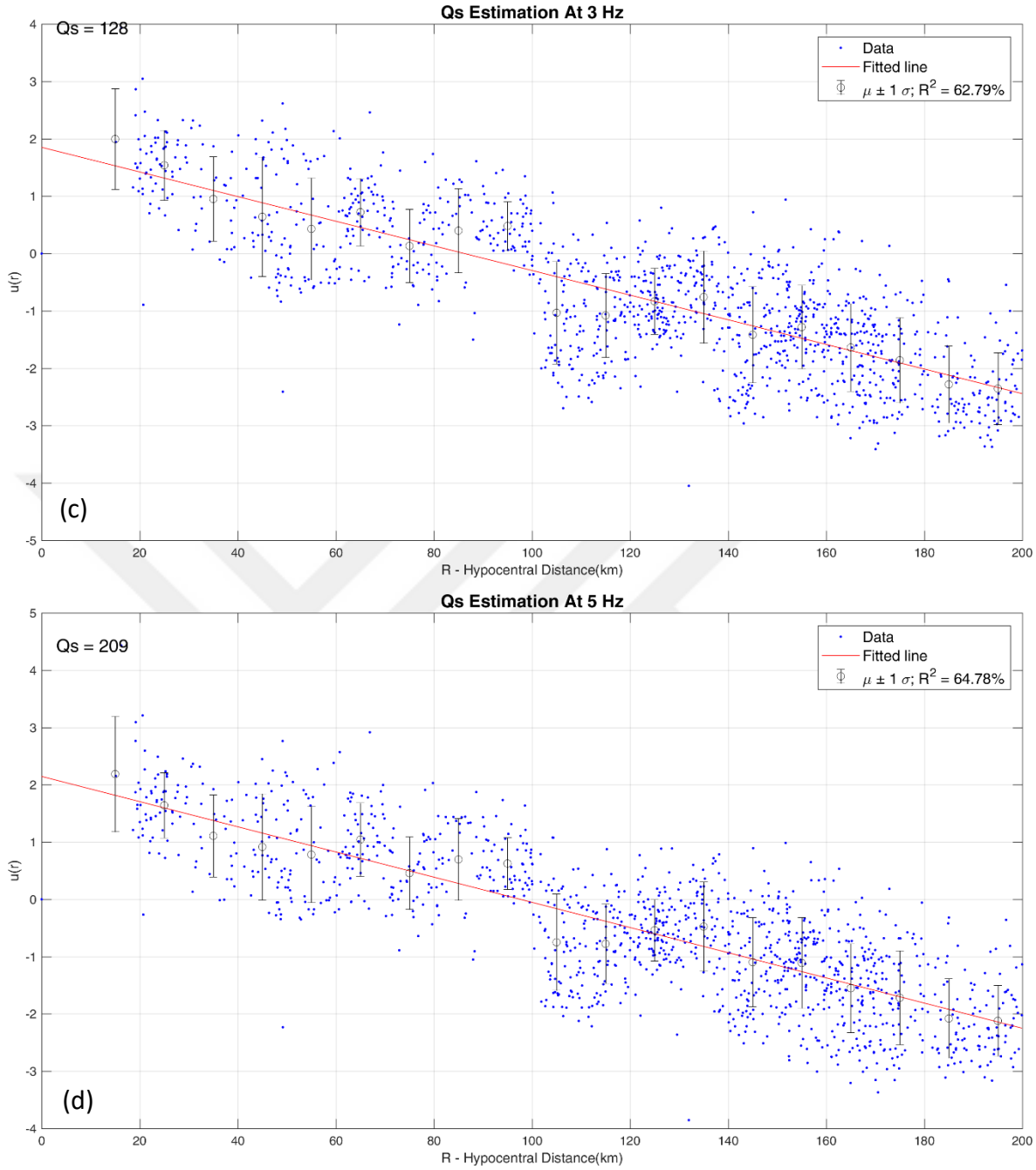

Figure 5.1. Q_S estimations at (a) 1 Hz, (b) 1.5 Hz, (c) 3 Hz, (d) 5 Hz, (e) 7 Hz, (f) 10 Hz, (g) 13 Hz, (h) 18 Hz (continued).

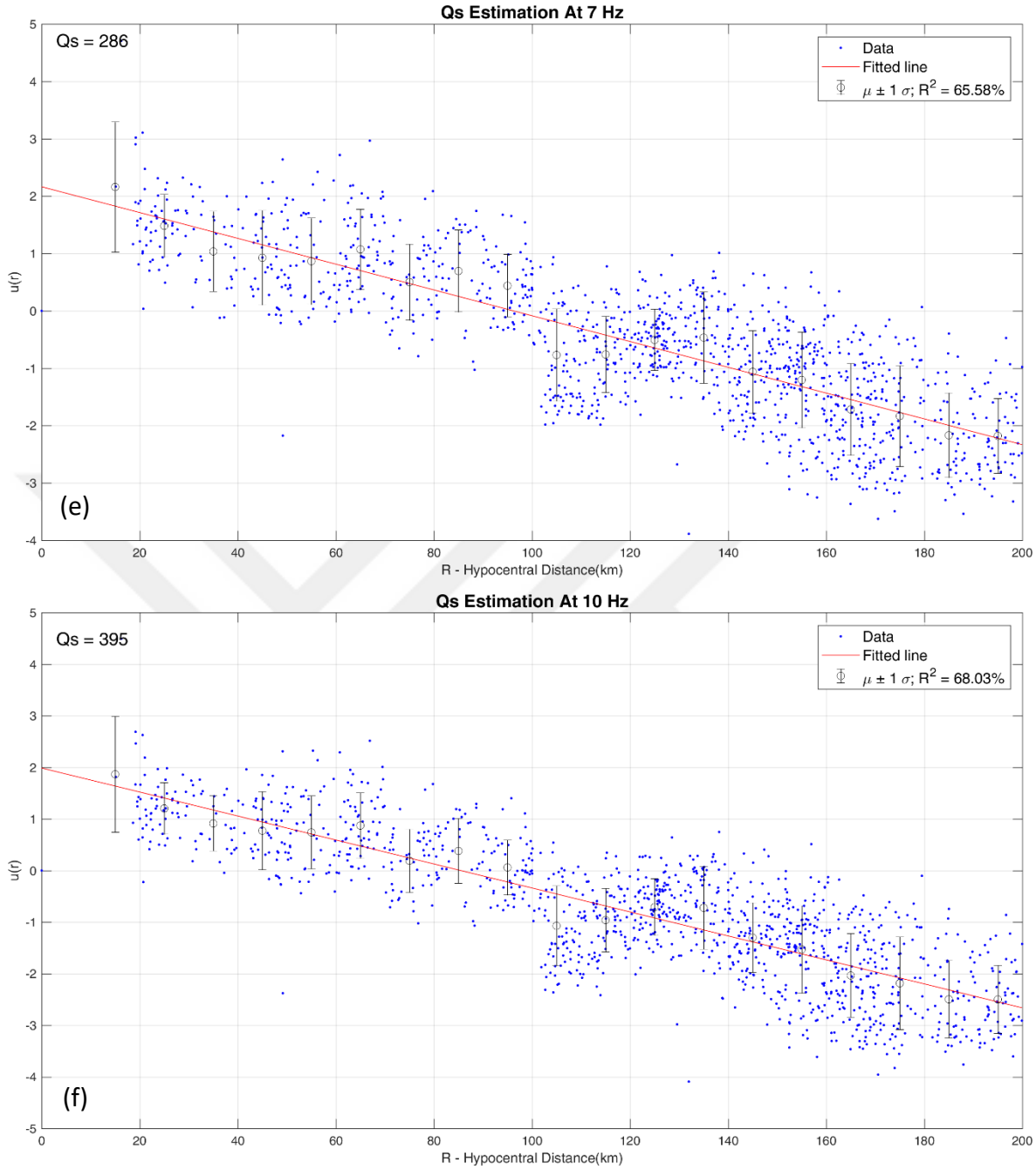

Figure 5.1. Q_S estimations at (a) 1 Hz, (b) 1.5 Hz, (c) 3 Hz, (d) 5 Hz, (e) 7 Hz, (f) 10 Hz, (g) 13 Hz, (h) 18 Hz (continued).

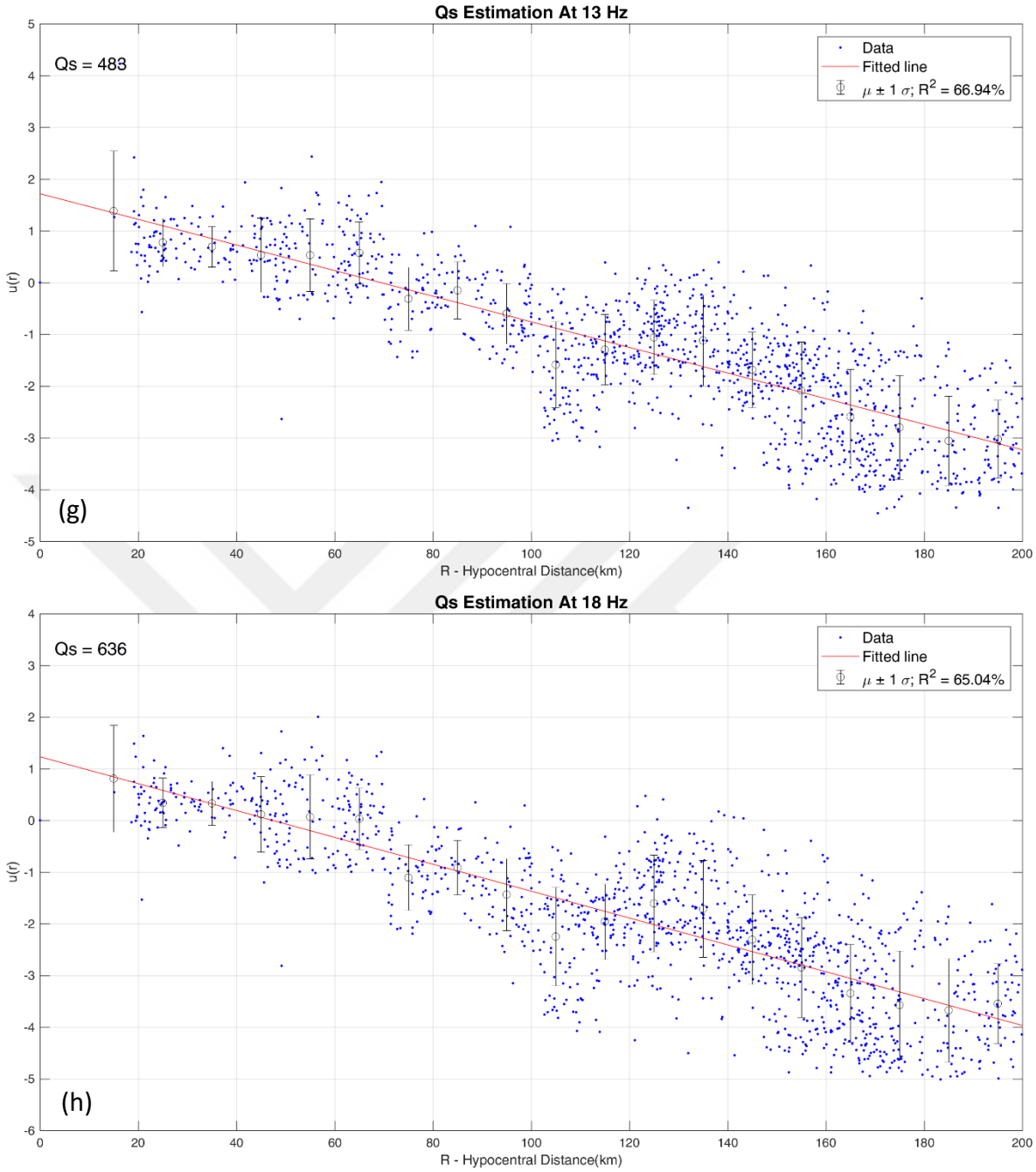

Figure 5.1. Q_S estimations at (a) 1 Hz, (b) 1.5 Hz, (c) 3 Hz, (d) 5 Hz, (e) 7 Hz, (f) 10 Hz, (g) 13 Hz, (h) 18 Hz (continued).

The Qs values are estimated as 45, 65, 128, 209, 286, 395, 483 and 636 for the central frequencies of 1Hz, 1.5 Hz, 3 Hz, 5 Hz, 7 Hz, 10 Hz, 13 Hz and 18 Hz respectively. The relationship between these values and corresponding central frequencies can be expressed as an exponential function (Figure 5.2). The frequency dependent Q function estimated through this analysis is given in equation 5.11.

$$Q(f) = 45f^{0.92} \tag{5.11}$$

Gündüz et al. (1998) by making use of small magnitude earthquakes recorded at distance ranges <100 km, proposed a frequency dependent anelastic attenuation function for the Marmara region as $Q(f) = (50 \pm 1.7)f^{1.09\pm0.05}$, which is so close to our estimation and supports its reliability. Akinci et. al. (2006), for the Marmara region estimated the Q parameter as $Q(f) = 180f^{0.45}$. One of the reasons of this difference should be the location of the stations. While Gündüz et al. (1998) use some stations located in Istanbul, none of the stations in Akinci et al. (2006) is in Istanbul.

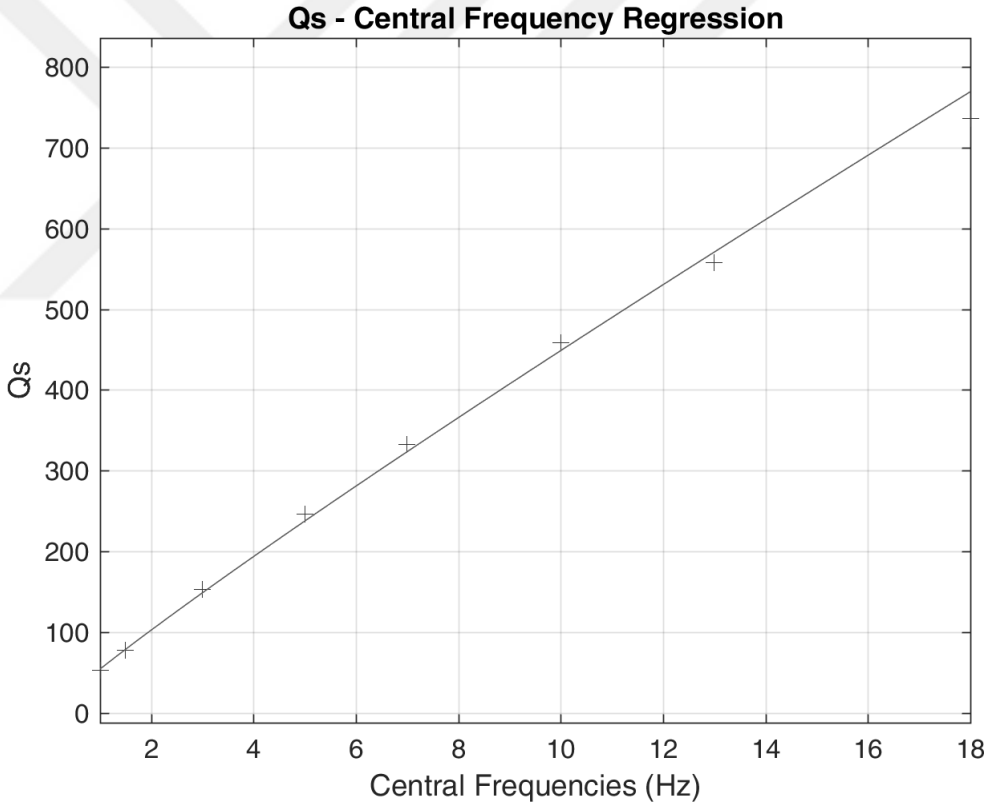

Figure 5.2. Qs – central frequency regression.

6. CONCLUSION

From our perspective, this study has significant outcomes on contributing to some discussions, opening new ones and pointing on some further studies.

The correlation of κ with distance regarding azimuths, showed the apparent path effect on κ_0 estimations in cases where data from larger distances are used. So that fitted line slopes may affect κ_0 results significantly. Unexpectedly, the differences among the results of these regression analyses reached up to 25% of difference. Similarly, while analyzing any possible relation between κ and SNR, we observed that the less contaminated data resulted with lower κ_0. Our preliminary results show that the difference in κ estimations when data with higher SNR is employed is at least 10% less, in contrast to the estimations with lower SNR. We also observed that estimating lower κ_0 also meant higher path dependence. Overall, our opinion is that the correlation with SNR still has to be worked on and discussed in detail. Complexity and variations in our κ estimations, makes it difficult to conclude on any specific model yet. Moreover, these analyses show that the site, path and source contributions on this parameter should be studied better and our results up to now should be refined even more.

The Q factor estimation is also supported with a previous study – the resultant equation prepared after the analysis is close to another equation prepared for the Marmara region previously. Our Q model was estimated with a sufficient amount of data, which we think supports its reliability. Additionally, in the future, its variations according to azimuths and with the path parameter of κ can be studied.

REFERENCES

Aki, K. (1967). Scaling law of seismic spectrum. *Journal of Geophysical Research*, *72*(4), 1217-1231.

Akinci, A., Malagnini, L., Herrmann, R. B., Gok, R., & Sørensen, M. B. (2006). Ground motion scaling in the Marmara region, Turkey. *Geophysical Journal International*, *166*(2), 635-651.

Akinci, A., Aochi, H., Herrero, A., Pischiutta, M., & Karanikas, D. (2017). Physics-Based Broadband Ground-Motion Simulations for Probable Mw≥ 7.0 Earthquakes in the Marmara Sea Region (Turkey) Physics-Based Broadband Ground-Motion Simulations for Probable Mw≥ 7.0 Earthquakes. *Bulletin of the Seismological Society of America*, 107(3), 1307-1323.

Anderson, J. G., and Hough, S. E. (1984). A model for the shape of the Fourier amplitude spectrum of acceleration at high frequencies. *Bulletin of the Seismological Society of America*, 74(5), 1969-1993.

Andrews, D. J. (1986). Objective determination of source parameters and similarity of earthquakes of different size. *Earthquake source mechanics*, *37*, 259-267.

Askan, A., Sisman, F. N., & Pekcan, O. (2014). A regional near-surface high frequency spectral attenuation (kappa) model for northwestern Turkey. *Soil Dynamics and Earthquake Engineering*, *65*, 113-125.

Atkinson, G. M. (2012). Evaluation of attenuation models for the northeastern United States/southeastern Canada. *Seismological Research Letters*, 83(1), 166-178.

Atkinson, G. M., and Boore, D. M. (2013). The attenuation of Fourier amplitudes for rock sites in eastern North America. *Bulletin of the Seismological Society of America*, 104(1), 513-528.

Boore, D. M. (2003). Simulation of ground motion using the stochastic method, *Pure Appl. Geophys.* 160, 635–676.

Boore, D. M. (2005). On pads and filters: Processing strong-motion data. *Bulletin of the Seismological Society of America*, 95(2), 745-750.

Campbell, K. W. (2009). Estimates of shear-wave Q and κ 0 for unconsolidated and semiconsolidated sediments in Eastern North America. *Bulletin of the Seismological Society of America*, *99*(4), 2365-2392.

Castro, R. R., Anderson, J. G., & Singh, S. K. (1990). Site response, attenuation and source spectra of S waves along the Guerrero, Mexico, subduction zone. *Bulletin of the Seismological Society of America*, *80*(6A), 1481-1503.

Castro, R. R., and Ruiz-Cruz, E. (2005). Stochastic modeling of the 30 September 1999 M w 7.5 earthquake, Oaxaca, Mexico. *Bulletin of the Seismological Society of America*, *95*(6), 2259-2271.

Durukal, E. (2002). Critical evaluation of strong motion in Kocaeli and Düzce (Turkey) earthquakes. *Soil Dynamics and Earthquake Engineering*, *22*(7), 589-609.

Durukal, E., and Catalyurekli, Y. (2004, August). Spectral analysis of source parameters of the 1999 Kocaeli and Düzce earthquake aftershock sequences. In *13th World Conference on Earthquake Engineering, Vancouver BC, Canada, Paper*(Vol. 421).

Erdik, M., Fahjan, Y., Ozel, O., Alcik, H., Mert, A., & Gul, M. (2003). Istanbul earthquake rapid response and the early warning system. *Bulletin of Earthquake Engineering*, 1(1), 157-163.

Gündüz, H., Ayşe, K. Ö., Aysun, B. G., & Niyazi, T. (1998). S-wave attenuation in the Marmara Region, northwestern Turkey. *Geophysical research letters*, 25(14), 2733-2736.

Hanks, T. C. (1982). f max. *Bulletin of the Seismological Society of America, 72*(6A), 1867-1879.

Hassani, B., and Atkinson, G. M. (2018). Adjustable Generic Ground-Motion Prediction Equation Based on Equivalent Point-Source Simulations: Accounting for Kappa Effects. *Bulletin of the Seismological Society of America*, 108(2), 913-928.

IBB-OYO-KOERI. (2009). İstanbul'un Olası Deprem Kayıpları Tahminlerinin Güncellenmesi İşi, Proje Çalışma Raporu, Boğaziçi Üniversitesi, Deprem Mühendisliği Bölümü, Istanbul

Istanbul Metropolitan Municipality (2007). Istanbul & Earthquake, European Side South Microzonation Project (online). Retrieved July 25, 2018, from http://www.ibb.gov.tr/tr-TR/SubSites/EarthquakeSiteEn/Pages/MicrozonationProjectEuropeanSideSouth.aspx

Istanbul Metropolitan Municipality (2009). Istanbul & Earthquake, Antolian Side Microzonation Project (online). Retrieved July 25, 2018, from http://www.ibb.gov.tr/tr-TR/SubSites/EarthquakeSiteEn/Pages/AntolianSideMicrozonationProject.aspx

Knopoff, L., and MacDonald, G. J. (1958). Attenuation of small amplitude stress waves in solids. Reviews of Modern Physics, 30(4), 1178.

Kjartansson, E. (1979). Constant Q-wave propagation and attenuation. *Journal of Geophysical Research: Solid Earth*, *84*(B9), 4737-4748.

Ktenidou, O.-J., C. Gelis, and F. Bonilla (2013). A study on the variability of kappa in a borehole, Implications on the computation method used, *Bull. Seismol. Soc. Am.* 103, 1048–1068.

Ktenidou, O. J., Cotton, F., Abrahamson, N. A., & Anderson, J. G. (2014). Taxonomy of κ: A review of definitions and estimation approaches targeted to applications. *Seismological Research Letters*, 85(1), 135-146.

Ktenidou, O. J., Abrahamson, N. A., Darragh, R. B., & Silva, W. J. (2016). A methodology for the estimation of kappa (κ) for large datasets. Example application to rock sites in the NGA-East database.

Lermo, J., and Chávez-García, F. J. (1993). Site effect evaluation using spectral ratios with only one station. *Bulletin of the seismological society of America*, *83*(5), 1574-1594.

Malcıoğlu, F. S. (2018). *Personal communication.*

Malcıoğlu, F. S., and Süleyman H. (2018). A practical approach for selection of the corner frequency of high-pass filters in processing earthquake records. *Proceedings of The European Seismological Commission 36th General Assembly.* University of Malta

Nakamura, Y. (1989). A method for dynamic characteristics estimation of subsurface using microtremor on the ground surface. *QR Railway Tech. Res. Inst.*, *30*(1), 25-33.

Nuttli, O. W. (1973). Seismic wave attenuation and magnitude relations for eastern North America. Journal of Geophysical Research, 78(5), 876-885.

OYO International Corporation (2007). Production of microzonation report and maps—European side (South): Final Report, Istanbul

OYO International Corporation (2009). Production of microzonation report and maps for Asia side: Executive Report, Istanbul

Parolai, S., Bindi, D., Durukal, E., Grosser, H., & Milkereit, C. (2007). Source parameters and seismic moment–magnitude scaling for Northwestern Turkey. *Bulletin of the Seismological Society of America*, 97(2), 655-660.

Picozzi, M., Strollo, A., Parolai, S., Durukal, E., Özel, O., Karabulut, S., Zschau, J., & Erdik, M. (2009). Site characterization by seismic noise in Istanbul, Turkey. *Soil Dynamics and Earthquake Engineering*, 29(3), 469-482.

Pinar A. (2018). *Personal communication*.

Regional Earthquake-Tsunami Monitoring Center, Kandilli Observatory and Research Institute, Boğaziçi University, Turkey (2018). *Personal communication.*

Safarshahi, M., Rezapour, M., & Hamzehloo, H. (2013). Stochastic Finite-Fault Modeling of Ground Motion for the 2010 Rigan Earthquake, Southeastern Iran. *Bulletin of the Seismological Society of America*, *103*(1), 223-235.

Tanırcan, G., and Dikmen, S. Ü. (2018). Variation of high frequency spectral attenuation (Kappa) in vertical arrays. *Soil Dynamics and Earthquake Engineering*, *113*, 406-414.

Tsai, C.-C. P., and K.-C. Chen (2000). A model for the high-cut process of strong motion accelerations in terms of distance, magnitude, and site condition: An example from the SMART 1 array, Lotung, Taiwan, *Bull. Seismol. Soc. Am.* 90, 1535–1542.

Van Houtte, C., S. Drouet, & F. Cotton (2011). Analysis of the origins of κ (kappa) to compute hard rock to rock adjustment factors for GMPEs, *Bull. Seismol. Soc. Am.* 101, 2926–2941.

Zengin, E., and Çaktı, E. (2014). Ground motion simulations for the 23 October 2011 Van, Eastern Turkey earthquake using stochastic finite fault approach. *Bulletin of earthquake engineering*, 12(2), 627-646.

Zülfikar C., Alçık, H. & Çaktı E. (2012), "Analysis of Earthquake Records of the Istanbul Earthquake Rapid Response System Stations Related to the Determination of Site Fundamental Frequency", *Proceedings of 15th World Conference on Earthquake Engineering, 24-28 September 2012, Lisbon, Portugal*, vol. 36, pp 28769-28776.

T.C
YÜKSEKÖĞRETİM KURULU
ULUSAL TEZ MERKEZİ

TEZ VERİ GİRİŞ FORMU

Referans No	10209083
Yazar Adı / Soyadı	HAKAN SULEJMAN
T.C.Kimlik No	99031264970
Telefon	5537746372
E-Posta	hakansuleyman1@gmail.com
Tezin Dili	İngilizce
Tezin Özgün Adı	ESTIMATION OF THE HIGH FREQUENCY DECAY PARAMETER (κ) AND ANELASTIC ATTENUATION FACTOR (Q) FOR ISTANBUL
Tezin Tercümesi	İSTANBUL İÇİN YÜKSEK FREKANS AZALIM PARAMETRESİ (κ) VE ANELASTİK AZALIM FAKTÖRÜ'NÜN (Q) HESAPLANMASI
Konu	Deprem Mühendisliği = Earthquake Engineering
Üniversite	Boğaziçi Üniversitesi
Enstitü / Hastane	Kandilli Rasathanesi ve Deprem Araştırma Enstitüsü
Anabilim Dalı	Deprem Mühendisliği Anabilim Dalı
Bilim Dalı	Deprem Mühendisliği Bilim Dalı
Tez Türü	Yüksek Lisans
Yılı	2018
Sayfa	90
Tez Danışmanları	PROF. DR. ESER ÇAKTI
Dizin Terimleri	
Önerilen Dizin Terimleri	

27.08.2018

İmza:.....